2-1-2016

DIRECT VOLTAGE MEASUREMENTS USING BULK ACOUSTIC WAVES IN LiNbO3

Nishant Patel

Nishant Bhupendra Patel
Candidate

Electrical and Computer Engineering
Department

This dissertation is approved, and it is acceptable in quality and form for publication:

Approved by the Dissertation Committee:

Edl Schamiloglu , Chairperson

Mark Gilmore

Zayd Leseman

Stefan Cular

DIRECT VOLTAGE MEASUREMENTS USING BULK ACOUSTIC WAVE SENSING IN $LiNbO_3$

by

NISHANT BHUPENDRA PATEL

BS, Optical Science and Engineering, University of California-Davis, 2004

M.S., Electrical and Computer Engineering, University of New Mexico 2010

DISSERTATION

Submitted in Partial Fulfillment of the

Requirements for the Degree of

Doctor of Philosophy

Engineering

The University of New Mexico

Albuquerque, New Mexico

December, 2015

DEDICATION

This dissertation is dedicated to my parents, for selflessly sacrificing their entire lives for me and my brother.

To my brother and his family, who have instilled in me the competitive drive and will power to never give up when faced with all the challenges life brings.

ACKNOWLEDGEMENTS

I want to extend my deepest appreciation to my committee chair, Professor Edl Schamiloglu, for taking me in as a student. His support, patience, and trust in me during this entire process gave me a chance to figure things out and believe in myself.

Secondly, I am extremely grateful to Dr. Stefan Cular for his mentorship and willingness to work with me to make my research successful. Despite my successes and failures, you were always fair and honest with me and I couldn't ask for anything more.

I want to thank both Professor Zayd Leseman and Professor Mark Gilmore for their time to be a part of my committee. Their insightful comments and valuable recommendations greatly assisted in completing this dissertation.

I greatly appreciate Dr. Darren Branch's time for showing me the ropes on many of the topics discussed in this dissertation as well as collaborating with me throughout my research efforts.

I want to thank the people who work in the Primary Standards Laboratory for their support and friendship. I want to thank my manager Roger Burton for allowing me to freely work on my Ph.D. research. Thanks to the AC Project for teaching me measurements and making work enjoyable. Particularly, I want to thank Dr. Eric Forrest, Jim Novak, Dr. Otis Solomon, and Tim Vanderburg for their contributions to this dissertation.

Lastly, the final year wouldn't have been completed without my love, Nichole Leahy, by my side. I am extremely privileged to have you in my life. Your patience, love, sacrifices, and encouragement changed everything for the better.

The Primary Standards Laboratory does not endorse or promote any of the equipment and manufacturers listed and used in this dissertation. Sandia National Laboratories is a multi-program laboratory managed and operated by Sandia Corporation, a wholly owned subsidiary of Lockheed Martin Corporation, for the U.S. Department of Energy's National Nuclear Security Administration under contract DE-AC04-94AL85000. The SAND number given to this document is SAND2015-7844 T.

DIRECT VOLTAGE MEASUREMENTS USING BULK ACOUSTIC WAVES IN $LiNbO_3$

By

Nishant Bhupendra Patel

B.S., OPTICAL SCIENCE AND ENGINEERING, UNIVERSITY OF CALIFORNIA-DAVIS, 2004

M.S., ELECTRICAL AND COMPUTER ENGINEERING, UNIVERSITY OF NEW MEXICO, 2010

Ph.D., ENGINEERING, UNIVERSITY OF NEW MEXICO, 2015

ABSTRACT

Accurate (< 1%) direct measurement of high voltage pulse amplitudes above 10 kilovolts becomes challenging due to voltage breakdown limitations in materials, parasitic impedance effects that can distort the pulse shape, and pickup of extraneous signals resulting from electromagnetic interference effects. A piezoelectric crystal-based bulk acoustic wave sensor using lithium niobate ($LiNbO_3$) that has applications to metrology, research, and power metering was developed to overcome these measurement issues with the factors of scalability, ease of use, and compactness in mind.

A Y+36° cut $LiNbO_3$crystal was coupled to two acoustic transducers, where direct current (DC) voltages ranging from 128–1100 V were applied transversely to the crystal. An acoustic wave was used to interrogate the crystal before, during, and after voltage application. Both single and multiple pass measurements were performed and compared to linear piezoelectric theory.

A comparison study between Y+36° and 0° X-cut $LiNbO_3$ was performed to evaluate the influence of crystal cut on acoustic propagation. The study was extended to applying alternating current (AC), and pulsed voltages. The measured DC data was compared to a 1-D impedance matrix model that was based on a three port circuit with voltage-induced strain effects inputted as a model parameter. An uncertainty budget was carried out for both crystal cuts and compared. Environmental effects such as pressure and temperature were also measured to determine their influence on the sensor under ambient conditions.

Published literature regarding material constants, such as elastic constants and piezoelectric constants, for $LiNbO_3$ do not account for the influence of an electric field. In light of this, measurements of the acoustic velocities and material constants under the presence of a DC electric field were performed up to 896 V. This information was used to develop an uncertainty analysis for the determination of stress-charge form piezoelectric constants e_{15} and e_{22}. All measured and calculated values were input into a Monte Carlo simulation to determine the error of the strain-charge form piezoelectric constants, d_{ij}, and how these new values can be used to predict the voltage sensor response.

Table of Contents

List of Figures

List of Tables

Acronyms

AC	Alternating Current
BAW	Bulk Acoustic Wave
BNC	Bayonet Neill–Concelman
CAT-IV	Measurement Category IV
$CuSO_4$	Copper Sulfate
DC	Direct Current
DUT	Device Under Test
IEC	International Electrotechnical Commission
LCR	Inductance-Capacitance-Resistance
$LiNbO_3$	Lithium Niobate
NIST	National Institutes of Standards and Technology
NMI	National Metrology Institute
PHVMS	Pulsed High Voltage Measurement System
PPB	Part Per Billion
PPM	Part Per Million
PSL	Primary Standards Laboratory
PZT	Lead Zirconate Titanate
RMS	Root Mean Square
RTD	Resistive Temperature Detector
SAW	Surface Acoustic Wave
SNL	Sandia National Laboratories
SNR	Signal-to-Noise Ratio
PR	Pulse Receiver
TIC	Time Interval Counter
ToF	Time-of-Flight

1 OVERVIEW OF HIGH VOLTAGE MEASUREMENTS

1.1 BACKGROUND

Measuring high voltage (HV), whether it is direct current (DC), alternating current (AC), or pulsed, can generally be performed using three methods: 1) measuring the spark gap between two conducting bodies (spheres, plates, etc.), 2) electrostatic voltmeters, and 3) voltage dividers. Although these HV measurement techniques exist, when the measurement requires accuracy of < 1%, the first two methods prove to be inadequate. The spark gap measurements provide, at best, an accuracy of ± 3%, excluding any environmental factors such as humidity or voltage breakdown between the conducting bodies [1]. When using electrostatic voltmeters for HV measurements, difficulty arises in calculating the electrostatic force when the electrodes are not a simple geometry. Another problem with electrostatic voltmeters is that the capacitance from the electrodes and the load inductance from the leads form a series resonant circuit that puts an upper limit on the measurable frequency [2].

A voltage divider circuit reduces the input voltage by a ratio defined by the circuit components. Typical arrangements for voltage dividers with associated equations for calculating V_{out} are shown in Figure 1.1.1. In this figure, L_1, R_1, and C_1 define the HV arm and L_2, R_2, C_2 define the low voltage (LV) arm. Additional instrumentation is connected to measure the output voltage, V_{out}. The LV arm

and HV arm values define the voltage division ratio, which is shown with the accompanying equation for each divider type in Figure 1.1.1.

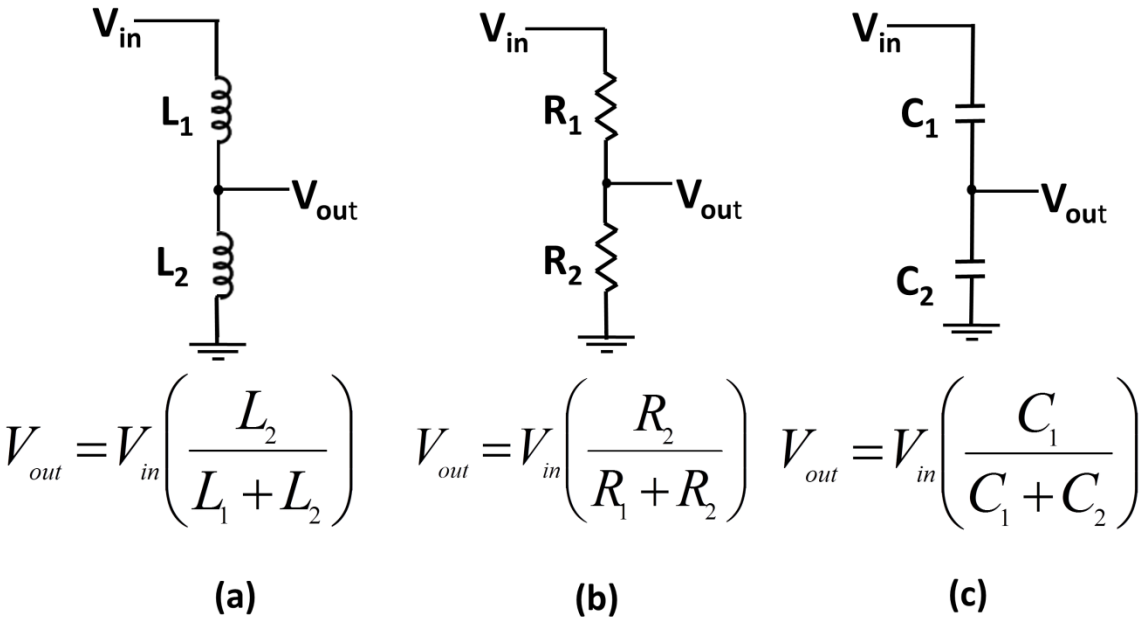

Figure 1.1.1. Schematic of three types of voltage dividers a) inductive, b) resistive, c) capacitive type.

Since V_{out} does not result in the direct measurement of V_{in}, device calibration is performed by comparing the device voltage output to that of a standard with a well characterized voltage division ratio. Calibration is the process that describes the conditions required to establish a relationship between values measured by an instrument or system [3]. The purpose of calibrating devices is to establish trust and reliability in a measurement such that subsequent measurements over the course of time are kept in control with respect to the environment and instrumentation used in the system. In terms of voltage dividers, calibration is important because the voltage divider ratio may drift over time, the HV or LV arm can be physically broken or have changed, or one or more connections could be

faulty. Thus, keeping a calibration record of such measurements is necessary. The standard is typically in the form of a resistor, capacitor, or a mix of these and other components. The accuracy of the standard traces to an International Standard of Units, known as the SI or metric system [3]. The type of standard used for HV measurements varies depending on these factors: 1) the type of voltage measured, 2) the accuracy desired, 3) the signal's frequency or pulse width, 4) the associated parasitic effects of each component, and 5) the ease of implementation into the overall measurement system [4].

Sections 1.2 through 1.5 provide descriptions of select electrical and optical technologies used to measure HV. Section 1.7 below contains state-of-the-art technologies with a high degree of accuracy, and Section 1.8 discusses the use of acoustic wave-based sensors for measuring voltage. The voltage divider sections include information and past measurements of HV dividers using inductors, resistors, and capacitors as the voltage dividing elements. Each section is further subdivided by the type of voltage measured. Following the divider sections, optical methods using nonlinear optical materials and optical fibers, as well as acoustic wave sensors using piezoelectric materials are discussed. Lastly, presently used HV measurements with corresponding accuracies are described.

1.2 INDUCTIVE VOLTAGE DIVIDERS

Inductive voltage dividers are based on current flowing through a conductor as described by Ampere's Law. Two inductors, L_1 and L_2 as shown in Figure

1.1.1(a), are chosen to achieve the desired voltage ratio for a defined frequency range. Since there are two inductors in the divider, two magnetic fields are generated and their respective magnetic fields can link and create coupling between the two inductors through their mutual inductance. Figure 1.1.1(a) shows a schematic of an inductive divider and the associated equation assuming no mutual inductance between the two inductors.

Inductive dividers were adopted from Blumlein's AC resistance measurements using inductive arms in a bridge circuit [5]. Using two inductive arms, Blumlein was able to determine a precise ratio between the two inductors, which was equal to the ratio of the number of turns in each inductor. The turns ratio was used to determine an unknown impedance. Using the turns ratio method from Blumlein's work, Gibbings and Hill were instrumental in realizing inductive dividers for low frequency resistance applications [6,7]. Hill's first inductive divider was successful in achieving uncertainties of 5 part per million (ppm) for voltage ratios of 500:1 and 1000:1 [7].

Later, two stage inductive dividers further improved the measurement uncertainty. The invention of the two stage transformer was an improvement over single stage current transformers, which suffered from errors due to changes in frequency, secondary current magnitude, and secondary circuit impedance [8]. The idea behind a two stage transformer is that adding an additional transformer corrects for the current's magnitude and phase. The two stage inductive divider used two inductive cores to improve measurement uncertainty.

Two stage inductive dividers are constructed by using two separate magnetic cores and two primary windings. One primary winding envelops a single magnetic core, while the other primary winding and secondary winding envelop both magnetic cores. The advantage of this configuration is a reduction in leakage current between the coils because very little current is drawn. The current magnitude drawn in a two stage configuration depends on the winding impedances and the mathematical theory that describes how the current was calculated can be found in the literature [9]. Using a two stage inductive divider with 10 decade adjustment, errors were reduced to 50 parts per billion (ppb) for the frequency range of 40 Hz-400 Hz [9]. Each decade corresponded to a different transformer ratio.

Hill and Deacon identified four independent errors that were common in these measurements: 1) different leakage inductances between the different decade section windings, 2) unequal conductor resistances, 3) internal loading in the windings themselves, 4) and core magnetic flux between decade sections were different but linked together [10]. Hill and Deacon found that these errors could be resolved by improving the inductor winding method, improving electrostatic screening and magnetic shielding, and by using either a smaller magnetic core or fewer winding turns.

To extend the work on inductive dividers to 100 kHz at 10 V, Homan and Zapf also utilized the two stage inductive divider technique. They improved the measurements by guarding each section of the divider using a coaxial cable inner conductor as the winding and the cable’s outer conductor as the guard.

This method mitigated the effects of unequal leakage inductance as well as interwinding capacitance, which scales with increasing frequency [11]. Although frequency scaling of the interwinding capacitance makes inductive divider operation at high frequencies difficult, dividers operating at frequencies up to 1 MHz with an accuracy of 30 ppm have been developed [12].

Driven by the CAT IV overvoltage protection category defined in the National Fire and Protection Association 70E standards, more recent work was performed to support higher voltages [13]. The CAT IV category includes circuits which directly connect to a power source that is used for buildings. As an example, measurements on a cable connecting the power transformer and a building qualify under CAT IV. The maximum switching voltage from channel to ground for this category is 1000 V. To improve such measurements for CAT IV circuits, researchers at the National Metrology Institute (NMI) of Australia constructed a two stage divider that operated up to 1000 V root mean square (rms) with a total operating bandwidth of 50 Hz-1 kHz [14]. The ratio error had an uncertainty of < 1 ppm across this frequency range. Because research on inductive dividers is driven by voltages and frequency range that satisfy the electrical power community, measurements of V > 1 kV have not been reported in the literature. Furthermore, inductive dividers are preferred in the power industry because their accuracy is much higher than capacitive and resistive dividers [15].

1.3 RESISTIVE VOLTAGE DIVIDERS

Resistive dividers are used for all voltage measurements, but are most commonly used for DC measurements. Figure 1.1.1(b) shows a schematic of a basic resistive divider, where R_1 is a large value resistor and R_2 a smaller value resistor. Like the inductive divider, the choice of values is determined by the desired voltage division ratio. Resistive dividers differ in accuracy depending on the type of voltage measured.

1.3.1 RESISTIVE VOLTAGE DIVIDERS FOR MEASURING DC VOLTAGES

For HV DC dividers, the standard resistor for the HV arm is of high impedance to prevent loading the voltage supply. The Park resistor was designed and constructed in the 1950's and is one of the earliest standard resistors [16]. The original Park resistor design consisted of several individual resistors that were connected in series and wound helically to reduce corona effects by allowing for a uniform potential drop along the length of the divider. Each individual resistor was specifically chosen and connected to mitigate resistance changes due to temperature variation. Park resistors are constructed so that the resistors can be stacked on top of each other to create a larger series resistor in the range of several MΩ. Furthermore, electrically biased metal shields are used to enclose resistor pairs and corona rings are placed on top of each Park resistor to eliminate corona discharges [17]. The Park resistor was measured to be accurate to within 10-20 ppm across a voltage range of 50 -100 kV [18].

Recent work performed by the NMI of Australia in this area involved measuring voltages > 800 kV. The resistor module consisted of 150 serially connected 1.5 MΩ metal oxide thin film resistors encased in aluminum shields. Much like the Park resistor, the resistor chain was wound helically around a polytetrafluoroethylene post insulator [19]. This resistor was used to measure 150 kV DC voltages with a voltage error of 5 ppm and 1000 kV with an error of 100 ppm. The largest source of error in the 1000 kV measurement was from leakage current, which reduces the measured voltage value and causes voltage division ratio variability [20].

1.3.2 RESISTIVE VOLTAGE DIVIDERS FOR AC AND PULSED VOLTAGES

For frequency dependent voltages, more consideration is needed for the divider design so that the waveform can be measured without being distorted. The two largest causes of waveform distortion are stray capacitance and inductance. Distributed stray capacitance, which exists due to spacing between two adjacent conductors, such as in a wire wound resistor, leads to a nonlinear potential across the HV arm, causing the divider ratio to be frequency dependent. The stray capacitance can also lead to increased rise times and response times, which can affect measurement resolution, as the divider might not be able to respond fast enough to the signal [21]. By using lower resistances on the HV arm or placing a parallel capacitive branch across the entire divider, the amount of stray capacitance can be reduced [22].

Figure 1.3.1. A two stack 200 kV DC divider developed at Australia's NMI. There are approximately 150 thin film resistors chained together helically for each divider stack Individual resistors are encased in metallic tubing and the entire chain wraps around an insulating tube. Each divider stack has a nominal resistance of 220 MΩ. This photo was taken in the DC Electrical Lab at the PSL.

Alternatively, aqueous solution resistors can be used to eliminate the wire wound resistors, effectively minimizing the stray capacitance. Figure 1.3.2 shows a schematic of an aqueous solution resistor. Here, a tube made of insulating material is filled with an aqueous solution with electrodes on top and bottom. The electrode material used depends on the type of solution used.

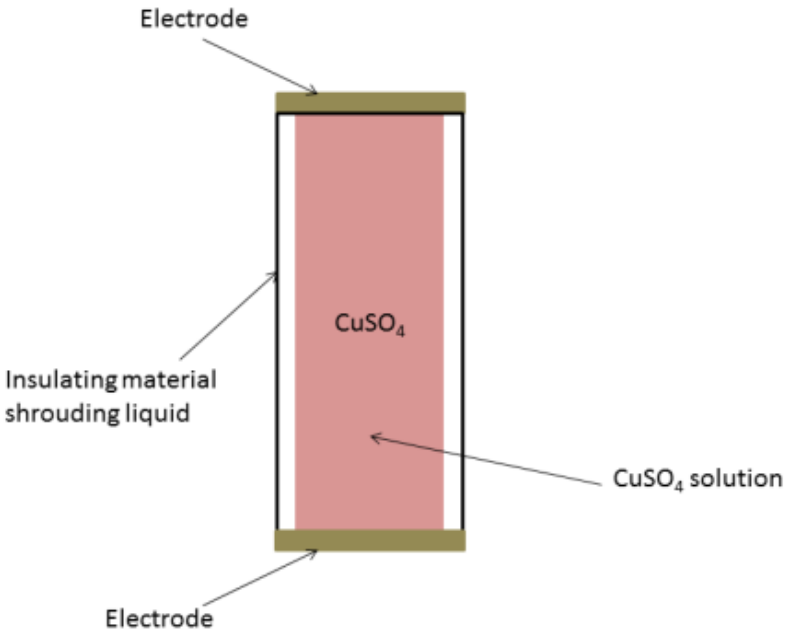

Figure 1.3.2: Schematic of a $CuSO_4$ resistor. The solution is encapsulated in an insulating tube and capped with copper electrodes.

The discussion here is limited to copper sulfate, $CuSO_4$, aqueous solution resistors which offer a higher solution resistivity than other aqueous solution resistors such as sodium chloride and silver nitrate without the toxicity [23]. Resistors whose values range from several MΩ to GΩ can be made using $CuSO_4$, making them suitable for HV division. $CuSO_4$ solution resistors have been used to divide MV level voltages with ns level rise times [24]. The accuracy of such resistors is typically not reported because the voltage division ratio is very sensitive to temperature variation. Recently, the divider ratio has been measured to vary as much as 0.04%/ °C due to temperature variation alone in a $CuSO_4$ resistor [24], although there are designs where the initial division ratio is determined by the ratio of a small length of the solution to the entire length, which would eliminate temperature variation. A detailed review of aqueous solution resistor applications and designs can be found in the literature [25]. For

frequency dependent dividers, compensating for just the stray capacitance and inductance is not sufficient and temperature sensitivity must also be accounted for to ensure good accuracy.

AC resistive dividers that operate from 10 Hz-100 kHz for voltages up to 240 V were studied using several high precision thin film resistors that were temperature compensated. Thirteen groups of two resistors were soldered onto a printed circuit board with a capacitor to improve impedance matching [26]. Each resistor was limited to a current input of 5 mA to reduce errors caused by resistive heating effects. Each resistive bundle was guarded by brass to reduce the capacitance between the resistors and the divider case. The brass guards only covered one of the resistors in each set. The guard was driven by a separate chain of resistors so that the guard would be equipotential to the resistors. Driving the guard reduced the effects of parasitic currents flowing onto and out of each resistor [27]. A voltage amplitude uncertainty 100 ppm was achieved using this method.

A similarly designed AC resistive divider using metallic thin film resistors was developed to operate from 50 Hz-10 kHz at voltages of 7.5 V-480 V. Here, two resistors were placed in parallel and then each parallel pair was connected in series. Instead of limiting the current in each resistor, this configuration allowed the researchers to limit the power consumed in each resistor, reducing resistive heating. This is done four times for a total buildup of 12 resistors [28]. Parasitic capacitance was reduced by placing equipotential shielding rings in between

each set of series and parallel resistors. An error of up to 25 ppm was measured for all the measurements in the aforementioned study.

A divider was constructed to measure both DC and AC voltages up to 10 kHz so that a single divider has the flexibility of measuring two types of voltage inputs [29]. The HV arm was constructed with 10 Ohmically large thin film resistors with low temperature coefficients that were placed between two circular electrodes that acted as protection from corona discharge. The LV arm consisted of a single 100 kΩ resistor. Voltages ranging from 200 V–1 kV were applied to individual resistors used in the HV arm and a 9.6 ppm error over that voltage range was measured when compared to a resistive standard that had an error of 3 ppm. Voltages from 4 kV–20 kV were then applied to the divider, where an error < 24 ppm was measured across this voltage range.

To use this divider for AC voltages, a capacitance between the individual resistor electrodes was measured and the time constant, $\tau = RC$, of the HV arm was matched to the LV arm. The time constant, τ, defines the amount of time taken for the capacitor to discharge to e^{-1} (or ~ 37%) of its original value. Furthermore, the inverse of τ can be used as a good estimate of the cutoff frequency, or the point in frequency where the power through the system is reduced.

The AC divider was tested using a 10 kHz waveform of unknown voltage to observe the effects of the divider ratio on frequency. An individual resistor from the HV arm was separately measured against a 0.01% resistive standard to show that an AC voltage of up to 1 kV at 10 kHz did not affect the resistor value. However, the study did not include AC voltage application beyond the component

level. A spline interpolation of the 10 kHz waveform results was used to estimate that the divider ratio error was < 0.15% up to 10 kHz [29].

A common theme in the previously mentioned resistive dividers is that they are comprised of several individual resistors. A detailed study on individual resistors and their reliability under HV conditions was performed in 2000 [30]. Three commonly used resistor types: metallic thin film, carbon film, and carbon composite resistors were compared. The resistors were subjected to pulsed voltages which produced voltage amplitudes of 15-35 kV with pulse durations of 2.5 μs. From the results, the resistance of the metallic thin film, carbon film, and carbon composite changed in resistance 5%, 150-250%, and 40-60%, respectively [30]. The carbon film resistors were found to handle the most pulsed power versus power rating, while the carbon composite resistors static resistance was most affected by pulsed voltage.

The limit of how high a voltage can be measured using resistive dividers is largely dictated by the voltage division ratio stability and instrumentation used to measure the voltage potential across the LV arm. As previously discussed, stray capacitance, stray inductance, leakage currents, etc. will affect the voltage stability ratio. For high frequency AC and pulsed voltages, commercial HV digitizers can typically handle up to 150 V at the expense of resolution. For low frequency (< 10 kHz) and moderate voltage levels (< 1200 V) a high precision digital multimeter with ppm level accuracy can be used to perform the measurements.

1.4 CAPACITIVE VOLTAGE DIVIDERS

To capture the transient features of a pulse voltage waveform properly, both high frequency (> 1 MHz) and HV (> 10 kV) need to be factored into the design of an accurate divider. Purely capacitive dividers can be used to satisfy both requirements. A generic capacitive divider setup is shown in Figure 1.1.1(c). The equation that describes a capacitive divider differs from a resistive or inductive divider because capacitors are summed by the inverse of the individual capacitances when capacitors are connected in series. Capacitive dividers can be categorized into two different types: 1) coaxial capacitive dividers and 2) series capacitive dividers. Stray inductance is the primary deterrent to using capacitive dividers, as it leads to nonlinearity in their high-frequency response. Since inductance is inversely proportional to length, it cannot be ignored when designing coaxial capacitive dividers. Literature findings have recommended that the upper frequency limit of the divider must be 1% of the natural frequency of the divider's equivalent circuit model. The natural frequency can be calculated from the stray inductance and capacitance [31].

Capacitive dividers were initially designed using a coaxial geometry [32]. Three terminal capacitive dividers with capacitors in a coaxial geometry were constructed with guard rings to eliminate fringing electric fields that occur at the conductor edges. This type of design measured up to 350 kV and had a temperature deviation of 0.01%/ °C with a cutoff frequency of 8 MHz [33,34]. More recent work has used coaxial capacitive dividers with an integrator to measure both the diode voltage and charging voltage of a pulse forming network

for an 80 ns repetitive electron beam accelerator at 530 kV and 560 kV, respectively to within 10% error [35]. The frequency response of coaxial capacitive dividers is ultimately limited by the resistance of the dielectric material used, since the material attenuates the signal as the frequency increases.

To avoid using dielectric material, capacitive dividers can be constructed with just two conductive parallel plates separated by a gap. Early work in high precision purely capacitive dividers at 60 Hz identified many of the problems and provided possible solutions [22]. The central issue that arises is that the divider must be connected to a pulse forming network whose leads have inductance. Since the circuit impedance is frequency dependent, higher frequencies cause the divider to be treated like a transmission line and not just a lumped element circuit. As a result, multiple reflections due to impedance mismatch will form a travelling wave in the circuit [33]. One way to circumvent this problem is by uniformly distributing a damping resistor along the HV arm much like in an AC resistive divider.

To eliminate the stray ground capacitances and distributed series resistance, a compressed gas capacitor can be used for the HV arm. This concept is based on Paschen's Law, which states that the electrical breakdown in an ideal gas can be determined by the gap distance between the electrodes and the pressure of the ideal gas [2]. For a gas capacitive divider, a homogeneous electric field is assumed. This configuration has improved linearity, little to no influence from the environment, small loading effects on the circuit, and can operate beyond 1 MV and has an upper frequency limit of close to 40 MHz [22].

Because capacitance depends on geometry in addition to material properties, very high bandwidth dividers can be created using wires and thin plates. Electric potentials in plasmas have been measured at frequencies 1 kHz-100 MHz by using a glass coated platinum wire tip as the dielectric and inner electrode, and the measured plasma as the outer electrode [36]. A very simplified plate capacitive divider embedded in a test chamber consisting of a thin aluminum foil separated from ground by a 125 μm thick sheet of Kapton was developed to measure rise times of 0.5 ns, which is important for use in measuring pulse outputs from ultrawideband radiation sources [37].

Designing the HV and LV arm of an impulse capacitive voltage divider requires great care in the design considerations. LV arm design is of greater concern because this arm is connected to the measurement instrument, so impedance matching to the instrument input (50 Ω or > 1 MΩ impedance) is of critical importance. The design of the LV arm was addressed by Jayaram *et al.* and Malewski *et al.* to improve the impedance matching problem [38,39].

Individual capacitors under HV conditions have been tested to the point of failure. Different values between 4.5 pF and 8200 pF were tested with ramped voltages between 600 V and 3 kV. The types of capacitors tested included film capacitors, ceramic capacitors, and molded Mylar tube capacitors. The set up was constructed such that a time dependent voltage was applied to the capacitor causing it to charge in a controlled manner. The current output was monitored and an abrupt change signaled capacitor failure. Research showed that all three types of capacitors withstood DC voltages of at least 10-16 times the rated

operating voltage for about 1 minute, and the energy stored in the capacitors for a short time was 50-250 times greater than the stated energy storage [40].

Resistive and capacitive dividers are commercially available from several vendors including Ross Engineering, Pearson Electronics, Ohm Labs, High Voltage Inc., and Haefely, among others. Although there are off the shelf versions, improved accuracy and higher voltage requirements generally leads to custom designs. High quality individual resistors and capacitors can be purchased from companies such as Vishay, Caddock, and Cooper Industries.

1.5 Alternative HV Measurement Methods

Resistive, inductive, and capacitive dividers have inherent bandwidth limitations, load the pulse forming network differently, can be large in size and cumbersome, and also suffer from electromagnetic interference. An alternative to the above methods is to perform the measurements either optically or acoustically. Optical and acoustic methods can potentially handle higher bandwidths, can have a small form factor, and can have minimal impedance loading on the pulse forming network than the traditional voltage divider.

1.6 Optical Methods for Measuring HV

To increase the bandwidth and eliminate electromagnetic interference from measuring HV signals, optical methods were researched before the laser was first realized. The earliest optical voltage measurements employed the Pockels effect, which is an electro-optic effect that involves inducing birefringence in a

material that is linearly proportional to the applied voltage [41]. Similar to the Pockels effect is the Kerr effect, in which induced birefringence in a substance is proportional to the square of the applied voltage. The strength of induced birefringence in a substance is described by its Kerr constant, a proportionality factor that relates the change in index of refraction to the square of the voltage. For both the Kerr and Pockels effect, induced birefringence can be related to a phase difference between an input and output light intensity generated from applying a voltage to the optical substance and the light propagating through that material. There are many detection schemes to measure the phase. This is discussed thoroughly in the literature [42,43].

Early work in this was area spawned from research on solar polarization filters and fast optical shutters for photography [44,45]. The earliest results utilized the Pockels effect to measure DC voltages up to 5 kV [46]. Early pulsed voltage measurements were performed using nitrobenzene, which has a relatively high Kerr constant for liquids, a high dielectric breakdown strength of 45-150 kV/cm (depending on purity), flat transmission spectrum for visible wavelengths (~400-700 nm), and a frequency independent dielectric constant up to 1 GHz [47,48]. Two drawbacks to using nitrobenzene are that it is inherently carcinogenic and explosive. Furthermore, since the Kerr effect is a function of the voltage (or electric field) squared, it is difficult to readily determine the electric field direction [49]. In the case of the Pockels effect, the electric field direction is defined, since the phase difference has a linear dependence with electric field. In the case of the Kerr effect, the square of the electric field is proportional to the phase, which

masks the quadratic dependence of the field to the phase. The direction of the electric field can be important when trying to establish the molecular polarizability of the Kerr gas. Pockels effect-based voltage sensors can be constructed using both integrated optical waveguide and bulk crystal configurations. Bulk materials, in the form of crystals, are chosen based off the strength of their nonlinear optical properties and transmission wavelength. Materials used as optical voltage sensing elements include quartz, $LiNbO_3$, and bismuth germanate [50-52]. Although bulk crystals can handle large voltages, they are free space optical systems which make alignment difficult to maintain as they are susceptible to mechanical vibration and shock. An integrated Pockels cell sensor has the advantage of being relatively compact and is less susceptible to mechanical vibration. However, because of the lower half wave voltage due to the small crystal thickness, voltage measurements above a few kV were not possible with the integrated voltage sensor. Presently, this technology utilizes two different lasers to interrogate a $LiNbO_3$ crystal, and uses the power output differences between the two lasers to map measured voltages of up to a few hundred kV [53].

Fiber optic based systems have also been studied by Bohnert *et al.* to overcome alignment difficulties with free space optical systems [54]. These systems are based on sensing intensity changes of light that is sent through a dual mode fiber wound around a piezoelectric crystal. Specifically, the voltage was applied across a quartz cylinder, inducing a strain in the material. This strain in the material was sensed by the wound fiber, which changed the light intensity as the light

propagated in the fiber. The induced strain in the quartz can be explained by the inverse piezoelectric effect, in which a mechanical displacement is generated by an applied electric field [55]. The test system was able to measure up to 420 kV ± 54 kV at 60 Hz, which is a common frequency used in electrical power. Voltages with frequencies up to 11 kHz were measureable before the piezoelectric resonance of the quartz crystal affected the response [56]. The stability was found to be less than 0.2% for a 14.4 kV rms voltage at 70 Hz. The minimum detectable voltage was found to be 2 V rms at 70 Hz. At 242.5 kV rms (the rms voltage of 420 kV), the minimum detectable limit was extrapolated to be 7.7 V rms at 60 Hz [57]. Such systems, which are commercially available, require that the sensing fiber affixed to the quartz and the receiver fiber in the detection system must have equal path differences to obtain a good signal [58]. This constraint makes fabrication complicated.

1.7 STATE-OF-THE-ART TECHNOLOGIES FOR MEASURING VOLTAGE

At present, a resistive divider is used to measure HV DC with the lowest measurement uncertainty. In particular, the dividers developed by Australia's NMI consist of 150 kV modules used as the HV arm in a resistive divider system. The DC electrical project group within the Primary Standards Laboratory (PSL) located at Sandia National Laboratories (SNL) presently uses these resistor modules as the primary standards to calibrate DC measurement devices at voltages up to 200 kV. The measurement uncertainty for such measurements is 100 ppm [20].

To measure HV pulses, different optical methods, resistive dividers, and capacitive dividers and are employed commercially and academically. The best traceable pulse HV measurements using capacitive and resistive dividers can be performed to an uncertainty of 1% [59]. This uncertainty increases to 4-6% due to positional, cable, instrumentation limitations, and terminator sensitivities.

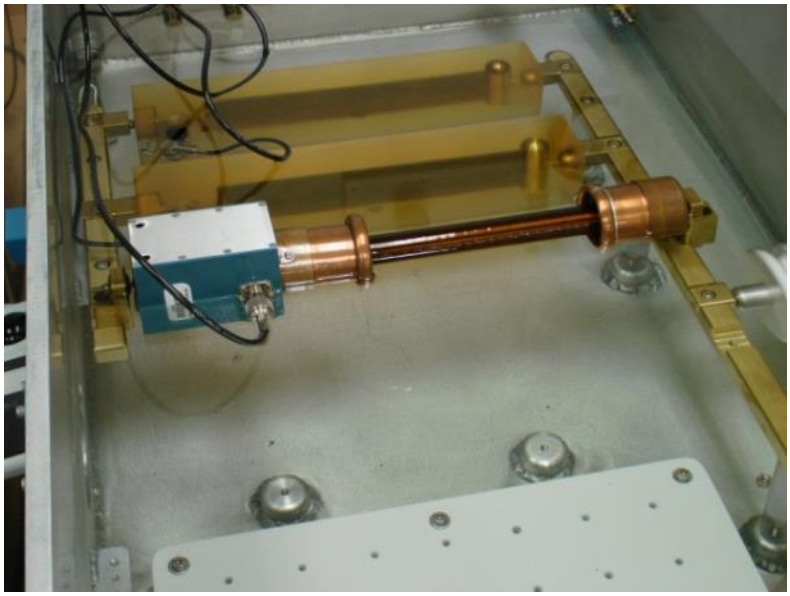

Figure 1.7.1. NIST-N1 resistor connected to brass supports within HV test tank. The N1 resistor is connected to two other resistors. This photo was taken in the AC Electrical laboratory at the PSL.

The measurement artifact used to calibrate devices to perform such measurements is the NIST-N1 voltage divider reference developed at the National Institute of Standards and Technology (NIST), which has an overall uncertainty of 0.5% [60]. This resistive device was characterized using a Kerr cell and DC resistance measurements. It provides a constant 5250:1 voltage division ratio from DC to 10 MHz with an operating range from 10 kV to 180 kV. The

divider is on permanent loan from NIST to the AC project Laboratory as NIST no longer performs such calibrations. There currently exists one version of this resistive divider in the world and no replacements are available. For pulsed voltage calibration the NIST-N1 artifact is the largest contributor to the measurement uncertainty. Table 1.7.1 shows the time-of-measurement uncertainty analysis for the pulsed HV divider used at the PSL.

Table 1.7.1: Uncertainty analysis for the calibration of a resistive divider at the PSL. The expanded uncertainty (k=2) is based on a 95% confidence interval.

Instrumentation	**Uncertainty**
Agilent L4534A-4 Channel Digitizer	0.004% (k=1)
NIST-N1 (5250:1, 10 kV–180 kV)	0.27% (k=1)
10 MHz Timebase	$1x10^{-11}$% (k=1)
Capacitor Standards	0.017% (k=1)
Connections	0.034% (k=1)
Repeatability	0.11% (k=1)
Combined Uncertainty	**0.29% (k=1)**
Expanded Uncertainty	**0.59% (k=2)**

The NIST-N1 artifact uncertainty accounts for 93% of the combined uncertainty. Because of this large contribution of error on the measurement, there exists a need for a new method of measuring HV non-DC measurements while improving the measurement uncertainty. Ideally, a primary standard would rely on physical properties that can be realized anywhere, and not rely on comparison to an artifact [61]. The work in this dissertation utilizes the benefits of acoustic waves with the piezoelectric effect in materials that are scalable to measure DC, AC, and pulsed voltages from 10 kV to 300 kV. Improved measurements would enhance the International Electrotechnical Commission (IEC) standard for high-

voltage reference measurement systems, which is used in areas such as: materials testing, power metering, pulse generator characterization, etc. This dissertation seeks to answer the question of whether or not a more accurate direct measurement HV sensor can be developed that relies on fundamental constants of a material and not an artifact.

Outside of using electrical or optical techniques to measure voltages, one can use acoustic wav-es. Acoustic wave sensing offers three advantages over lasers: 1) longitudinal acoustic waves are not polarization dependent, so alignment is not critical, 2) acoustic waves are not susceptible to low frequency vibrations, and 3) the cost of developing and maintaining an acoustic wave based system is generally lower [55,62,63].

1.8 ACOUSTIC SENSORS FOR HV APPLICATION

Acoustic sensors operate by utilizing a mechanical, or acoustic, wave as the sensing mechanism. In the context of this dissertation, the mechanical motion is created by vibrations of a crystal lattice. The two types of vibrations considered in this dissertation are compressional or longitudinal wave vibrations, and transverse or shear wave vibrations.

Acoustic wave sensors use piezoelectric material to generate the acoustic wave. Piezoelectricity, which was discovered in 1880 by the Curie brothers, describes the buildup of electrical charge in asymmetric solid materials, such as crystals and some ceramics, in response to an applied mechanical stress [64].

This relationship between mechanical stress and strain and electric field is represented by the linear piezoelectric constitutive equations

$$S_i = s_{ij}^E T_j + d_{mi} E_m \tag{1.8.1}$$

and

$$D_m = d_{mi} T_i + \varepsilon_{ik}^T E_k \tag{1.8.2}$$

where the subscripts *i, j* have values from 1 to 6 and *k, l, m* from 1 to 3. The variables are defined as follows: *S* is the strain, *s* is the stiffness, *T* is the stress, *d* is the piezoelectric constant, ε is the electrical permittivity, *E* is the electric field, and *D* is the displacement flux density. The superscripts denote the presence of constant stress or constant electric field [65]. Physically, equation 1.8.1 describes the total strain generated by the contributions of mechanical strain from Hooke's law and piezoelectric strain due to electric field biasing. Equation 1.8.2 defines the displacement field, which is determined by the piezoelectric polarization due to stress in the material and the relationship between the displacement field and electric field via the material's electric permittivity.

Longitudinal wave and shear wave vibration in $LiNbO_3$ are the two primary modes of acoustic propagation. Longitudinal waves are described by having displacement of the medium in the same direction as the direction the wave is traveling. Shear waves are described as displacement of the medium that is orthogonal to the direction of wave propagation. The propagation velocities associated with both vibrations is dependent on the material properties of

$LiNbO_3$. Preference of wave application depends upon the application. For this dissertation both shear wave and longitudinal wave propagation were studied.

1.9 CRYSTAL ORIENTATION TERMINOLOGY AND NOTATION

In crystallography, the crystal properties are described by their natural coordinate system, which is dictated by the crystal itself. The axes of this system are denoted by *a*, *b*, and *c*, and are the edges of the unit cell. The unit cell for $LiNbO_3$ is a primitive unit cell, where the crystal lattice points lie on the unit cell corners only. Due to crystal symmetry, there are 7 crystal systems–isotropic, cubic, orthorhombic, hexagonal, tetragonal, and trigonal, with each system divided into classes according to their symmetry. $LiNbO_3$ falls into the trigonal system and class 3m, which means there is exists three-fold symmetry about its *c* axis, or propagation axis [66,67]. The trigonal system lacks inversion symmetry, and this crystallographic property allows for the crystal to exhibit ferroelectricity, the Pockels effect, piezoelectric effect, photoelasticity, and nonlinear optical polarizability [68]. Industry practice states that the crystal cut, which designed as x-cut, y-cut, or z-cut, correspond to, respectively, the x,y, and z axis axes being normal to the large area surfaces. A second letter is added to the plate orientation description, indicating the direction of longest dimension of the plate or bar [69]. For example, an xy-cut crystal is an x-cut crystal with its longest dimension parallel to the y-axis.

The coefficients in the material constant matrices for $LiNbO_3$ are also dictated by the crystal symmetry. Lithium niobate has 6 unique elastic coefficients, 4 unique piezoelectric coefficients, and 2 unique dielectric coefficients. The subscripts in

equation 1.8.1 and 1.8.2, where the subscripts *i, j* have values from 1 to 6 and *k, l, m* from 1 to 3, all have a correspondence to the x,y, and z crystal axes.

Table 1.9.1: Table that relates corresponding crystal axis to indices used in equation 1.8.1 and 1.8.2 and throughout this dissertation.

Index	Corresponding Crystal Axis
1	x,x
2	y,y
3	z,z
4	y,z or z,y (shear)
5	z,x or x,z (shear)
6	x,y or y,x (shear)

Due to the anisotropy of $LiNbO_3$, it is important to track the elastic and piezoelectric constants with respect to the crystal orientation. Because several crystal cuts were used in this dissertation, a tracking method had to be established. This tracking method is accomplished using the 6 x 6 Bond transformation matrix [55]. Appendix A2 displays the mathematical steps taken to perform these calculations in more detail, and a thorough treatment can be found in the original Bond article.

1.10 SURFACE ACOUSTIC WAVE SENSORS USED FOR HV MEASUREMENTS

Surface acoustic wave (SAW) devices utilize the piezoelectric effect to generate acoustic waves on the surface of a material as a means of detecting physical phenomena. This configuration is commonly used for band pass filters, resonators, and environmental sensors in commercial and research laboratory settings [70-73]. A SAW device involves sending an electrical signal across the surface of a piezoelectric substrate using one or more interdigital transducers (IDTs). The IDTs are designed to generate an acoustic wave at the frequency

defined by the spacing between each transducer finger. Strain produced in the material causes a length change in either direction depending on the crystal and its orientation. The material changes can be detected as either a time or frequency shift of the propagating acoustic wave. The substrate surface between the input and output IDT, as shown in Figure 1.10.1 is often perturbed by voltage, biological or chemical agents, mass, or other physical phenomena. These perturbations generate length changes of the substrate material, leading to changes in the acoustic wave velocity.

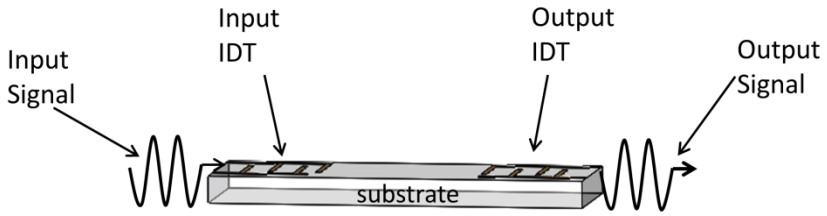

Figure 1.10.1: Generic SAW delay line sensor layout. The sensor output signal is determined by the substrate, IDT configuration, and the perturbation to the delay line.

SAW sensor configurations using various piezoelectric crystals and cuts were implemented to detect voltages in the range of 1 V-7 kV [74-77]. Materials used in the past include $LiNbO_3$, bismuth germanate, quartz, and lead zirconate titanate (PZT) [76,78,79]. The limitation of this work was the substrates used were less than a millimeter thick; the breakdown voltage of the crystal was easily exceeded when measuring voltages larger than 10 kV. As an example, measuring 200 kV with $LiNbO_3$ would require a material thickness of 10 mm, as opposed to the 0.5 mm substrate thickness used in Joshi's work [74].

Double SAW sensors can also be used in a HV sensor system. The advantage of using a double SAW sensor is utilize one oscillator as a reference sensor and the other oscillator as the voltage sensing unit [80]. Using this configuration, both oscillator frequencies are tracked with respect to temperature such that the frequency difference between each oscillator is temperature independent [81].

1.11 BULK ACOUSTIC WAVE SENSORS

Bulk acoustic wave (BAW) sensors differ with respect to SAW sensors in that the acoustic wave propagates within the crystal body and not on the surface of the substrate as observed in the SAW configuration [82].

BAW sensors are excited to generate shear waves as well as longitudinal waves. The electroded region also plays a role in restricting the vibrating area [83]. These types of sensors are commonly used as shear thickness mode devices, which is what is shown in Figure 1.11.1. Such devices are used to detecting mass deposited onto a crystal surface as well as liquids [65,84].

The BAW configuration is more commonly used in wireless applications for RF filter and resonator applications since they are easier to integrate with silicon chip fabrication [85]. Furthermore, they have better power handling capabilities, less sensitive to surface contamination than SAW devices, and better electric field containment between electrodes than SAW devices [86].

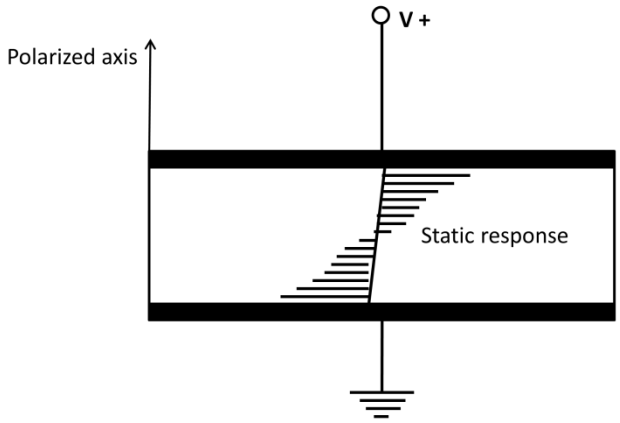

Figure 1.11.1: Schematic of a thickness shear mode bulk acoustic wave device. As DC voltage is applied in the thickness direction, a static shear wave is created in the bulk crystal. Electrodes can also be placed on the top of the material.

1.12 MATERIAL CHOICE FOR BULK HV SENSOR

Table 1.12.1 describes characteristics of some commonly used piezoelectric materials in acoustic-based sensors. Lithium niobate was chosen as the material for the HV sensor presented in this dissertation. $LiNbO_3$ has relatively large piezoelectric constants and can be grown to large thicknesses so that voltages well above 10 kV can be tested and corrected for temperature. This material also has a large bandwidth, as evidenced by its use in optical modulators [87]. In the frequency regime used in this dissertation, the relationship between dielectric permittivity and frequency is constant [88].

Table 1.12.1: Select piezoelectric materials commonly used in acoustic wave sensors.

Bulk Material	**Relative Electrical Permittivity (unitless)**	**Piezoelectric Constants (10^{-12} C/N)**	**Electrical Breakdown Voltage (V/mm)**	**Notes**
Quartz	4.52-4.68	-0.67 to 4.6	100,000	Hard to grow large samples without damage, weak piezo constant
Zinc Oxide	9.16-12.64	-11.34 t0 11.67	25,000-40,000	Cannot grow thick samples without damage

PZT	1,700-1,730	-171 to 584	8,000-16,000	Cannot grow thick samples without damage, hysteresis effects
Lithium Niobate	30 to 84	-1 to 68	20,000	temperature sensitive
Bismuth Germanate	16	0.87	2,000	Weak piezo constant

The electrical voltage breakdown for $LiNbO_3$ is ~20 kV/mm, which makes it suitable for measuring voltages in the 100's of kilovolts with commercially available crystal thicknesses [89].

The remainder of this dissertation is organized as follows. Chapter 2 discusses the theory of operation of for bulk acoustic wave voltage sensors using the piezoelectric crystal $LiNbO_3$ [90]. Chapter 3 presents a comparison study between two crystal cuts of $LiNbO_3$ to determine how crystal cut influences the sensor response [91]. Chapter 4 details how ambient environmental conditions of pressure and temperature influence the sensor response. Chapter 5 discusses voltage dependent velocity and material constant measurements and how the results can be used to predict the sensor response. Conclusions and recommendation for future work are summarized in Chapter 6.

2 OPERATIONAL CHARACTERISTICS AND THEORY OF BULK ACOUSTIC WAVE SENSOR

2.1 INTRODUCTION

The information presented in this chapter discusses the use of $LiNbO_3$ as a time-of-flight sensing element to measure the acoustic wave delay as a function of applied voltage. The experimental setup, configuration of the sensor, and preliminary data is discussed for a bulk Y+36°-cut $LiNbO_3$ crystal and its response to DC voltages up to 1100 V.

2.2 ACOUSTIC TRANSDUCERS

Both transmitting and receiving acoustic transducers (Olympus NDT) are used in this experiment. Acoustic transducers contain either a piezo-ceramic or piezoelectric material, which expands or contracts when an electric field is applied. Depending on the sample's orientation, the expansion or contraction generates a compressional or shear wave. For the measurements described in chapters 2 and 3, a longitudinal wave transducer was used. The measurements described in chapter 5 include the utilization of a shear wave transducer. The energy of the pulse applied to the transducer was between 1 μJ–4 μJ at a rate of 150 Hz. The repetition rate was controlled by the signal generator that externally triggered the pulse/receiver (PR) unit. The acoustic wave damping setting varied between 50 Ω and 150 Ω, and both 3 mm element size transducers are of the same make and model and operate at 10 MHz with a 5 MHz bandwidth at -6 dB. Glycerin is used to provide better impedance matching between the transducer face and the crystal as opposed to just the transducer face and the crystal separated by air.

2.3 TIME INTERVAL COUNTER

The time interval counter (TIC) is utilized throughout this dissertation as the main apparatus used to measure acoustic propagation time as a function of voltage in $LiNbO_3$. A stable quartz oscillator defines the spacing of the clock frequency for the TIC, which varies from 0.1 Hz to 100 MHz. In our experiment, this quartz oscillator is phase locked to an external house oscillator. The external 10 MHz

timebase has a time stability of 1 ppb. The main gate, which is generated by an externally synced signal generator, dictates the beginning and end of the time interval. Start and stop inputs are used as amplitude level indictors for the counter so that it can begin counting pulses. The trigger levels for the TIC used in this experiment were set with respect to the amplitude levels of the electrical bang of the transducer and the mechanical wave response that corresponded to the appropriate acoustic propagation mode. The “start” signal of the gate is synchronized to the output of the acoustic wave transducer, and the “stop” signal is generated after the acoustic wave has passed through the crystal once. The signal generator gated the amount of time between the start and stop signal. The resolution of the start and stop triggers was 10 mV ± 0.5% of the setting. No prior knowledge of the acoustic velocity of the mode and subsequent acoustic propagation time through the crystal leads to the TIC detecting noise or unwanted signals subsequently producing inaccurate measurements. Typical propagation times measured by the TIC in this dissertation were between 2 and 3 μs.

2.4 SENSOR CONFIGURATION

Commercially available $LiNbO_3$ is utilized to produce a bulk acoustic wave (BAW) sensor for measuring HV for AC, DC, and pulsed voltage applications. The data presented in this chapter takes advantage of this piezoelectric property by allowing the crystal to be utilized as a time-of-flight sensing element to measure the acoustic wave delay as a function of applied voltage. A 36° Y-X cut $LiNbO_3$

(Boston Piezo-Optics) was selected to measure DC voltages up to 1,100 V directly, without a voltage divider or electrostatic meter. To avoid complexity, the crystal cut was chosen such that a single acoustic mode propagates in the crystal, while other modes are too small to really interfere.

The $LiNbO_3$ crystal used in this work had dimensions of 15.0 mm $\times$ 5.0 mm $\times$ 5.0 mm with gold electrodes that had a cross sectional area of 25 mm^2 and thickness of 0.35 μm. The electrodes were positioned in the middle of the crystal on two opposing sides in the Y-Z plane. The electrodes were placed 5 mm from the stainless steel casing of either transducer for electrical isolation. Figure 2.4.1 shows a schematic of the Y+36° cut crystal used in the shear wave voltage sensor measurements.

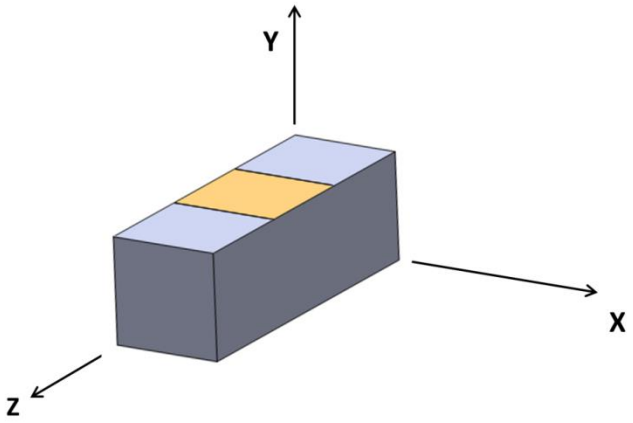

Figure 2.4.1: Y+36° cut crystal schematic used for shear wave measurements. The region on the top and bottom of the figure (not shown), indicated by gold color designates the electrodes. The dimensions of the crystal are 15.0 mm $\times$ 5.0 mm $\times$ 5.0 mm with gold electrodes of a nominal 5 mm $\times$ 5 mm $\times$ 0.35 μm in the middle of the crystal on two opposing sides in the Y-Z plane.

The crystal was enclosed in a non-conductive Delrin fixture with nominal dimensions 30 mm $\times$ 24 mm $\times$ 20 mm. The fixture held the crystal and two

threaded voltage connector sleeves were used to apply the voltage. Figure 2.4.2 shows the fixture used and a schematic of the experimental setup. Two acoustic transducers mounted directly onto the fixture were used for transmitting and receiving an acoustic wave through the crystal. The transmitting transducer was screwed into one side of the fixture and the receiving transducer was clamped to the other side using a spring and backing plate. The excited transducer acoustic wave propagates through the crystal and is monitored before, during, and after the HV was applied by a receiving transducer. A 1 V, 1 kHz pulse from a signal generator (Agilent 33250A) was used to externally trigger a pulser/receiver unit (Olympus NDT 5073PR) that controlled the transducers. The pulser/receiver system output was monitored by a TIC (Stanford Research Systems 620) that utilized an external 10 MHz signal as its time reference. The signal generator was also used to act as the timing gate for the measured signal. Figure 2.4.3 shows a representative oscilloscope trace of an acoustic response observed in these experiments where the timing gate is defined by the blue square pulse. Although Glycerin couplant was used for reducing the acoustic impedance mismatch between the transducer elements and crystal face, small reflections were still present outside the timing gate. These additional signals are reflections between the transducer face/glycerin interface, and glycerin/$LiNbO_3$ interfaces.

The PR unit was used to transmit and receive the acoustic wave and the TIC was used to collect the receiving transducer signal. For these initial measurements the nominal propagation time for the acoustic wave for this crystal orientation was 2.79 μs.

For the voltage measurements, a multicalibrator system (Fluke 5700EP) was used as the voltage source. A computer automated procedure was developed for data collection. A baseline measurement was performed for 30 seconds in the absence of an applied voltage before and after the 30 second voltage measurements. This process was repeated for 12 cycles at each voltage.

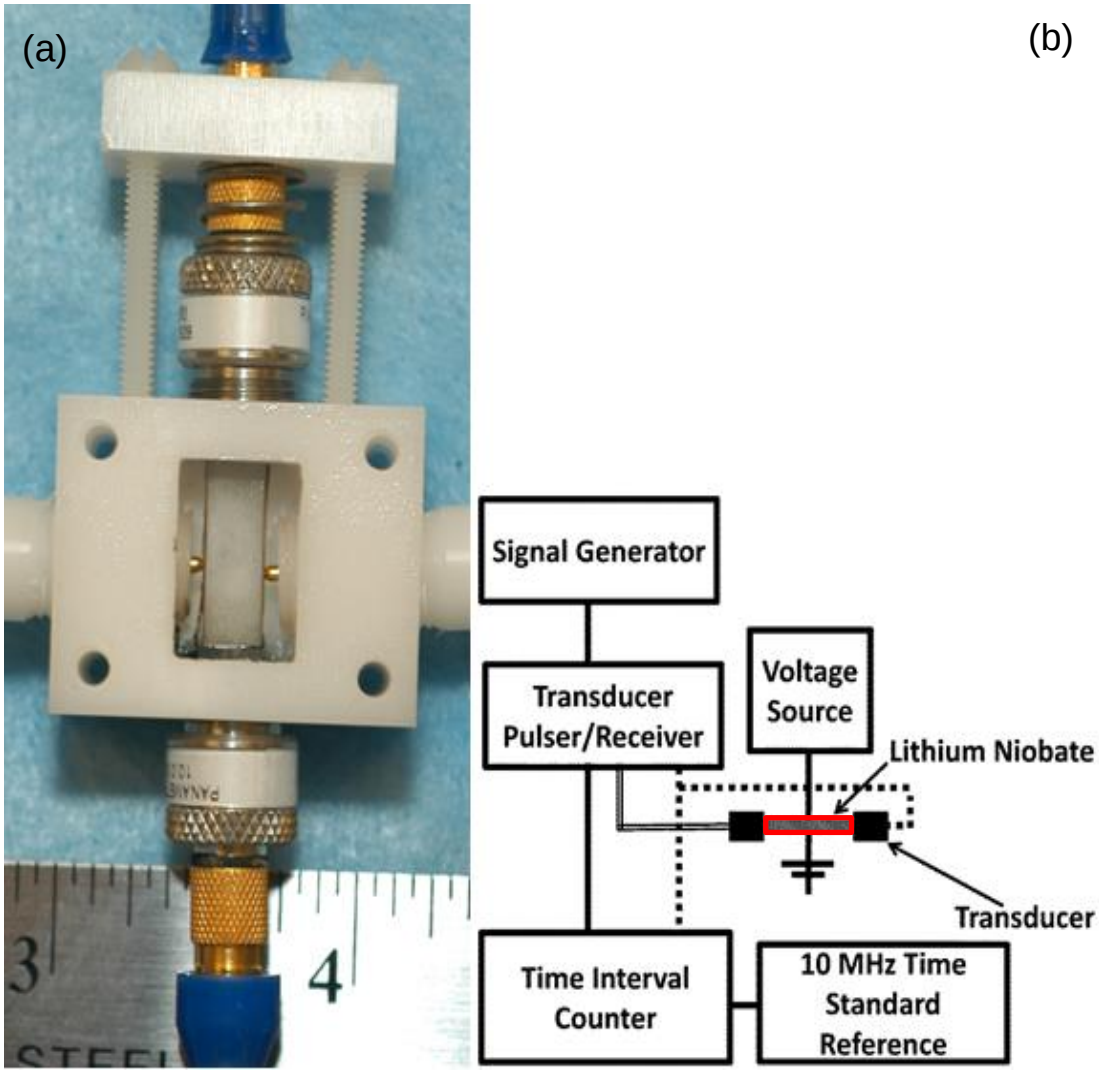

Figure 2.4.2: (a) Crystal fixture for $LiNbO_3$ crystal with mounted transducers. (b) Experimental setup with integrated HV sensor. The rectangle outlined in red represents the $LiNbO_3$ crystal. The black solid boxes represent the transmitting and receiving acoustic transducers.

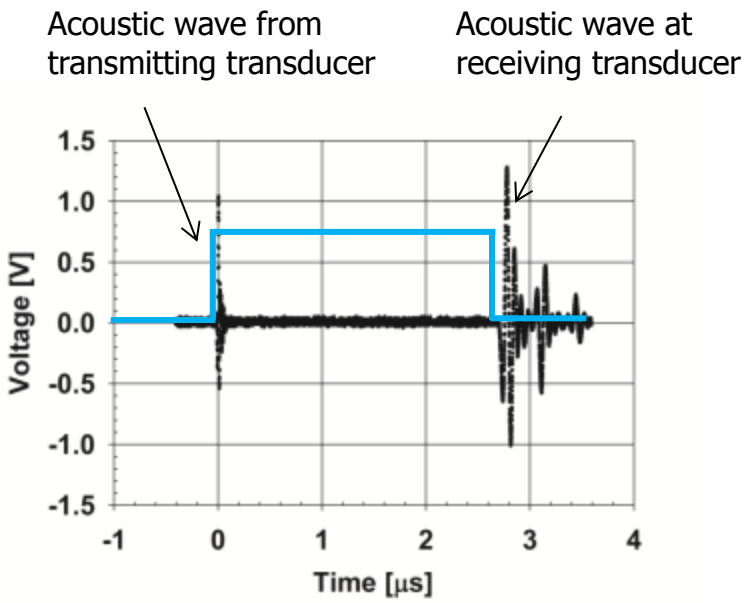

Figure 2.4.3: Time dependent voltage transducer response output making a single propagation through the 15 mm $LiNbO_3$ crystal. The pulse designated in blue is the timing gate which defines the propagation time measured by the TIC.

2.5 EXPERIMENTAL DATA ON SINGLE AND MULTIPLE PASS MEASUREMENTS

Figure 2.6.1(a) shows the DC voltage results for applied voltages between 128 V-1,100 V at steps of 128 V compared with calculated values from equation 1.9.1 in chapter 1. A linear relationship between the applied voltage and the acoustic time delay is in good agreement without the need for temperature compensation or any additional signal processing. The data from Figure 2.6.1(a) ranged from -2.6 to -17.2 ps. The error bars represent the combined standard deviation of the mean for 10 measurements at the stated applied voltage. The standard deviation ranged from 2 to 6 ps. To increase the sensor's signal-to-noise ratio (SNR), all acoustic pulses prior to the 5^{th} pass acoustic wave were gated out. Figure 2.6.1(b) shows that a voltage dependent increase in SNR is observed when monitoring the 5^{th} pass acoustic wave versus that of a single pass. It was

observed that the response was 5.1 times the single pass response. Subsequent passes (7^{th} and above) required significant amplification that reduced the SNR. The data for the calculated values was determined by using the calculations from equation 3 using $d_{21} = -2.48 \times 10^{-11}$ m/V. This particular coefficient corresponds to compressive strain. The d_{21} term is found by using the material data from Kovacs *et al.* and using the Bond transformation matrix formulation found according to Auld with Euler angles (90°, 90°, 36°) [55,92,93]. The time delay due to the voltage strain is calculated after inferring the change in crystal length, ΔL, from the applied voltage and d_{21} term.

2.6 DISCUSSION ON BAW VOLTAGE SENSOR

Due to the strong electric fields in this work (2.56×10^4 V/m to 2.20×10^6 V/m) nonlinearities are expected to be present in the data [94]. The reported data deviated slightly from the linear theory described in 1.8. The slight deviation from linear theory can be attributed to using the empirically calculated d_{21} value to calculate the time delay. Data reported in the literature has observed even larger differences in the measured versus empirically calculated piezoelectric constant [78].

Since the crystal is 15 mm thick, the nonlinearity could be possibly dampened by the time the acoustic wave has propagated the full distance through the crystal. The sensitivity of the 1^{st} pass and 5^{th} pass data obtained in our measurements was 17 fs/V and 87 fs/V, respectively.

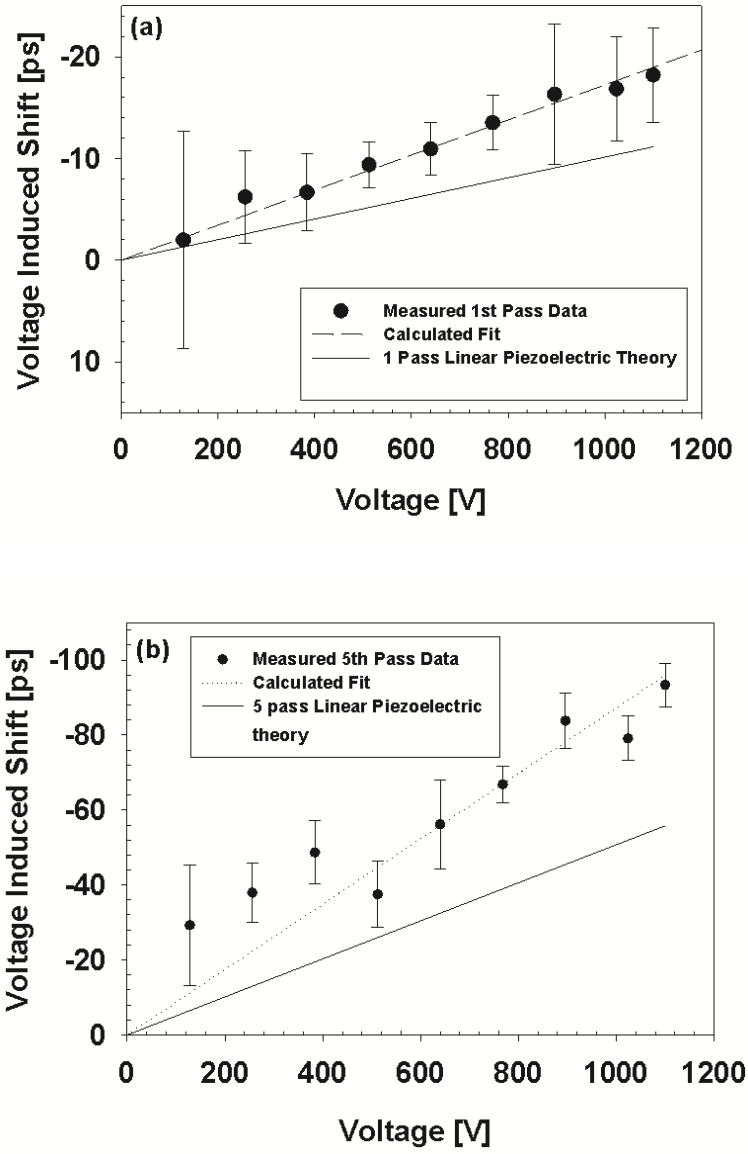

Figure 2.6.1: (a) Voltage induced shift vs. voltage applied to the crystal for measured values from a single pass acoustic wave and theoretically calculated values using linear piezoelectric theory. (b) Measured values from an acoustic wave making five passes in the crystal. The increase in voltage induced shift is 4-5 times, depending on voltage.

2.7 CONCLUSIONS ON BAW VOLTAGE SENSOR

In summary, DC voltages were measured using a compact piezoelectric voltage sensor by monitoring acoustic wave propagation time changes with applied

voltage in bulk $LiNbO_3$. It was shown that the measured crystal responses are linear but do not align well with linear piezoelectric theory. Multiple pass measurements were also performed and an increased sensitivity was achieved. The increased sensitivity from multiple pass measurements scaled linearly compared to single pass measurements.

3 COMPARATIVE STUDY OF 0° X-CUT AND Y+36°-CUT $LINBO_3$ HIGH-VOLTAGE SENSING

3.1 INTRODUCTION

This chapter extends the BAW sensor's capabilities to measure DC, AC, and pulsed voltage signals. The results from two different $LiNbO_3$ crystal orientations were compared to determine the role of acoustic mode propagation on sensor performance. A 1-D impedance matrix method was utilized to compare with the DC measurements based on calculating the strain as the input to the model. The 1-D impedance method is based on a three port circuit–two acoustic ports that sandwich an electrical port [95]. The electrical port was comprised of multiple impedance layers. Voltage-induced strain effects were implemented in the model by adding an incremental length ΔL to the nominal crystal length. The incremental length was calculated using a simplified version of the piezoelectric constitutive relationship that relates total strain of the crystal to the strain generated by an applied electric field:

$$S = \frac{\Delta L}{L} = d_{ij} E_i \tag{3.1.1}$$

where d_{ij} is the linear piezoelectric strain coefficient, E_i is the electric field, ΔL is the incremental change in length due to strain generation, and L is the nominal crystal length. Due to the rectangular crystal geometry and electrode positions, equation 3.1.1 was used to relate the total strain to the applied voltage using the relationship $V=EL$. The ΔL was determined for DC voltages ranging from 256–

1,100 V for both crystal cuts. The d_{ij} terms contributing to ΔL depended on the acoustic wave propagation and applied voltage, V, directions:

$$\Delta L = d_{ij} V \tag{3.1.2}$$

3.2 CHRISTOFFEL'S EQUATION

The Christoffel equation describes anisotropic elastic waves in classical elastic theory. The solutions of this equation show differences in acoustic propagation with respect to different electrical polarizations. The complexity of the solutions depends upon the crystal class. Lithium niobate is in the 3m crystal class (Hermann-Mauguin notation) which is part of the trigonal crystal system. The Christoffel equation takes advantage of the equation of motion which relates stress acting on a point in a solid to the motion of particles in the solid:

$$k^2 \left(l_{iK} \left\{ C_{KL}^E + \frac{[e_{Kj} l_j][l_i e_{il}]}{l_i \varepsilon_{ij}^S l_j} \right\} l_{Lj} \right) v_j = \rho \omega^2 v_i \tag{3.2.1}$$

where k is the wavenumber, l is the propagation vector, v is the phase velocity, C is the elastic constant, ε is the electrical permittivity, e is the stress-charge form piezoelectric constant, ρ is the density, and ω is the angular frequency. The subscripts indicate summation over the dimensions of the coordinate system. Equation 3.2.1 is known as the Christoffel equation. The derivation of this equation can be found in textbooks [55]. Eigenvalue solutions to this equation yield phase velocities of all possible wave modes for a particular phase velocity direction.

3.3 0° X-CUT CRYSTAL CHRISTOFFEL SOLUTIONS

As described in chapter 1, a 0° X-Cut crystal is a crystal whose polarization orientation is in the X-direction, and orthogonal to the YZ plane. Figure 3.3.1 shows a schematic of the crystal with the copper ribbon wrapped around the perimeter of the crystal.

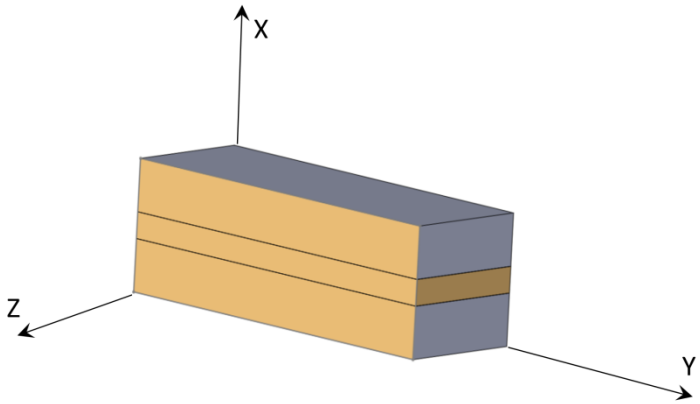

Figure 3.3.1: Schematic of 0° X-Cut $LiNbO_3$ crystal. A 3 mm wide 1 mm thick copper ribbon was wrapped around the crystal to excite longitudinal waves which propagate along the XY plane. Faces indicated by the gold color designate electrodes. The dimensions of the crystal are nominally 15.0 mm × 5.0 mm × 5.0 mm with gold electrodes of a nominal 15 mm × 5 mm × 0.35 μm.

Figure 3.3.2 plots the electrical to acoustic energy conversion, k_t, within the crystal as a function of propagation angle in the crystal. Figure 3.3.2(b) shows the slowness curve for the different modes associated with this crystal. The longitudinal wave is denoted by the red curve and the mode solution yields a theoretical velocity of 6572 m/s (green and blue curves are shear wave modes). X-cut $LiNbO_3$ has no piezoelectric coupling at 0° for a longitudinal mode but has an acoustic phase velocity at this angle. This means that the longitudinal mode

propagating at this angle is a purely elastic mode. The electrode configuration for this crystal is shown in Figure 3.3.1.

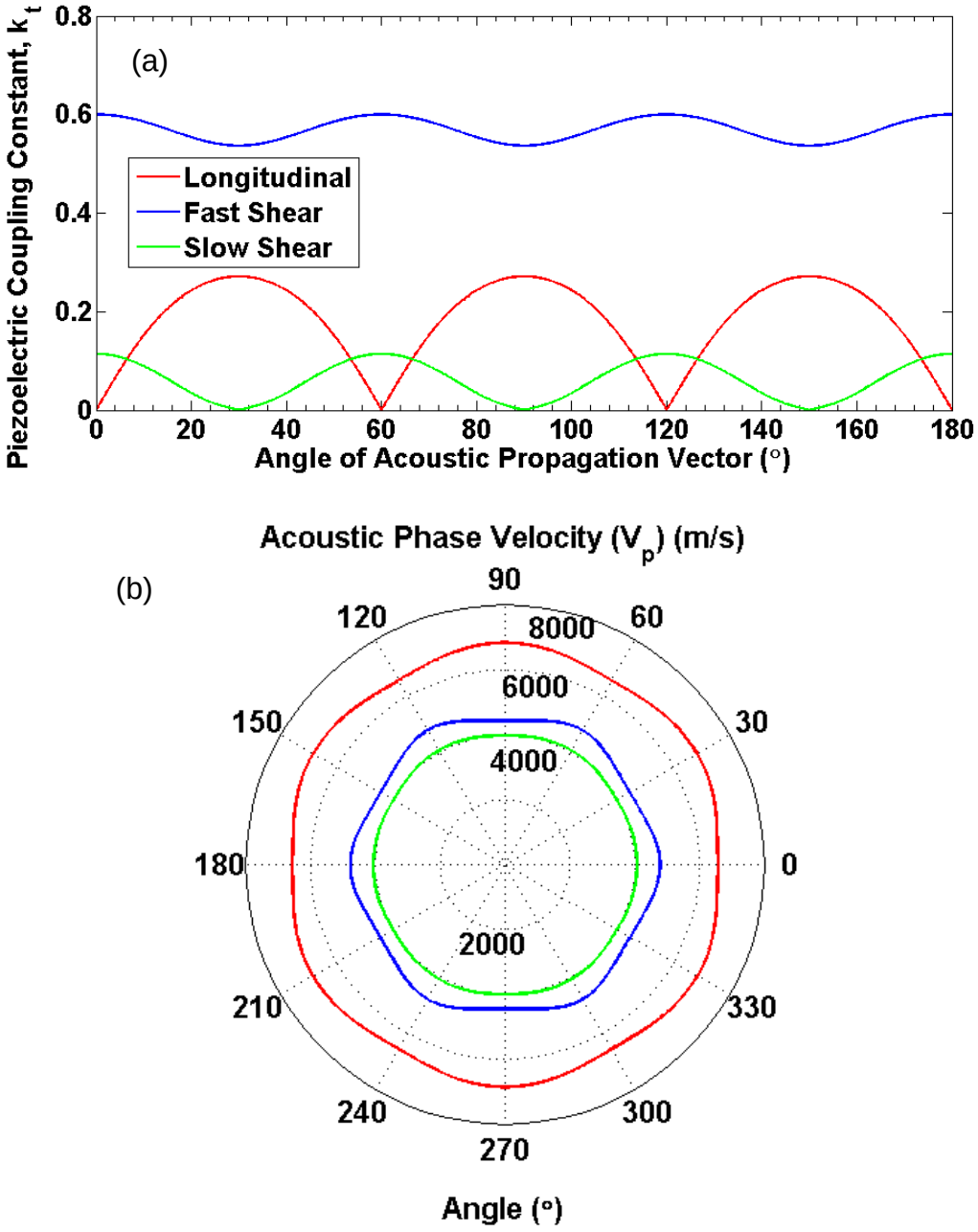

Figure 3.3.2: Solutions from solving Christoffel's equation. a) Piezoelectric constant, k_t vs. acoustic propagation vector angle for X-cut $LiNbO_3$. b) The corresponding slowness curve. The longitudinal mode is denoted by the red curve. The green and blue curves represent shear wave modes.

3.4 Y+36°-Cut Crystal Christoffel Solutions

Figure 3.5.1 describes the electrical to acoustic energy conversion, k_t, within the crystal as a function of propagation angle in the crystal. Figure 3.5.1(b) shows the slowness curve for the different modes associated with this crystal. The longitudinal wave is denoted by the red curve and the mode solution yields a theoretical velocity of 7340 m/s (green and blue curves are shear wave modes). This crystal cut was tested to take advantage of the single longitudinal mode that operates at 36°, which is marked in the figure. The electrode configuration for this crystal is shown in Figure 3.4.1.

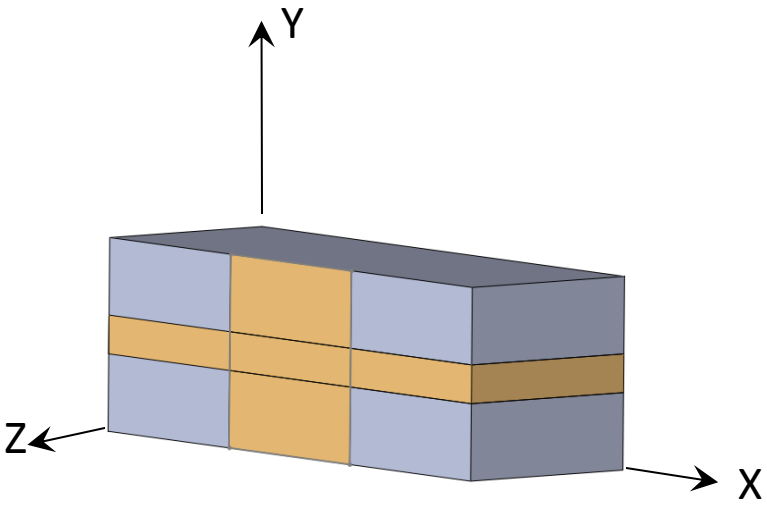

Figure 3.4.1 Schematic of Y+36°-cut $LiNbO_3$ crystal with copper ribbon. Ribbon that wraps around the crystal represents electrode to excite longitudinal waves. The dimensions of the crystal are nominally 15.0 mm × 5.0 mm × 5.0 mm with gold electrodes of a nominal 5 mm × 5 mm × 0.35 μm.

3.5 Experimental Setup for Longitudinal Wave Measurements

The BAW HV sensor operates by measuring the velocity of a propagating acoustic wave in real-time while a voltage is applied across the crystal. The

Y+36°-cut and 0° X-cut crystals both have dimensions 15 mm × 5 mm × 5 mm. The crystal cuts were verified using acoustic velocity measurements. The measured acoustic velocities were validated by solving the Christoffel equation [55]. The measured acoustic velocity for the Y+36°-cut crystal was 7328 m/s ± 37 m/s and for the 0° X-cut crystal was 6700 m/s ± 200 m/s. Both crystals were wrapped with a ~50 μm thick copper strip across the 15 mm crystal length to generate longitudinal strain due to the applied voltage. Consequently, shear strain was induced in the 5 mm Y-direction.

The experimental setup found in chapter 2 was also used for the longitudinal wave measurements. As before, two transducers were placed on either side of the crystal which transmitted and received acoustic pulses. The operating frequency of the transducers was centered at 10 MHz, having a bandwidth of 5 MHz, with a 3 mm outer diameter. The transducers were controlled using a PR system (Olympus Corporation). The PR system was synchronized to a TIC (Stanford Research Systems) using a 10 MHz reference signal. The PR system was used to transmit and condition the received acoustic pulses to determine the ToF. A 300 MHz oscilloscope (Tektronix Corporation) was used to digitize the conditioned signal from the receiver.

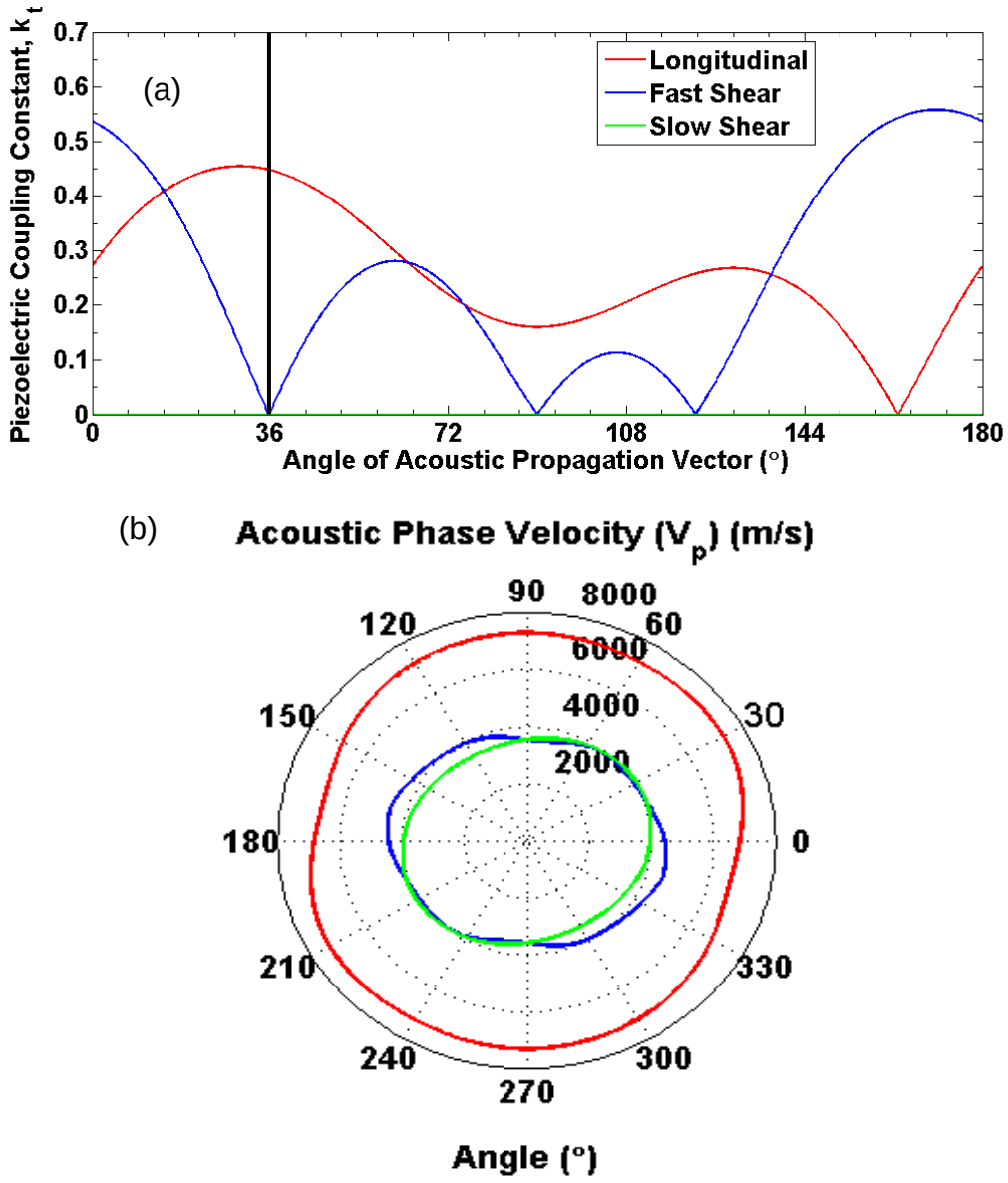

Figure 3.5.1: Solutions to Christoffel's equation. a) Piezoelectric constant, k_t vs. acoustic propagation vector angle for Y+36°-cut $LiNbO_3$. b) The corresponding slowness curve. The longitudinal mode is denoted by the red curve. The green and blue curves represent shear wave modes.

AC, DC, and pulsed voltages were applied to the crystal to determine the relationship between the voltage sources and their acoustic propagation time delays. The DC and AC voltages were derived from an identical source (Fluke Corporation), producing DC voltages up to 1,100 V and AC voltages up to 640 V

at 100 kHz. For pulse measurements, a pulse generator (Berkeley Nucleonics) produced voltages up to 800 V with a 5 μs pulse width. A 50 Ω, 100 W rated non-inductive resistor (Vishay Dale NH-100) was placed in parallel with the sensing element so that the total load impedance closely matched the 50 Ω output impedance of the pulse generator.

A 1 V, 1 kHz pulse (Agilent 33250A) triggered the PR system. The crystal was mounted and the transducers were aligned until the receiving pulse signal amplitude was maximized. Two 0.5 mm thick pieces of glass were added to both ends of the crystal to add electrical isolation between the transducer casing and copper strip. Glycerin couplant was used to reduce the acoustic impedance mismatch between the transducer elements, glass, and $LiNbO_3$ crystal. For AC and DC measurements, the time interval was recorded while increasing the applied voltage. For AC and DC measurements, this cycle was repeated 5 times at each voltage and frequency. For pulsed measurements, 10 single event pulses with 5 μs duration were applied to the crystal. A TIC measured the acoustic delay time between the transmitting and receiving transducer before, during, and after an applied voltage to the crystal.

3.6 CRYSTAL RESPONSES FROM DC, AC, AND PULSED VOLTAGE

Each measurement was performed within an ambient temperature of 23 °C ± 1 °C with no temperature compensation, where the temperature change was less than ± 0.2° C. The DC measurements were performed at 256 V, 384 V, 512 V,

640 V, 768 V, 896 V, 1,024 V, and 1,100 V. The AC measurements were performed at 640 V at frequencies of 100 Hz, 1 kHz, 10 kHz, and 100 kHz.

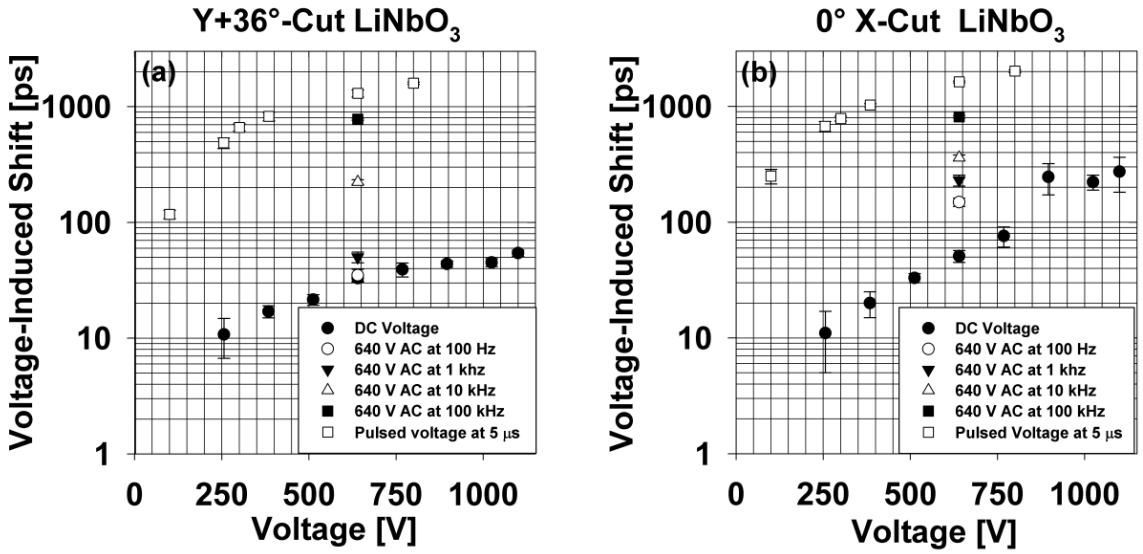

Figure 3.6.1: Voltage-induced shift in time vs. applied voltage for AC, DC, and pulsed voltages for the (a) Y+36° and (b) 0° X-cut $LiNbO_3$ crystals. For AC measurements the voltage was fixed at 640 V. For pulsed measurements the pulse width was 5 μs.

Figure 3.6.1 shows AC, DC, and pulsed voltage results for the two crystal cuts. The DC measurements were performed at 256 V, 384 V, 512 V, 640 V, 768 V, 896 V, 1,024 V, and 1,100 V. The AC measurements were performed at 640 V at frequencies of 100 Hz, 1 kHz, 10 kHz, and 100 kHz. From Figure 3.6.1(a), the Y+36°-cut crystal response ranged from 10–54 ps over the DC voltage range and 35–778 ps for the AC voltage case. The standard deviation ranged from 2–4 ps for the DC measurements and 4–16 ps for AC measurements. Figure 3.6.1(b) shows the results of the 0° X-cut crystal, which had a response of 10–273 ps for DC voltages and 189–813 ps for AC voltage. For the X-cut crystal, the standard deviation ranged from 6–91 ps across all of the DC voltage measurements and 12–25 ps for all the frequencies tested during the AC measurements. Figure

3.6.1 is a semilog plot and masks the trend observed in the AC measurements, which was quadratic for both crystal cuts.

For the pulsed configuration, the applied voltages 100, 255, 300, 385, 640, and 800 V with a pulse width of 5 μs, were chosen to facilitate comparison between DC and AC measurements. In this case, the 0° X-cut $LiNbO_3$ crystal response varied from 0.250–2 ns with a measured standard deviation ranging from 36–53 ps. The Y+36°-cut crystal response was 0.115–1.6 ns with a measured standard deviation of 9–70 ps. An uncertainty budget for these measurements was calculated and this information can be found in Appendix A3.

3.7 1-D Impedance Matrix Model Comparison to Experimental Data

The basic configuration of this model is a piezoelectric slab with a cross sectional area, *A*, and thickness, *h*. The 1-D model takes into consideration forces, F_1 and F_2, from adjacent materials acting on a piezoelectric slab while a voltage, V_{in}, is applied to it [95]. The 1-D impedance model consisted of three ports: two acoustic ports and one electrical port. The forces are related to the electrical impedance as follows:

$$F_1 = -AT(z_1) = Z_1 v_1 \tag{3.7.1}$$

where *T* is the traction per unit area, Z is the electrical impedance, and v_1 is the velocity. The force F_2 is similarly defined with the appropriate numerical subscript. Equation 3.7.1 can be further expanded by:

$$Z_1 v_1 = Z_1\left(ae^{-ikz_1} + be^{-ikz_1}\right) - i\frac{h}{\omega}I \tag{3.7.2}$$

where *h* is the thickness of each slab, and *I* is the current intensity across the z_1 and z_2 plane, and *a* and *b* are dummy variables. Using v_1 and v_2 (which is defined similarly to v_1), and simultaneously solving for *a* and *b,* F_1 and F_2 can be rewritten as:

$$F_1 = Z_1\left(\frac{v_1}{i\tan kd} + \frac{v_2}{i\sin kd}\right) + \frac{h}{i\omega}I \tag{3.7.3}$$

$$F_2 = Z_1\left(\frac{v_1}{i\sin kd} + \frac{v_2}{i\tan kd}\right) + \frac{h}{i\omega}I \tag{3.7.4}$$

Electrically, the slab is modelled like a parallel plate capacitor with displacement current from each adjoining material:

$$V_{in} = \frac{e}{i\omega\epsilon^S}[v_1 - v_2] + \frac{I}{i\omega C_o} \tag{3.7.5}$$

where *e* is the piezoelectric voltage constant, ϵ^S is the dielectric permittivity of the material under constant stress *S*, and *I* is the current. Using equations 3.7.1, 3.7.4, 3.7.5, and 3.7.6 a matrix can be written:

$$\begin{pmatrix} i\mathbb{Z}_1 + \frac{\mathbb{Z}_M}{\tanh(kd)} & \frac{\mathbb{Z}_M}{\sinh(kd)} & e/(\omega\epsilon^S) \\ \frac{\mathbb{Z}_M}{\sinh(kd)} & i\mathbb{Z}_1 + \frac{\mathbb{Z}_M}{\tanh(kd)} & e/(\omega\epsilon^S) \\ e/(\omega\epsilon^S) & e/(\omega\epsilon^S) & \frac{1}{\omega C_o} \end{pmatrix} \begin{pmatrix} v_1 \\ v_2 \\ I_1 \end{pmatrix} = \begin{pmatrix} 0 \\ 0 \\ iV_1 \end{pmatrix} \tag{3.7.6}$$

Using equation 3.7.6, the electrical impedance and velocities were calculated from successive impedances due to each layer loading the face of the transducer. Figure 3.7.1: 1-D impedance model of a composite piezoelectric slab of thicknesses, *d* and cross sectional area, *A*. The forces that are applied to each area are designated by F_1 and F_2, and are applied at velocities v_1 and v_2, respectively. shows a schematic of the model.

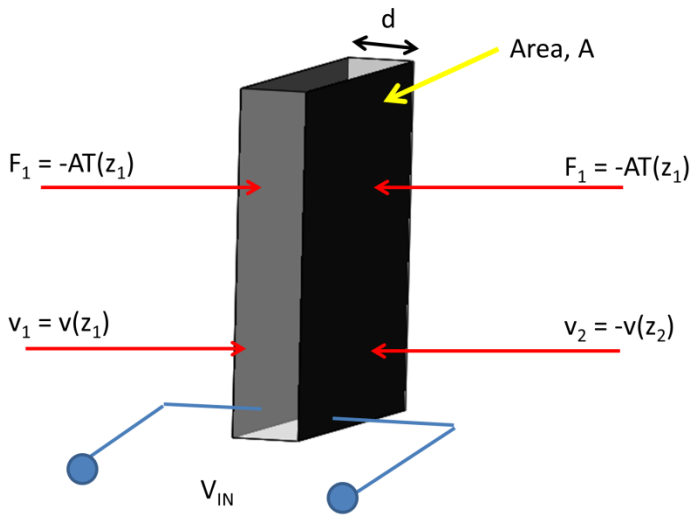

Figure 3.7.1: 1-D impedance model of a composite piezoelectric slab of thicknesses, *d* and cross sectional area, *A*. The forces that are applied to each area are designated by F_1 and F_2, and are applied at velocities v_1 and v_2, respectively.

The model takes in each impedance layer that is placed on the transducer and calculates its impedance. Firstly, the substrate impedance is calculated, which in this case the $LiNbO_3$ transducer, and the resonance/antiresonance peaks are calculated. Second, the model then calculates each successive impedance layer that is placed on the transducer. Thirdly, the combined impedance of the transducer and layer is calculated, and this is done in a recursive fashion to obtain the final effective impedance at the face of the transducer. Figure 3.7.2 shows the multilayer structure inputted into the impedance model. Termination of

the acoustic ports allowed for calculation of the electrical impedance of the overall structure. The transducer was a 370 μm thick Y+36°-cut $LiNbO_3$, which generated a 9.91 MHz acoustic wave. Using Y+36°-cut reduced the impedance mismatch between the transducer and the crystal interface. The layers loading the transducer were: 1) 0.5 mm Pyrex, 2) 15.0 mm $LiNbO_3$, and 3) 0.5 mm Pyrex. An inverse fast Fourier transform was used to convert the frequency-domain to the time-domain. The first zero crossing before the maximum peak in the time-domain was determined using a linear fit. The zero crossing time was dependent on the voltage applied to the crystal. The voltage-induced time shift was determined by taking the different zero crossing times and comparing them to the case with zero applied voltage to the crystal.

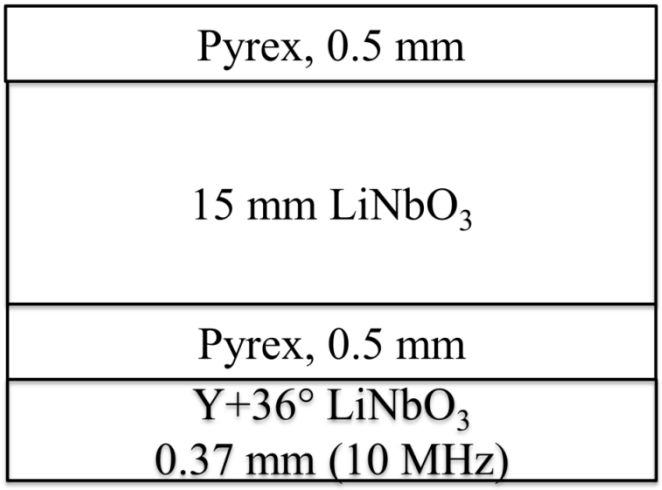

Figure 3.7.2: A schematic of the multilayer structure used for 1-D impedance matrix model. The substrate material used in this simulation was Y+36°-cut $LiNbO_3$ to mitigate impedance mismatch.

The best-fit d_{ij} terms were used to validate the DC experimental data for each crystal. The material constants were obtained from the unrotated values in Kovacs *et al.* and were appropriately rotated using the Bond transformation

matrix formulation according to Auld [55,92]. The Euler angles associated with the 0° X-cut crystal and Y+36°-cut crystal are (90°, 90,° 0°) and (90°, 90,° 36°), respectively [69]. Using equation 3.1.2, the incremental length change of the crystal for a specific applied voltage was calculated and inserted into the model. Figure 3.7.3 shows the results for both crystals. Figure 3.7.3(a) shows that, for the 0° X-cut crystal, the longitudinal mode d_{11} and shear mode d_{61} terms describe the measured crystal response. For Case A in Figure 3.7.3(a), it was found that between 256 V–512 V, a longitudinal mode with d_{11} term explained the measured data. Case B describes the voltage range of 512 V–768 V, where a fraction of both the d_{11} and d_{61} term, both longitudinal and shear modes, contributed to the response. For Case C, or voltages > 768 V, both d_{11} and d_{61} terms fully contributed to the response. A linear summation of the total strain generation by using multiple d_{ij} terms to explain the measured data has been previously used in frequency dependent measurements [74]. In Figure 3.7.3(b), the d_{11} and d_{43} term were used to model the measured response from the Y+36°-cut $LiNbO_3$ crystal. The d_{11} and d_{43} terms corresponded to the longitudinal and shear wave piezoelectric coefficient terms, respectively.

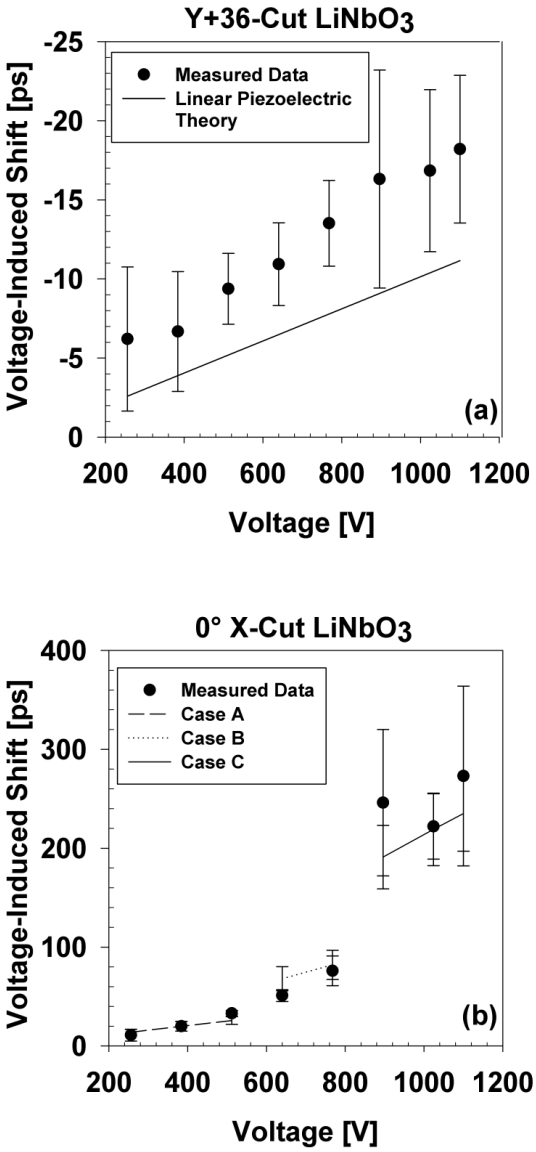

Figure 3.7.3: Measured response of (a) 0° X-cut $LiNiBO_3$ and (b) Y+36°-cut $LiNiBO_3$ for DC voltage between 256 V-1,100 V. The ΔL term was used as the model input. For (a), the d_{11} and d_{43} terms were used to determine ΔL. For (a), Case A used the d_{11} term to calculate ΔL. Case B used 50% of the d_{11} term and 50% of the d_{61} term to calculate ΔL. Case C uses the full d_{11} and d_{61} term to calculate ΔL.

3.8 **DISCUSSION**

Applying a DC voltage to a piezoelectric crystal resulted in a static deformation; however, the crystal did not continuously change stress as in the case when

using AC or pulsed voltages. Furthermore, larger time shifts were observed for the pulsed voltage case, where the crystal interacted with all frequencies greater than 200 kHz, including the resonant frequency for both crystals. For pulse measurements, a 32-fold increase in response versus that of DC voltage measurements at 640 V for the X-cut crystal and 39-fold increase for the Y+36°-cut crystal were observed. Figure 3.6.1 indicates that the acoustic delay time shift was dependent on the source frequency and pulse duration; however, additional studies are required to determine the role of the energy dose of the acoustic pulse.

Figure 3.7.3 shows the comparison between the DC responses for each crystal and the 1-D impedance matrix model. The DC experimental data for the X-cut $LiNbO_3$ crystal was linearized for different voltage ranges and showed good agreement with the 1-D impedance matrix model. Discrepancies observed between the measured and calculated time-delay for the Y+36° crystal were attributed to the empirically calculated d_{11} and d_{43} values in the time delay. Previous literature reports cite even larger differences when comparing measured versus empirically calculated piezoelectric constants [74,78]. In Figure 3.7.3(b), the discrepancy between the measured data and the theoretical line is likely attributed to non-linear effects of the lithium $LiNbO_3$ crystal. The AC and pulse measurements appeared to be dependent on the energy dose of the acoustic pulse as well as the source frequency, suggesting a possible nonlinear relaxation of the $LiNbO_3$ crystal in addition to effects from a nonlinear piezoelectric tensor [96].

3.9 CONCLUSION

Measuring high-voltage using DC, AC, and pulsed sources involves consideration of the source and its impedance. A comparison of two $LiNbO_3$ crystal cuts was made to determine their performance as a voltage sensor. The crystal response from each crystal was measured after applying DC, AC, and pulsed voltages to each crystal. From the three voltage types measured, the largest crystal response was observed when performing pulsed measurements. The temperature dependence of the acoustic propagation time was monitored and shown to have a negligible effect on the measured response. The DC voltage experimental data was compared to a 1-D impedance matrix model for both crystal cuts and showed good agreement for the X-cut crystal and to a lesser extent for the Y+36° crystal.

4 TEMPERATURE AND PRESSURE EFFECTS ON HV SENSOR FOR AMBIENT CONDITIONS

4.1 INTRODUCTION TO TEMPERATURE COEFFICIENT MEASUREMENTS

Unlike some piezoelectric crystals that have temperature stable crystal cuts, all $LiNbO_3$ cuts are sensitive to temperature. As mentioned in chapter 2, $LiNbO_3$ is used in several applications such as pressure and temperature sensors [97,98]. For acoustic sensor applications, the temperature coefficient of delay (TCD) of $LiNbO_3$ is an important parameter to consider during the design phase. To monitor how temperature fluctuations affect the measurement, the TCD was measured for two different crystal cuts used in chapter 3.

4.2 TEMPERATURE COEFFICIENT OF DELAY

The TCD only depends on a two measurable quantities: the temperature coefficient of expansion (TCE) of the material and the temperature coefficient of velocity (TCV). The following equation was used to calculate the TCD:

$$TCD = TCE - TCV \tag{4.2.1}$$

where TCE is defined as:

$$\mathrm{TCE} = \alpha = \frac{1}{L}\frac{\Delta L}{\Delta T} \tag{4.2.2}$$

and TCV is defined as:

$$\mathrm{TCV} = -\frac{1}{v_p(T_r)}\frac{v_p(T_1) - v_p(T_2)}{(T_1 - T_2)} \qquad 4.2.3$$

For TCD measurements on the 0° X-cut and Y+36° $LiNbO_3$ crystals, T_1 *and* T_2 were 18° C and 32° C, respectively. The reference temperature, T_r, used was the ambient laboratory temperature of 23° C. Using this information, equation 4.2.3 is modified as follows:

$$\mathrm{TCD} = \alpha - \frac{1}{\mathrm{v_p}(23\ ^\circ\mathrm{C})}\left(\frac{(\mathrm{v_p}(32\ ^\circ\mathrm{C}) - \mathrm{v_p}(18\ ^\circ\mathrm{C})}{14\ ^\circ\mathrm{C}}\right) \qquad 4.2.4$$

A measured TCE value of 14.5×10^{-6}/ °C from the literature was used to complete the TCD calculation [99].

4.3 RESISTIVE TEMPERATURE DETECTOR

A resistive temperature detector (RTD) with platinum resistive element was used for this experiment (Omega Engineering). For the TCD experiments, a single four-wire RTD was employed to negate the impact of lead resistance on the temperature measurement. The specifications for the four-wire RTD are shown in Table 4.3.1.

Table 4.3.1: Parameters for 4 wire RTD used to measure the temperature of the $LiNbO_3$ crystal.

RTD Parameters	
Model	OMEGA Engineering SA1-RTD
Standards Met	DIN/IEC 60751
Temperature Range	-73C to 260 °C Continuous
Resistor Material	Class A
Nominal Resistance	100 Ω at 0 °C
α_r	0.00385 Ω/Ω °C
Manufacturer's Stated Accuracy / Stability	±0.15°C at 0 °C / < 0.2 °C drift/year
Self-Heating Effect	2.5 mW/°C

4.4 TEMPERATURE CONTROLLED ENVIRONMENT

A temperature controlled air bath (Measurements International) with stability of 15 mK for a ± 2 °C change in ambient temperature and a ramp rate of 0.25 °C/min was used for all temperature measurements.

4.5 EXPERIMENTAL SETUP FOR MEASUREMENT OF TEMPERATURE COEFFICIENTS

The temperature was swept from 18 to 32 °C in a temperature controlled air bath with a Type-T RTD placed inside the fixture and adhered to the crystal. A reference probe inside the air bath but just outside the fixture was present to determine if the system's temperature had reached equilibrium (Brunson Engineering). Furthermore, the temperature was allowed to equilibrate inside

with the air temperature for at least 4 hours prior to taking readings. Figure 4.5.1 shows a schematic for the experimental setup.

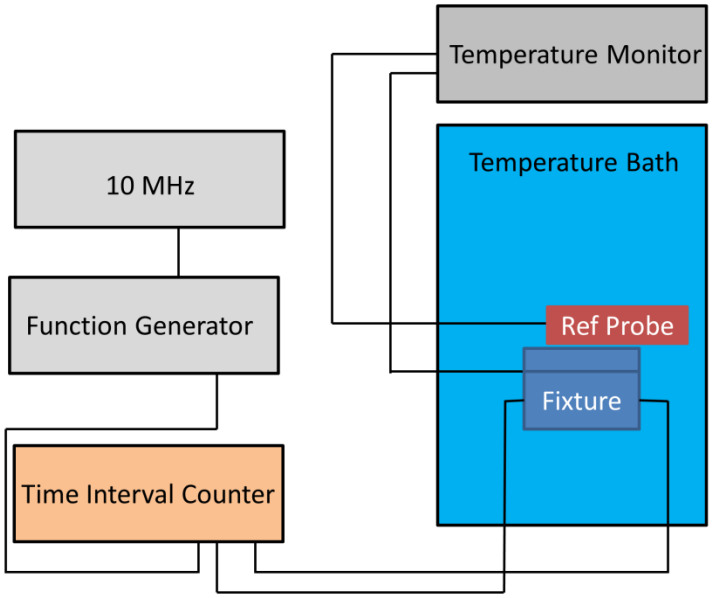

Figure 4.5.1: Schematic setup of the resistive bath. The RTD was bonded to the crystal and completely enclosed inside the fixture. A metrology grade temperature reference probe was placed next to the fixture inside the bath as a secondary reading.

To determine the source heating effect's influence on the crystal response, a 1,100 V DC signal was applied for 1 hour to the crystal. The amount of energy deposited into the crystal for this time was calculated to be ~669 J (0.185 W) based on bulk crystal properties. The specific heat equation, $Q = m_c c_v \Delta T$, was used to determine the amount of temperature change for the amount of energy dissipated, where Q is the energy, m_c is the $LiNbO_3$ mass, c_v is the volumetric specific heat of $LiNbO_3$, and ΔT is the temperature change that was calculated to be ΔT=0.01 °C. To make this rough calculation, it was assumed that no heat dissipated from the crystal.

4.6 TEMPERATURE STABILIZATION CONSIDERATIONS

To achieve complete temperature stabilization prior to measurement, a wait time of two hours was used. This time was determined using a lumped capacitance thermal analysis model, which is valid for a small Biot number, designated by *Bi*. $LiNbO_3$ Biot number was determined using:

$$Bi = \frac{L_c h}{k} \tag{4.6.1}$$

where L_c is the characteristic length, h is the convective heat transfer coefficient of air, and k is the thermal conductivity of $LiNbO_3$. Lithium Niobate's *Bi* was determined to be 0.004. Since *Bi* < 0.01, the lumped capacitance model for transient heat transfer model can be used [100]:

$$T(t) = T_\infty + (T_i - T_\infty)e^{-\left(\frac{ht}{\rho C L_c}\right)} \tag{4.6.2}$$

where T_i is the initial temperature, t is time in seconds, ρ is the density of $LiNbO_3$, C is the specific heat capacity of $LiNbO_3$ solid, and T_∞ is the ambient temperature of the system. Figure 4.6.1 below shows the comparison between the measured data and the lumped capacitance model output, with the ambient temperature in approximately 60 minutes for both cases.

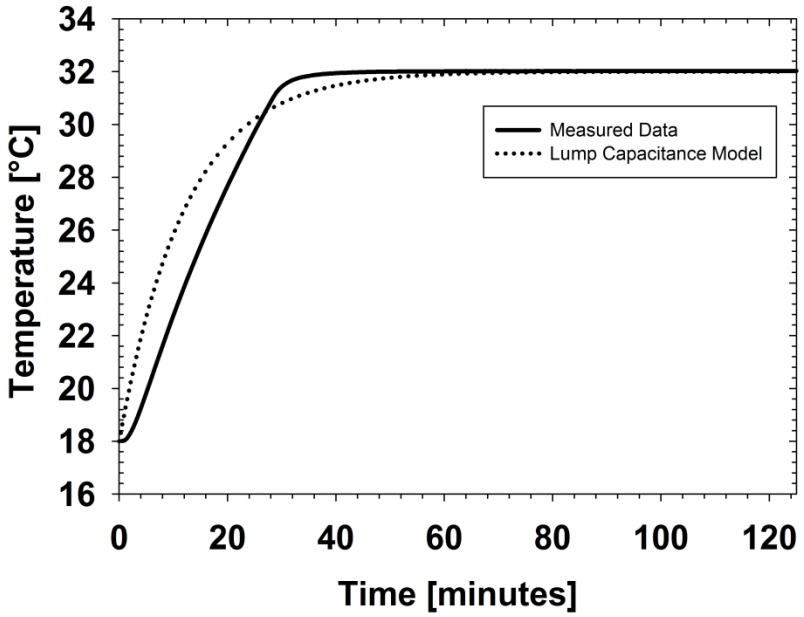

Figure 4.6.1: Comparison plot between the measured data and the lumped capacitance model output between 18 °C to 32 °C. Both the model and experimental data predict it takes approximately 60 minutes for the temperature of the bulk crystal has equilibrate with the bath.

The ambient temperature was closely monitored and a change within ± 0.2 °C was observed during each measurement. The laboratory temperature fluctuation corresponded to a time change of 49 ps. This time variation was not discernible in the acquired measurements, strongly suggesting that the temperature fluctuation of the crystal was negligible.

The thermal effects on acoustic wave propagation were measured by steadily sweeping the temperature in a controlled environment. A temperature sweep between 18 °C to 32 °C was performed using the aforementioned temperature controlled air bath. The temperature and acoustic propagation time stamps were acquired using computer data acquisition every 30 seconds using a standard Fluke 1529 Chub-E4 thermometer with a response time of (Fluke Corporation). The temperature error was dominated by the RTD error, which ranged from

2250–2810 ppm over the 18 °C to 32 °C range. The velocity change under thermal cycling illustrated in Figure 4.6.2 is consistent with publications in the literature that observed the same effect when characterizing ultrasonic attenuation in $LiNbO_3$ [101].

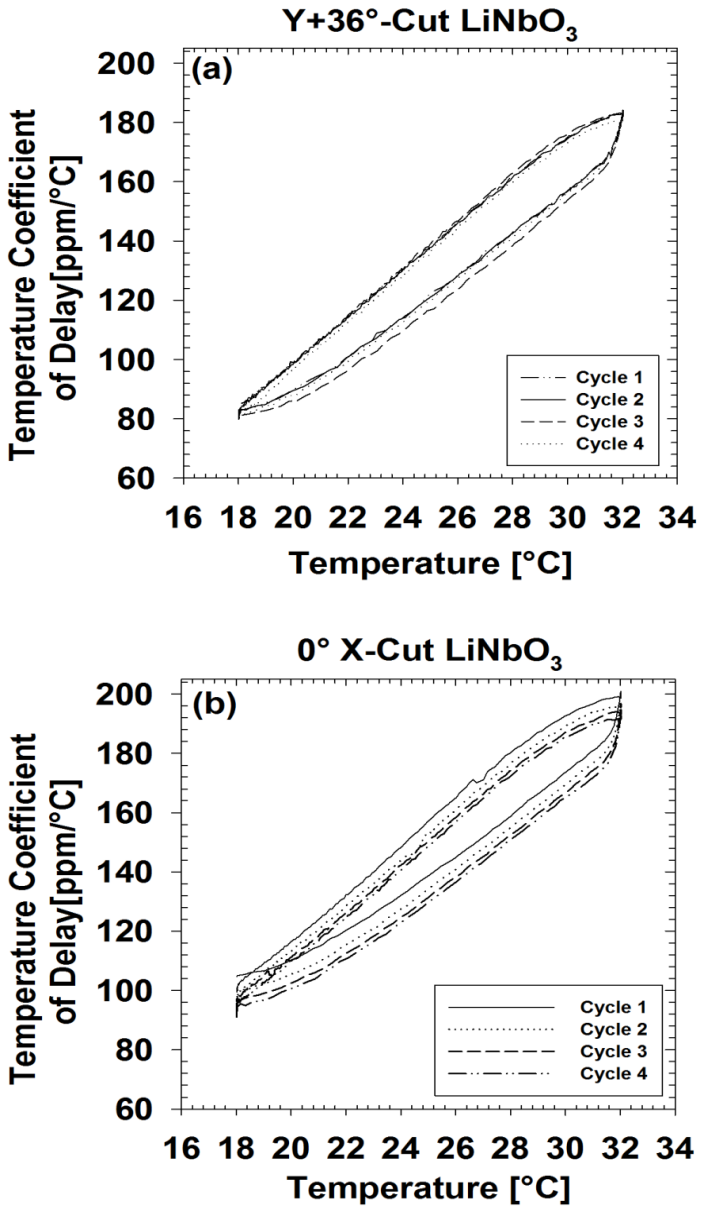

Figure 4.6.2: Measured TCD of $LiNbO_3$ over 18-32° C for (a) Y+36° and (b) 0° X-cut crystals. The total time for each cycle from 18-32° C and 32-18° C was 2 hours.

Specifically, the report showed that temperature changes affected the equilibrium of the crystal structure as a whole, causing the acoustic waves to see a different crystal structure under thermal cycling. Overlap is observed between the four cycles, which is captured by the measurement error.

4.7 EXPERIMENTAL DATA AND DISCUSSION

Figure 4.6.2 shows how a change in temperature affects the acoustic propagation time in both crystal cuts. The general method involves differentiating Christoffel's equation with respect to temperature and obtaining relationships for the temperature coefficients of fundamental electroacoustical constants in terms of partial derivatives of the effective elastic moduli. The velocity change under thermal cycling is consistent with reports in the literature that characterized ultrasonic attenuation in $LiNbO_3$ [101]. The average TCD for the Y+36°-cut and 0° X-cut crystal was measured to be 149.7 ppm/°C ± 1.9 ppm/°C and 157.3 ppm/°C ± 0.68 ppm/°C, respectively, using 4 up/down thermal cycles. These measured TCDs are consistent with published SAW and bulk TCD measurements that considered the second order effects of nonlinear elasticity, nonlinear piezoelectric effects, electrostriction, and the nonlinear electrical polarization [102,103].

Simplified TCD calculations are abundant in the literature where crystals at a given temperature were considered to maintain their crystallographic class, changing only their density and material constants. These assumptions cause a discrepancy between the theoretically calculated and measured TCD values for

strained crystals since the state of the crystal (i.e. the initial static deformation) requires considering all of the second order effects. Lower TCD values (i.e. 75-90 ppm/°C) reported in the literature were based on linear material temperature coefficients that neglected electrostriction and nonlinear effects such as electrical polarization [104,105]. Table 4.7.1 shows a comparison of calculated and experimental TCD values observed in SAW configurations. This table was reproduced from literature, which does not discuss uncertainty of the measurements [102].

Table 4.7.1: Comparison of values of TCD of SAW calculated by different methods using experimental data (this table was reproduced from Table I in [102]).

Calculated TCD	**$LiNbO_3$ (41.5° YX-cut)**	**$LiNbO_3$ (YZ-cut)**
Using nonlinear elastic and piezoelectric constants and electrostriction constants	160 ppm/°C	259 ppm/°C
Using only temperature coefficients for linear elastic, piezoelectric, and dielectric constants	75.4 ppm/°C	94.4 ppm/°C
Theory and experiment	~ 75 ppm/°C	~94 ppm/°C

4.8 $LiNbO_3$ Capacitance Coefficient of Pressure

Lithium niobate is a very established material system, used in various acoustic based sensors. Recent publications in the literature have discussed using $LiNbO_3$ in tire pressure sensors and Pirani vacuum sensors [97,106]. Although much attention has been given to temperature sensitivity measurements, relatively little effort has gone into understanding the effects of $LiNbO_3$ under impact loading conditions [107]. Although this information is valuable, the

purpose of the experiments described here are more suited towards how pressure affects the capacitance of $LiNbO_3$ under typical laboratory ambient pressure.

4.9 Capacitance Measurements

A commercial capacitance bridge, that operates at 1 kHz up to a 15 V input, was used to perform the capacitance measurements. The bridge has an accuracy of 5.5 ppm.

4.10 Pressure Controller and Measurement

A digital pressure calibrator was used to precisely control the gas pressure of the chamber. The calibrator's resolution is 0.001% of the span with a precision of 0.1% of the span. A quartz pressure transducer (Paroscientific Model 745) is connected to both the pressure controller and chamber as a secondary pressure measurement.

4.11 Experimental Setup for Pressure Measurement

Figure 4.12.1 depicts the experimental setup used to measure the capacitance in a pressurized environment. The $LiNbO_3$ (Boston Piezo-Optics, Bellingham, MA) used had dimensions of 15.0 mm × 5.0 mm × 5.0 mm with gold electrodes of dimensions 5 mm × 5 mm × 0.35 μm in the middle of the crystal on two opposing sides in the Y-Z plane. The crystal was mounted in a metal enclosure (Pomona electronics) and sealed inside the chamber. The system was grounded through

the capacitance bridge. The pressure chamber has a volume of 0.089 m^3. Due to the large volume of the chamber and small 18 psi diaphragm pumps, the crystal enclosure was left to stabilize in the pressure chamber overnight before readings were taken. Data were collected using an Excel-based VBA program.

4.12 DATA FROM PRESSURE MEASUREMENT

The capacitance was measured with respect to pressure from sea level up to 7,300 feet. For these readings, the coaxial adapter, which had an average capacitance of 7.6885 pF at barometric pressure (Albuquerque, NM altitude), was subtracted out of the final capacitance measurement.

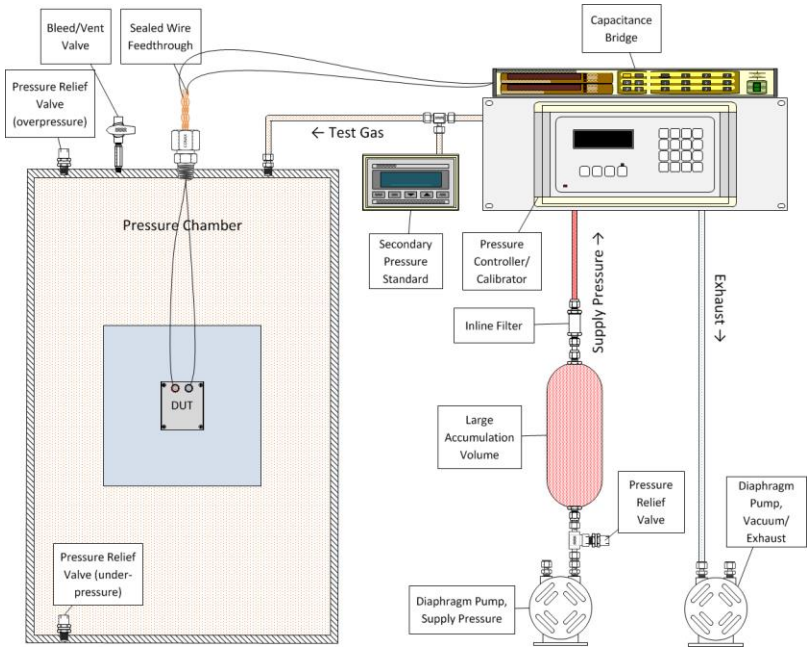

Figure 4.12.1: Experimental setup of pressure coefficient of capacitance measurements.

Figure 4.12.2 shows the capacitance as a function of pressure. The pressure coefficient calculated using a linear fit is 0.041 fF/kPa. The measurement

standard deviation is comparable to the instrument accuracy, which is 5 ppm for a day long measurement. Each data point represents 200 points which are recorded every 1 second.

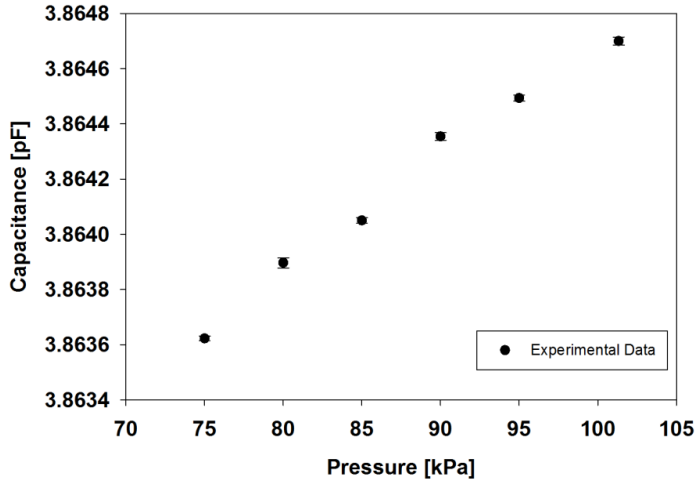

Figure 4.12.2: Capacitance vs. pressure for $LiNbO_3$.

4.13 CORRELATION BETWEEN PRESSURE FORCE AND CHARGE PRODUCED

The crystal is freely suspended inside the Pomona box, there are forces from pressure acting in three general directions: longitudinal, transverse, and shear. Mathematically, this is described as:

$$Q = PAd_{ij} \tag{4.13.1}$$

where Q is the charge, P is the pressure, A is the cross sectional area, and d_{ij}, is the piezoelectric constant as in previous chapters. For this measurement, the d_{ij} values came from this matrix:

$$\begin{bmatrix} 37.99 & -17.17 & -17.05 & 0 & 0 & 6.30 \\ -24.82 & 18.79 & 11.22 & 0 & 0 & 6.31 \\ 0 & 0 & 0 & 78.37 & 6.54 & 0 \end{bmatrix} \frac{pC}{N} \quad (4.13.2)$$

Thus, the total charge can be calculated in the following manner:

$$Q = 25\ \mathrm{mm}^2 * P * ((37.99\ \times 10^{-12} + (-17.17\ \times 10^{-12}) + (-17.05\ \times 10^{-12}) + (6.30\ \times 10^{-12})) \quad (4.13.3)$$

As a result of calculating the charge as a pressure of voltage, the range of the capacitance bridge voltage used was estimated. The 25 mm^2 is the area of the electrode on the top and bottom of the crystal face. Figure 4.13.1 shows the results of the measurements and calculations made using equation 4.13.3.

Because the capacitance is measured using a bridge, the true voltage seen by the capacitor is never known at the time of reading. The bridge voltage setting used was 15 V to minimize noise. Based on the data, the measured voltage used by the bridge ranged between 3-7 V.

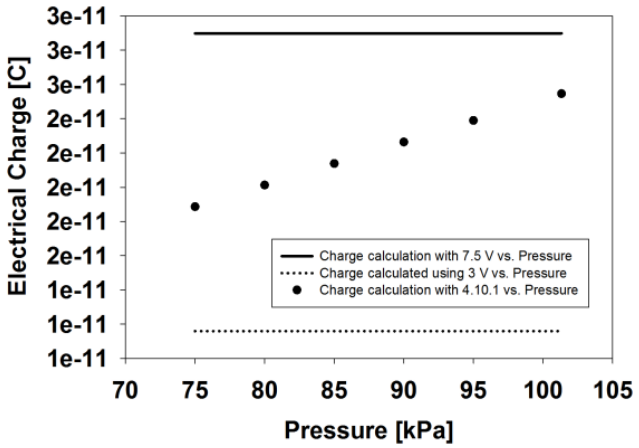

Figure 4.13.1: Electrical charge generated by $LiNbO_3$ vs. pressure. Solid and dotted lines represent charge when applying 7.5 V and 3 V to the crystal, respectively.

4.14 CAPACITANCE RELATIONSHIP TO CHANGE IN VOLTAGE

The experiment performed in this section provided baseline information in regards to how much of an impedance loading effect the HV sensor would have on a pulse waveform. Traditionally, capacitance is measured as a function of frequency for piezoelectric crystals for determining the resonance frequency of the crystal. In the majority of cases, an impedance analyzer, laser interferometry, or a vector network analyzer is employed to perform the measurements. The measurement accuracy for the instruments mentioned above are nominally ± 2% [109]. The measurement accuracy is dictated by factors such as open and short circuit corrections, high quality connections, temperature, and humidity control. These factors ensure good repeatability and reproducibility of the measurements.

4.15 EXPERIMENTAL SETUP OF CAPACITANCE MEASUREMENTS

The same fixture used in the pressure measurement was used. On the capacitance bridge unit, there exists an external DC bias port on the capacitance bridge unit that the multicalibrator was connected to via a BNC cable. Using Fluke METCAL software, the multicalibrator (Fluke Corporation) was programmed to provide voltage to the bridge between 1 V–100 V with the voltage cycling on and off every 5 minutes. This DC voltage was superimposed on top of the AC sine wave from the voltage generator in the bridge as follows:

$$V = V_{dc} + V\sin(2\pi f t) \tag{4.15.1}$$

where the frequency, *f*, is 1 kHz.

4.16 CAPACITANCE-VOLTAGE RESULTS

The capacitance was measured for 1 V, 2.5 V, 5 V, 7.5 V, 10 V, and from 20 V-100 V. Figure 4.16.1 shows the results of the measurements. The nominal capacitance measured was 3.8 pF with a standard deviation between 3.9×10^{-6} pF and 1.1×10^{-4} pF. The conductance was also monitored and ranged between 0.764–0.771 nS which corresponds to a resistance of 1.3 GΩ.

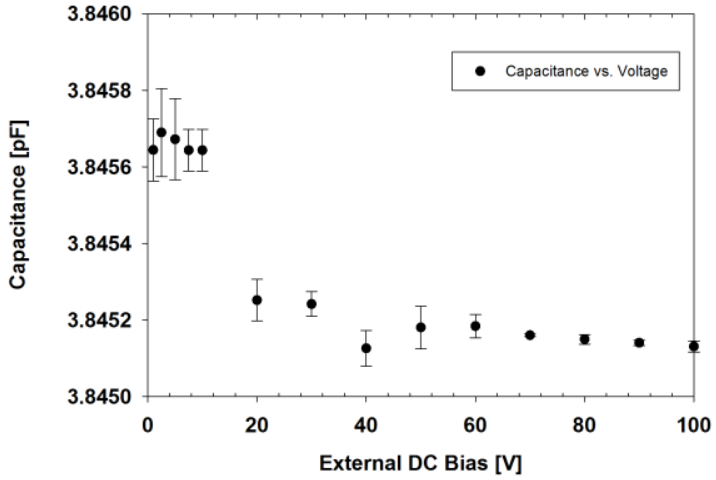

Figure 4.16.1: Capacitance vs. Voltage of Y+36° cut $LiNbO_3$ at 1 kHz.

4.17 **DISCUSSION**

As Figure 4.16.1 shows, the capacitances under 20 V had a higher capacitance by 15 fF, which is likely due to the capacitor not being fully charged to give good readings. Error bars were calculated using the error of the measurement and the error from the bridge. From 20 V onward, the capacitance is nearly constant with just < 0.5 fF variation. Since the sensor's charge appears to be leveling out after 80 V, capacitance values for even higher DC voltages will remain constant. For AC and pulsed applications, more care would need to be given for the experimental set up to verify that the capacitor has fully charged and that the voltages do not interfere with the impedance reading. Furthermore, the bridge would no longer be a useable instrument and the measurement error would suffer greatly if the capacitor was not fully charged.

4.18 CONCLUSION

This chapter discussed the environmental and electrical characteristics of $LiNbO_3$ may affect performance of the HV sensor discussed in this dissertation. The temperature coefficients for two crystal cuts were measured and revealed that simple linear theory is insufficient for determining the crystal's TCD, and that nonlinear coefficients of the material constants must be used to fully predict the TCD. Capacitance vs. pressure measurements were undertaken for pressures between sea level and 7,300 ft. The data shows that capacitance increases proportionally with pressure, but the actual capacitance range only varies by 1 fF, making this crystal very sensitive to pressure changes. Using a force-charge model, the amount of charge generated by the crystal was compared to capacitance measurements for two applied voltages, and they agreed relative to one another. Finally, capacitance vs. voltage measurements were carried out for voltages up to 100 V. Data showed that the capacitance starts to level out for applied voltages greater than 80 V DC. It was found that both temperature and pressure effects don't significantly impact the measurements discussed in chapters 2 and 3.

5 EFFECTS OF LITHIUM NIOBATE MATERIAL CONSTANTS UNDER STRESS OF A DC BIAS FIELD

1. INTRODUCTION

Lithium niobate has established itself as the material of choice in many sensor, actuator, transducer, and resonator applications. Thus, such wide usage of this piezoelectric material requires a detailed characterization of the dielectric permittivity, piezoelectric coefficients, and elastic coefficients. Much literature has devoted time to establishing temperature coefficients and nonlinear coefficients of these material constants [94,96,103,110]. Furthermore, the crystal symmetry dictates that there exists 8 electrostrictive, three 3rd order dielectric, 13 third order piezoelectric, and 14 third order elastic constants of $LiNbO_3$. These measurements involve measuring the change in capacitance as a function of stress change using a load cell, and measuring variation of resonant frequencies as a function of static electric field, and variation in velocity as a function of static electric field and static stress. Due to the large amount of constants and measurements required to obtain the nonlinear constants, a mathematical fitting solution based on few measured constants is used to determine the remaining constants [96,111,112].

When an electric field is not present, two conventional methods exist for determining linear material constants: resonance/antiresonance frequency measurements of the crystal, and acoustic velocity measurements of the crystal [113].

5.1 ANTIRESONANCE/RESONANCE MEASUREMENT METHODS

One of the drivers behind for performing antiresonance/resonance measurements stems from the 176-1987 IEEE standard on piezoelectricity, which highlights the relationship between frequency and material constants by modeling a piezoelectric material as a Butterworth-Van-Dyke equivalent circuit [66].

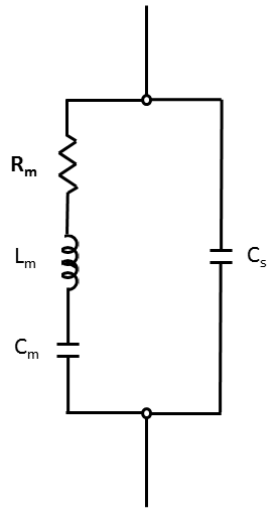

Figure 5.1.1: Generalized Butterworth-Van-Dyke equivalent circuit model used to describe piezoelectric material.

The material constants can be extracted from frequency measurements of assorted crystallographic orientations of $LiNbO_3$, provided that the material has no loss, through the electromechanical coupling coefficient [109]. Measurements today use an LCR (Inductance-Capacitance-Resistance) meter which measures the voltage and the current across a device in a 4-wire terminal configuration. The voltage to current ratio leads to the magnitude of the impedance and the equivalent circuit setting (i.e. L_{series}-R_{series}, or an inductor and resistor in series) is

used internally by the meter to break out the individual components from the impedance magnitude. When the frequencies are measured as a function of voltage, an external voltage bias fixture can be used to safely apply voltage to the DUT without interrupting the voltage sensing arms of the LCR meter.

5.2 THEORETICAL CALCULATIONS OF ACOUSTIC VELOCITIES

As mentioned in chapter 3, the eigenvalue solutions to the Christoffel equation lead to relationships between acoustic velocities in the three principal axis directions and the crystal's material constants. Again, the Christoffel equation with piezoelectric stiffening is described as follows:

$$k^2\left(l_{iK}\left\{C_{KL}^{E}+\frac{\left[e_{Kj}l_j\right]\left[l_i e_{il}\right]}{l_i\varepsilon_{ij}^{S}l_j}\right\}l_{Lj}\right)v_j=\rho\omega^2 v_i \qquad (5.2.1)$$

To solve for v_x, v_y, *and* v_z several matrix operations must be carried out which are discussed in more detail in the Appendix A2. After performing the matrix multiplication and dividing through by ρ, the left hand side of 5.3.1 yields:

X-Propagation

$$\begin{pmatrix} c_{11} & 0 & 0 \\ 0 & c_{66}+\frac{e_{22}^2}{\epsilon_x} & c_{14}+\frac{e_{15}e_{22}}{\epsilon_x} \\ 0 & c_{14}+\frac{e_{15}e_{22}}{\epsilon_x} & c_{44}+\frac{e_{15}^2}{\epsilon_x} \end{pmatrix} \tag{5.2.2}$$

Y-Propagation

$$\begin{pmatrix} c_{66} & 0 & 0 \\ 0 & c_{11}+\frac{e_{22}^2}{\epsilon_y} & -c_{14}-\frac{e_{15}e_{22}}{\epsilon_y} \\ 0 & -c_{14}-\frac{e_{15}e_{22}}{\epsilon_y} & c_{44}+\frac{e_{15}^2}{\epsilon_y} \end{pmatrix} \tag{5.2.3}$$

Z-Propagation

$$\begin{pmatrix} c_{44} & 0 & 0 \\ 0 & c_{44} & 0 \\ 0 & 0 & c_{33}+\frac{e_{33}^2}{\epsilon_z} \end{pmatrix} \tag{5.2.4}$$

Using Mathematica to solve for the eigenvalues, the velocities for each cut are as follows:

X-propagation, X-polarization

$$\rho V_{x,x}^2 = c_{11} \tag{5.2.5}$$

X-propagation, Y-polarization

$$\rho V_{x,y}^2 = \frac{e_{15}^2+e_{22}^2+c_{44}\epsilon_x+c_{66}\epsilon_x-\sqrt{(-e_{15}^2-e_{22}^2-c_{44}\epsilon_x-c_{66}\epsilon_x)^2-4(c_{66}e_{15}^2\epsilon_x-2c_{14}e_{15}e_{22}\epsilon_x+c_{44}e_{22}^2\epsilon_x-c_{14}^2\epsilon_x^2+c_{44}c_{66}\epsilon_x^2)}}{2\epsilon_x} \tag{5.2.6}$$

X-propagation, Z-polarization

$$\rho V_{x,z}^2 = \frac{e_{15}^2 + e_{22}^2 + c_{44}\epsilon_x + c_{66}\epsilon_x + \sqrt{(-e_{15}^2 - e_{22}^2 - c_{44}\epsilon_x - c_{66}\epsilon_x)^2 - 4(c_{66}e_{15}^2\epsilon_x - 2c_{14}e_{15}e_{22}\epsilon_x + c_{44}e_{22}^2\epsilon_x - c_{14}^2\epsilon_x^2 + c_{44}c_{66}\epsilon_x^2)}}{2\epsilon_x} \quad (5.2.7)$$

Y-propagation, X-polarization

$$\rho V_{y,x}^2 = C_{66} \quad (5.2.8)$$

Y-propagation, Y-polarization

$$\rho V_{y,y}^2 = \frac{e_{15}^2 + e_{22}^2 + c_{11}\epsilon_y + c_{44}\epsilon_y - \sqrt{\left(e_{15}^2 + e_{22}^2 + (c_{11} + c_{44})\epsilon_y\right)^2 - 4\epsilon_y\left(-2c_{14}e_{15}e_{22} + c_{44}e_{22}^2 - c_{14}^2\epsilon_y + c_{11}\left(e_{15}^2 + c_{44}\epsilon_y\right)\right)}}{2\rho\epsilon_y} \quad (5.2.9)$$

Y-propagation, Z-polarization

$$\rho V_{y,z}^2 = \frac{e_{15}^2 + e_{22}^2 + c_{11}\epsilon_y + c_{44}\epsilon_y + \sqrt{\left(e_{15}^2 + e_{22}^2 + (c_{11} + c_{44})\epsilon_y\right)^2 - 4\epsilon_y\left(-2c_{14}e_{15}e_{22} + c_{44}e_{22}^2 - c_{14}^2\epsilon_y + c_{11}\left(e_{15}^2 + c_{44}\epsilon_y\right)\right)}}{2\rho\epsilon_y} \quad (5.2.10)$$

Z-propagation, X-polarization (Y-Polarization)

$$\rho V_{z,x(y)}^2 = C_{44} \quad (5.2.11)$$

Z-propagation, Z-polarization

$$\rho V_{z,z}^2 = c_{33} + \frac{e_{33}^2}{\epsilon_z} \quad (5.2.12)$$

5.3 EXPERIMENTAL SETUP FOR SHEAR AND LONGITUDINAL WAVE MEASUREMENTS

For all longitudinal wave measurements the setup is identical to that found in chapter 3. Shear wave measurements required a shear wave transducer (Olympus NDT) that has a nominal element size of 6 mm at a frequency of 10

MHz. The connector type is a right angle microdot which required that the system be placed in a vice so that an adequate signal can be detected on the oscilloscope and the TIC. Figure 5.3.1 shows the modified setup.

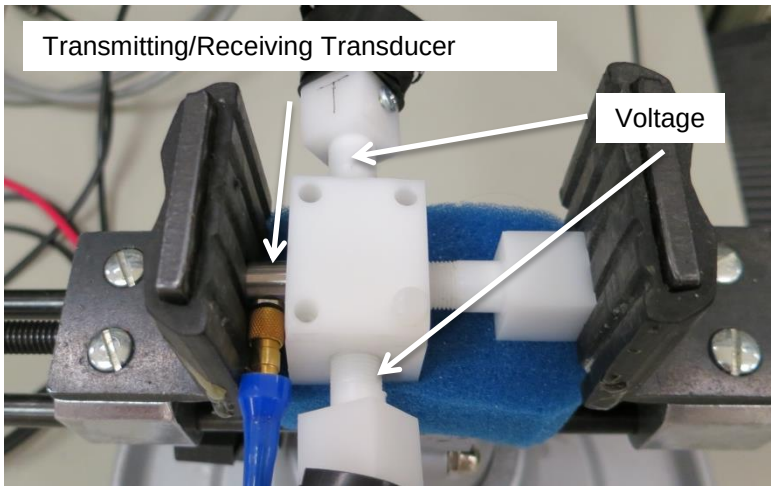

Figure 5.3.1: Shear wave measurement setup. The fixture was clamped in a vise with enough force to have adequate coupling between the shear wave transducer face and crystal. The voltage was applied in the same manner as the longitudinal wave measurements.

The increase in standard deviation for the shear wave measurements in comparison to measurements using a longitudinal wave setup is a result of the shear wave being more dispersive and, therefore, more difficult to achieve good SNR to detect a clean signal with the TIC. As a result, the pulser unit was run with a higher gain (> 30 dB) and increased energy in the voltage excitation signal. The measurements were well within the calculated uncertainty budget found in Appendix A3.

5.4 EXPERIMENTAL DATA FOR MATERIAL CONSTANT AND VELOCITY MEASUREMENTS

5.4.1 ELASTIC CONSTANT C11 MEASUREMENTS

The elastic constant C_{11} is the elastic constant directly related to the X-propagating X-polarized wave velocity shown in equation 5.2.5. The measurement was performed in the experimental set up discussed in chapter 2 and 3 using a transmitting and receiving transducer. Figure 5.4.1 shows the results.

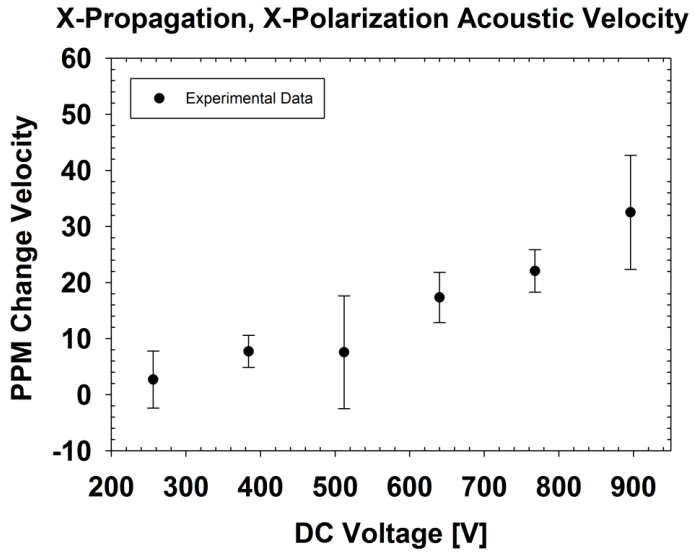

Figure 5.4.1: Plot of PPM change in velocity vs. applied DC voltage of an X-propagating, X-polarized (or Y-polarized) wave. This wave is directly related to C_{11}.

The velocity changed from 2.7-32.5 ppm with a measurement standard deviation that varied from 2.9–45.5 ppm. Using a density of ρ = 4650 g/m^3, the nominal C_{11} value was measured to be 203 GPa. The average change in C_{11} ranged from 1.1–37.8 MPa with a measurement standard deviation of 0.8–4.1 MPa.

5.4.2 ELASTIC CONSTANT C_{66} MEASUREMENTS

The elastic constant C_{66} is the elastic constant directly related to the Y-propagating X-polarized wave velocity shown in equation 5.2.8. The measurement was performed in the experimental set up discussed in Section 5.3 using a single shear wave transducer. Figure 5.4.2: shows the results.

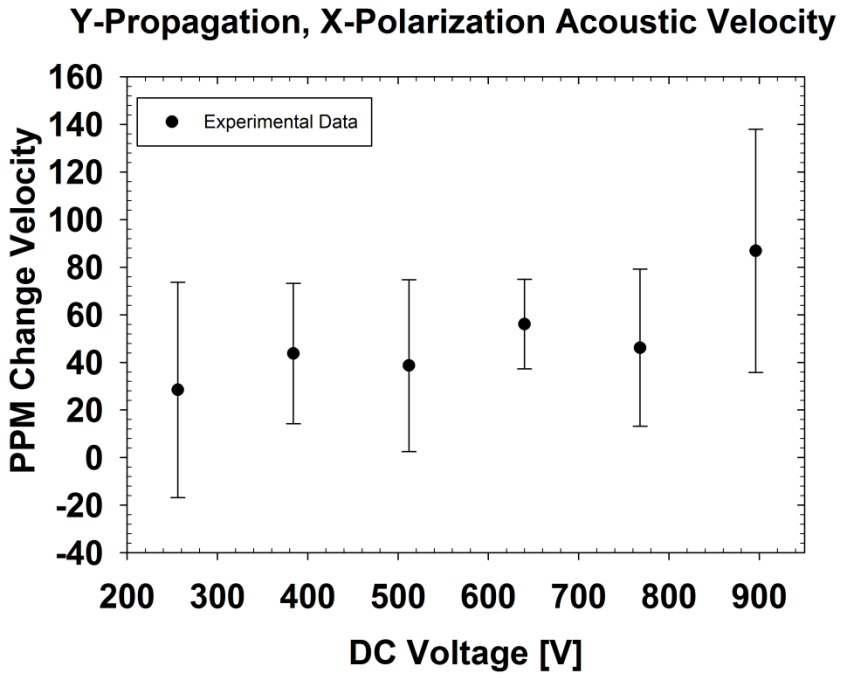

Figure 5.4.2: Plot of PPM change in velocity vs. applied DC voltage of an Y-propagating, X-polarized. This wave is directly related to C_{66}.

Since there is no piezoelectric activity with this propagation and polarization configuration, it is expected that there will not be a strong correlation between the velocity and applied voltage, which is demonstrated by the results. The velocity varied between 28.4 and 86.9 ppm with a measurement standard deviation that varied from 18.9 to 51.1 ppm over the voltage range of 256 V to 896 V. Using a density of ρ = 4650 g/m^3, the nominal C_{66} value was calculated to be 72.9 GPa.

The average change in c_{66} ranged from 4.5-12.7 MPa with a measurement standard deviation of 2.6–13.2 MPa.

5.4.3 ELASTIC CONSTANT C_{44} MEASUREMENTS

From equation 5.2.11, C_{44} is a degenerate material constant that is directly related to a Z-propagating, Y-polarized acoustic wave and a Z-propagating, X-polarized acoustic wave acoustic wave. The measurement was performed in the experimental set up discussed in section 5.3 using a single shear wave transducer. Figure 5.4.3 shows the results.

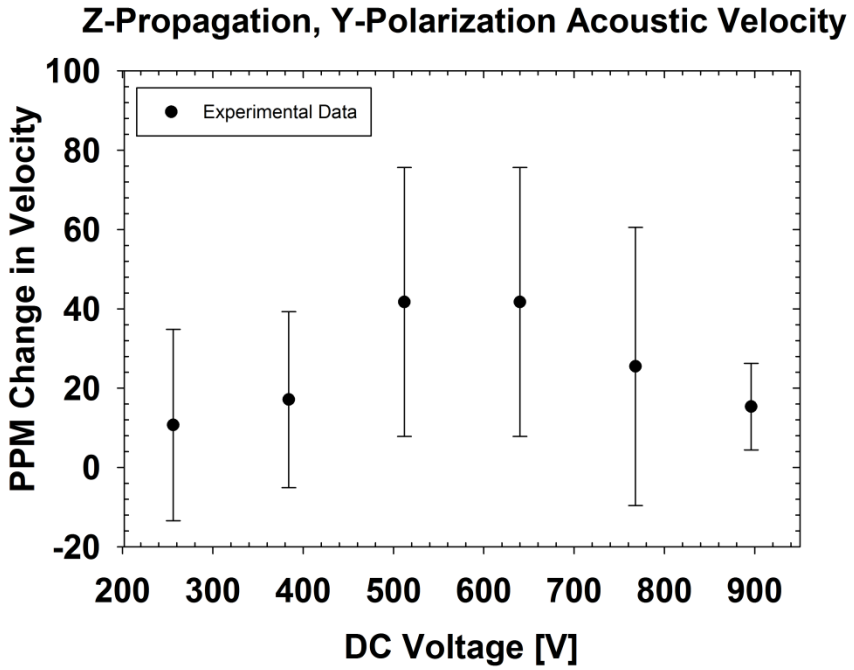

Figure 5.4.3: Plot of PPM change in velocity vs. applied DC voltage of a Z-propagating, X-polarized (or Y-polarized) wave. This wave is directly related to C_{44}.

The velocity changed from 10.7-41.7 ppm with a measurement standard deviation that varied from 10.1–33.9 ppm. Using a density of ρ = 4650 g/m^3, the

nominal c_{44} value was measured to be 63.2 GPa. The average change in C_{44} ranged 1.9-5.2 MPa with a measurement standard deviation of 1.4-4.5 MPa.

5.4.4 X-PROPAGATING Z-POLARIZED VELOCITY, V_{13} MEASUREMENTS

Equation 5.2.7 mathematically describes a Z-polarized, X-propagating velocity that is piezoelectrically active. This activity is identified by the presence of piezoelectric constants in the equation. Figure 5.4.4 shows the results of these measurements.

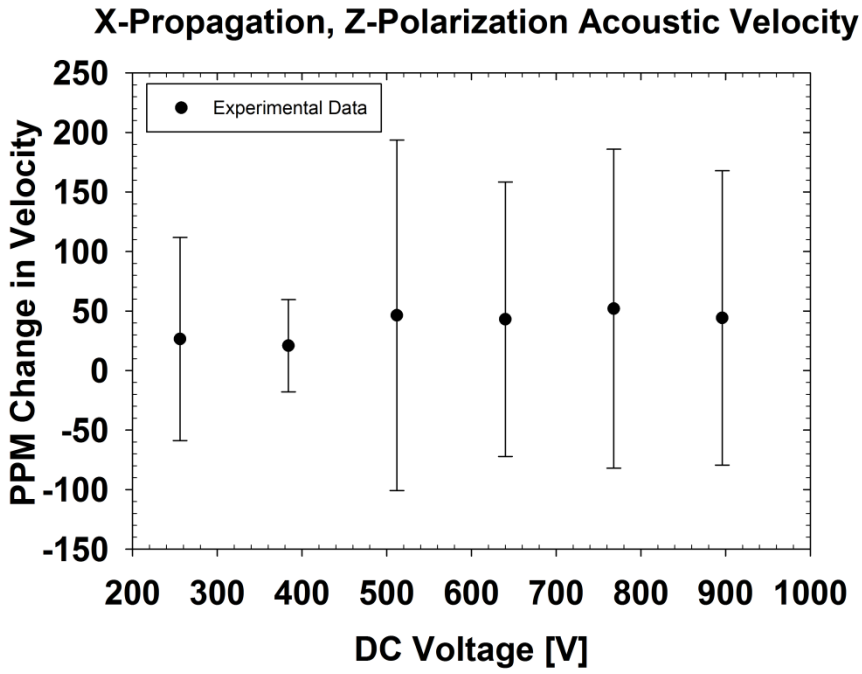

Figure 5.4.4: Plot of PPM change in velocity vs. applied DC voltage of voltage of an X-propagating, Z-polarized. This shear wave is piezoelectrically active.

The velocity changed from 20.8–51.9 ppm with a measurement standard deviation that varied from 38.8 to 133.96 ppm, a result of shear waves possessing more attenuation and dispersion than longitudinal waves [114].

5.4.5 Y-POLARIZED, Y-PROPAGATING VELOCITY, V_{22} MEASUREMENTS

Equation 5.2.9 mathematically describes a Y-polarized, Y-propagating acoustic velocity that is piezoelectrically active. This activity is identified by the presence of piezoelectric constants in the equation. Figure 5.4.5 shows the results.

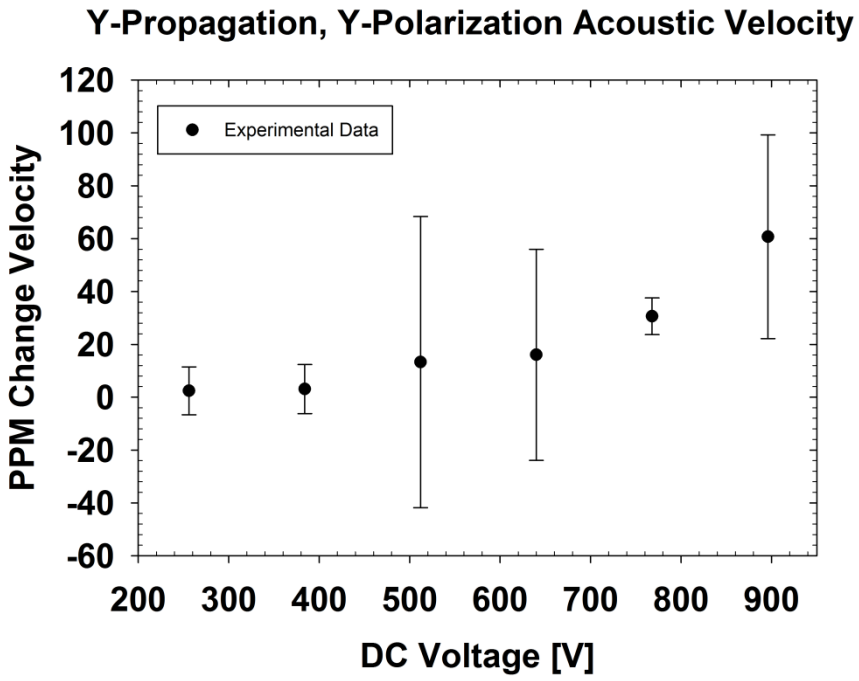

Figure 5.4.5: Plot of PPM change in velocity vs. applied DC voltage of an Y-propagating, Y-polarized. This longitudinal wave is piezoelectrically active.

The velocity changed from 20.8–51.9 ppm with a measurement standard deviation that varied from 38.8-147 ppm. Although influenced by electric fields, the wave associated with this velocity is a longitudinal wave, which has an error that is less than what is found in the V_{13} velocity.

5.5 PIEZOELECTRIC CONSTANTS d_{15} AND d_{22} CALCULATIONS

The piezoelectric coefficients are only present in velocities where a piezoelectric stiffening term is present. For example, the piezoelectric stiffening term is the second term in the z-propagating, z-polarized velocity, which is described in equation 5.2.12.

In the context of this dissertation, the variation in constants d_{15} and d_{22} were not directly measured, but were determined from other velocity measurements. Mathematically, the two constants can be calculated from e_{15} and e_{22}:

$$e_{15} = \sqrt{\varepsilon_o \varepsilon_{rxx} \left(\frac{\rho^2 V_{y,y}^2 V_{y,z}^2 - \rho^2 V_{x,y}^2 V_{x,z}^2}{c_{11} - c_{66}} - c_{44} \right)} \tag{5.5.1}$$

$$e_{22} = \sqrt{\varepsilon_o \varepsilon_{rxx} \left(\rho V_{y,y}^2 + \rho V_{y,z}^2 - c_{44} - c_{11} - \frac{e_{15}^2}{\varepsilon_{rxx}} \right)} \tag{5.5.2}$$

$$[d] = ([C]^{-1}[e]^T)^T \tag{5.5.3}$$

Figure 5.5.1 shows calculated values of e_{15} and e_{22}. The lack of variation in the nominal value over a function of voltage is consistent with what is found in varying the electromechanical coupling constant as a function of voltage in PZT [115].

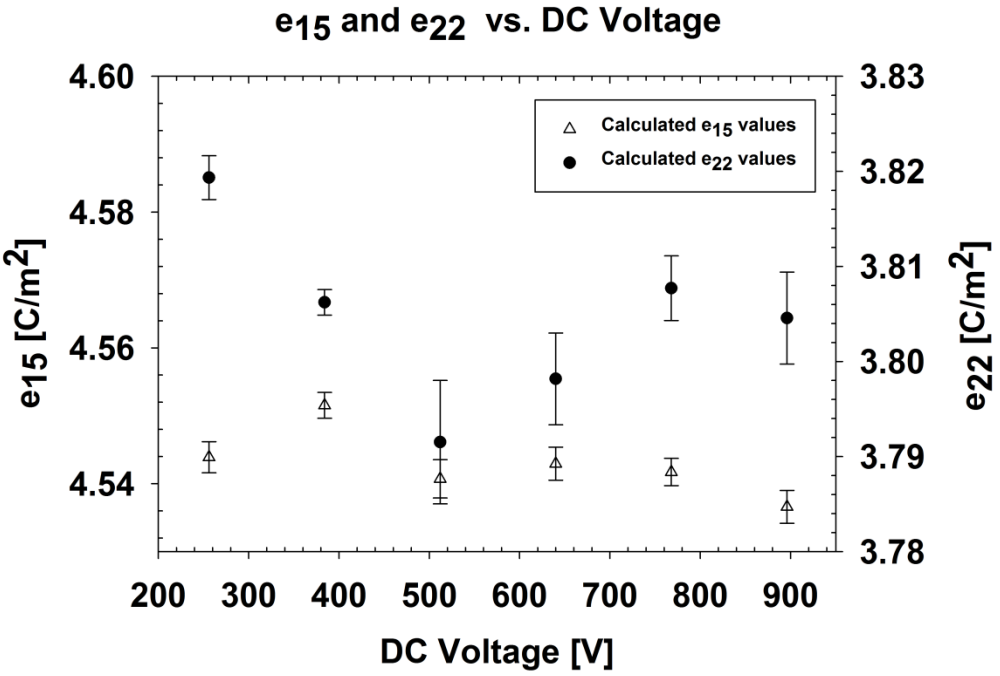

Figure 5.5.1: Plot of calculated values of e_{15} (red circles) and e_{22} (Black squares) as a function of voltage. The error bars come from a Kline-Mcclintock uncertainty analysis of the calculation.

In lieu of this, measurements from Andruschak *et al*. were utilized to obtain estimates for this velocity and the constants C_{14}, C_{31}, and C_{33} since these constants are needed to fully define [*C*] [116]. Constants d_{15} and d_{22} were determined from calculations using equations 5.5.1, 5.5.2, and 5.5.3. Since the HV sensor results discussed in chapters 2 and 3 are based upon d_{15} and d_{22} they are the only reported constants of interest. Since the conversion to d_{15} and d_{22} requires the full matrix multiplication, a Monte Carlo simulation was performed.

5.6 MONTE CARLO SIMULATIONS OF $LiNbO_3$ MATERIAL CONSTANTS

In order to understand how acoustic velocity in $LiNbO_3$ is influenced by changing material constants under the influence of voltage, a Monte Carlo simulation was

carried out for each of the velocity propagation/direction combinations mentioned in 5.2 using Matlab. The simulation allowed for each material constant to change independently, keeping the rest of the constants fixed. This was done to show how sensitive each material constant is to a velocity with a given propagation and polarization.

5.6.1 ELASTIC CONSTANT C_{11} CALCULATIONS

Based on the measurements described in 5.4, the change in C_{11} was 5.4–65.2 ppm with a measurement standard deviation of 10-33.3 ppm. With respect to acoustic velocity, the change corresponds to 2.7-32.5 ppm with a measurement standard deviation that varied from 5.1–10.2 ppm over the voltage range of 256–896 V.

The experimental data were related to the Monte Carlo simulation by using the experimental change in C_{11} as an input and calculating changes in the acoustic velocity. The remaining constants are held fixed. This calculated velocity change is then related to the experimental velocity change.

Table 5.6.1 summarizes the experimental velocity changes to the calculated velocity change for this elastic constant. Since the velocity is calculated in the same manner for the measured data and the Monte Carlo simulation, their agreement is expected. The constant C_{11} constant also has impact on several other acoustic velocities.

Table 5.6.1: Comparison between change in measured C_{11} and velocity as a function of voltage to the calculated velocity change using Monte Carlo simulation.

Voltage (V)	Measured C_{11} Change (ppm)	Average Measured Velocity Change (ppm)	Standard Deviation Measured Velocity Change (ppm)	Calculated Velocity Change (± ppm)
256	5.4	2.7	5.1	2.5
384	15.5	7.7	2.9	7.4
512	15.1	7.6	10.1	7.7
640	34.7	17.3	4.5	17.3
768	44.2	22.1	3.9	22.1
896	65.2	32.5	10.2	32.2

5.6.2 THE ELASTIC CONSTANT C_{66} CALCULATIONS

Based on the measurements described in 5.4.2, the change in C_{66} was 57.9–173.8 ppm with a measurement standard deviation of 10-48 ppm. With respect to acoustic velocity, the change corresponds to 28.4-86.9 ppm with a measurement standard deviation that varied from 18.9–51.1 ppm over the voltage range of 256 V to 896 V.

The experimental data was related to the Monte Carlo simulation by using the experimental change in C_{66} as an input and calculating changes in the acoustic velocity. The remaining constants are held constant. This calculated velocity change is then related to the experimental velocity change. Table 5.6.2 summarizes the experimental velocity changes to the calculated velocity change for this elastic constant. Since the velocity is calculated in the same manner for the measured data and the Monte Carlo simulation, their agreement is expected.

Table 5.6.2: Comparison between the change in measured C_{66} and velocity as a function of voltage to the calculated velocity change using Monte Carlo simulation.

Voltage (V)	Measured C_{66} Change (ppm)	Average Measured Velocity Change (ppm)	Standard Deviation Measured Velocity Change (ppm)	Calculated Velocity Change (± ppm)
256	62.1	28.4	45.2	31.0
384	57.9	43.7	29.5	29
512	77.3	38.6	36.1	38.6
640	112.1	56.1	18.9	55.9
768	92.3	46.2	33.0	46.2
896	173.8	86.9	51.1	86.9

5.6.3 THE ELASTIC CONSTANT C_{44} CALCULATIONS

Based on the measurements described in 5.4, the change in C_{44} was 5.4–186.3 ppm with a measurement standard deviation of 10-48 ppm. With respect to acoustic velocity, the change corresponds to 2.7-93.8 ppm with a measurement standard deviation that varied from 2–45.5 ppm over the voltage range of 256 V to 896 V. Table 5.6.3 summarizes the experimental velocity changes to the calculated velocity change for this elastic constant.

Table 5.6.3: Comparison between change in measured C_{44} and velocity as a function of voltage to the calculated velocity change using Monte Carlo simulation.

Voltage (V)	Measured C_{44} Change (ppm)	Average Measured Velocity Change (ppm)	Standard Deviation Measured Velocity Change (ppm)	Calculated Velocity Change (± ppm)
256	21.4	10.7	24.1	1.1
384	42	17.1	22.2	2.1
512	82.5	41.7	33.9	4.1
640	77.7	41.7	33.9	3.9
768	52.5	25.5	35.1	2.6
896	30.7	15.3	10.9	1.5

5.7 PIEZOELECTRIC CONSTANT SIMULATIONS

In order to perform Monte Carlo simulations for d_{15} and d_{22}, data from the aforementioned elastic constant measurements and e_{15} and e_{22} calculations were utilized to carry out the simulation. Material constants that were not measured or calculated, namely C_{31}, C_{33}, C_{14}, e_{31} and e_{33}, were set to fixed values found in the literature.

5.8 PIEZOELECTRIC CONSTANT D_{15} AND D_{22} CALCULATIONS

Equation 5.5.3 was used to calculate d_{15} and d_{22}. The expanded version of equation 5.5.3 is as follows:

$$\begin{pmatrix} 0 & d_{22} & d_{31} \\ 0 & -d_{22} & d_{31} \\ 0 & 0 & d_{33} \\ 0 & 0 & 0 \\ d_{15} & 0 & 0 \\ d_{22} & 0 & 0 \end{pmatrix} = \left(\begin{pmatrix} c_{11} & c_{12} & c_{13} & c_{14} & 0 & 0 \\ c_{12} & c_{11} & c_{13} & -c_{14} & 0 & 0 \\ c_{13} & c_{13} & c_{33} & 0 & 0 & 0 \\ c_{14} & -c_{14} & 0 & c_{44} & 0 & 0 \\ 0 & 0 & 0 & 0 & c_{44} & 2c_{14} \\ 0 & 0 & 0 & 0 & 2c_{14} & c_{66} \end{pmatrix}^{-1} \begin{pmatrix} 0 & e_{22} & e_{31} \\ 0 & -e_{22} & e_{31} \\ 0 & 0 & e_{33} \\ 0 & 0 & 0 \\ e_{15} & 0 & 0 \\ e_{22} & 0 & 0 \end{pmatrix}^{T} \right)^{T} \quad (5.8.1)$$

For calculating the [d] matrix the respect to the appropriate rotation, the Euler angles (0°, 0°, 0°) were used. By allowing for variation in the material constants, a standard deviation and average for d_{15} and d_{22} were calculated. Kline-McClintock uncertainty analysis was performed on both e_{15} and e_{22} based on the data [117]:

$$\pm e_{15} = \sqrt{\begin{array}{l}\left(\frac{\partial e_{15}}{\partial C_{11}}\sigma_{C_{11}}\right)^2 + \left(\frac{\partial e_{15}}{\partial C_{44}}\sigma_{C_{44}}\right)^2 + \left(\frac{\partial e_{15}}{\partial C_{66}}\sigma_{C_{66}}\right)^2 + \left(\frac{\partial e_{15}}{\partial \varepsilon_{xx}}\sigma_{\varepsilon_{xx}}\right)^2 + \\ \left(\frac{\partial e_{15}}{\partial V_{X,Y}}\sigma_{V_{X,Y}}\right)^2 + \left(\frac{\partial e_{15}}{\partial V_{Y,Y}}\sigma_{V_{Y,Y}}\right)^2 + \left(\frac{\partial e_{15}}{\partial V_{Y,Z}}\sigma_{V_{Y,Z}}\right)^2 + \left(\frac{\partial e_{15}}{\partial V_{X,Z}}\sigma_{V_{X,Z}}\right)^2\end{array}} \quad (5.8.2)$$

$$\pm e_{22} = \sqrt{\begin{array}{l}\left(\frac{\partial e_{15}}{\partial C_{11}}\sigma_{C_{11}}\right)^2 + \left(\frac{\partial e_{15}}{\partial C_{44}}\sigma_{C_{44}}\right)^2 + \left(\frac{\partial e_{15}}{\partial C_{66}}\sigma_{C_{66}}\right)^2 + \left(\frac{\partial e_{15}}{\partial \varepsilon_{xx}}\sigma_{\varepsilon_{xx}}\right)^2 + \\ \left(\frac{\partial e_{15}}{\partial V_{X,Y}}\sigma_{V_{X,Y}}\right)^2 + \left(\frac{\partial e_{15}}{\partial V_{Y,Y}}\sigma_{V_{Y,Y}}\right)^2 + \left(\frac{\partial e_{15}}{\partial V_{Y,Z}}\sigma_{V_{Y,Z}}\right)^2 + \left(\frac{\partial e_{15}}{\partial V_{X,Z}}\sigma_{V_{X,Z}}\right)^2\end{array}} \quad (5.8.3)$$

The full versions of 5.8.2 and 5.8.3 can be found in the Appendix A3. The standard deviation was calculated, on average, to range from 3.5 to 17.1% for e_{15} and 0.08-0.11% for e_{22} over the voltage range of 256–896 V. Using the newly calculated e_{15} and e_{22} values and associated errors, equation 5.8.1 was solved to calculate the *d* matrix based on measured values. In comparing these calculations to the d_{ij} terms used in Section 3.7 of chapter 3, it was found that the values calculated from the Monte Carlo are different. The average and standard deviation for d_{11} and d_{61} for the 0° X-cut was calculated to be 6.24×10^{-11} m/V ± 0.016×10^{-11} m/V and -0.45×10^{-11} m/V ± 0.016×10^{-11} m/V, respectively. For the Y+ 36° cut, d_{11} and d_{43} was calculated to be 4.2391×10^{-11} m/V ± 0.02×10^{-11} m/V and 1.69×10^{-11} m/V ± 0.004×10^{-11} m/V, respectively.

5.9 DISCUSSION AND CONCLUSIONS

The average and standard deviation for d_{11} and d_{61} for the 0° X-cut was calculated to be 6.24×10^{-11} m/V ± 0.016×10^{-11} m/V and 1.78×10^{-11} m/V ± $0.11\times10^{-}$

^{11} m/V, respectively. For the Y+ 36° cut, d_{11} and d_{43} was calculated to be 7.73×10^{-11} m/V ± 0.12×10^{-11} m/V and 3.49×10^{-11} m/V ± 0.08×10^{-11} m/V, respectively.

Table 5.9.1 shows a summary of the original piezoelectric values used in chapter 3 with what was calculated using measured velocity and constants from this chapter.

Table 5.9.1: Comparison between constants used to model measured values in chapter 3 vs. the calculated values after Monte Carlo simulations.

Strain charge constants	**D_{11} (X-cut 0°)**	**D_{61} (X-cut 0°)**	**D_{11} (Y+36°)**	**D_{43} (Y+36°)**
Values used in chapter 3 (Kovacs)	2.04×10^{-11} m/V	6.75×10^{-11} m/V	3.81x10^{11} m/V	7.86×10^{-11} m/V
Monte Carlo simulation results	6.24×10^{-11} m/V	1.78×10^{-11} m/V	7.73×10^{-11} m/V	3.49×10^{-11} m/V

When calculating equation 5.8.1 in full, it is important to note that e_{31} and C_{14} are parameters that are not measured in this dissertation but are important in calculating d_{61} and d_{43}. From Andrushchak *et al.,* a tabulation of material constants from measurements and previous literature shows that e_{31} variation in values from 0.2 to 0.37 C/m^2 while C_{14} varied from 7.45-9 GPa [116]. Measurements of e_{31} showed a variation range of 37%-48% in the measured values and C_{14} varied by 1%. Based on these variation ranges, it is possible that both constants would have a great influence on the d_{61} and d_{43} value. When these variations are plugged into the Monte Carlo simulation, with the appropriate Euler angles used for Y+36° cut, d_{43} remains 3.49×10^{-11} m/V ±0.08×10^{-11} m/V and d_{11} is 7.71×10^{-11} m/V ± 0.12×10^{-11} m/V. When the C_{14} and e_{31} variations are plugged into the Monte Carlo simulation, with the appropriate Euler angles used for 0° X-cut, d_{61} remains to 1.77×10^{-11} m/V ± 0.11×10^{-11} m/V. and d_{11} is 6.24×10^{-11} m/V ± 0.016×10^{-11} m/V.

From the simulation results, it was found that variation in e_{31} and C_{14} did not have a significant influence on determining the values of d_{43} and d_{61}. Thus, measuring e_{31} and C_{14} would not elucidate the problem of more accurately determining the piezoelectric strain charge constants, but potentially further complicate it, at least under DC electric field conditions. To fully characterize d_{ij}, further experiments using AC and pulsed voltages are required to fully understand the voltage sensor response. Even though the d_{ij} coefficients were difficult determine using this method described in this dissertation, a more accurate means of determining the elastic constants was achieved using the TIC without the use of fitting routines or additional signal processing techniques [92,116]. Full characterization of the d_{ij} terms with respect to frequency is required in order to use this system to work as a metrology-grade replacement for the NIST-N1 pulsed voltage divider. It would require that more accurate measurement techniques for the piezoelectric constants be sought out that quantify the frequency dependence of the constants.

The data acquisition and analysis in this chapter were performed to determine how material constants and acoustic velocities are influenced by voltage. Both longitudinal and shear wave velocities were measured on several $LiNbO_3$ crystal cuts to determine the stress-charge form piezoelectric coefficients, e_{15} and e_{22}, as a function of voltage. From here, the calculated e_{15} and e_{22} constants, along with measured elastic constants and measured velocities, were inputted into a Monte Carlo simulation to determine the rotated strain-charge form piezoelectric constants. d_{11}, d_{61}, d_{43}, function of voltage for 0° X-cut and Y+36°-cut $LiNbO_3$. It

was found that a large variation in the piezoelectric constants exists when comparing rotated literature constants and calculating constants from direct measurement. In particular, direct measurements show that d_{11} can differ by 100-200%, d_{61} by 279%, and d_{43} by 125% in comparison to previously rotated measured values. In order for this system to work as a metrology-grade replacement for the NIST-N1 divider, it would require that more accurate measurement techniques for the piezoelectric constants be sought out that quantify the voltage dependence on the constants.

6 CONCLUSION AND FUTURE WORK

This dissertation provides insight into using $LiNbO_3$'s piezoelectric properties to design a direct measurement bulk acoustic wave HV sensor for DC, AC, and pulsed voltage applications. In addition, experiments were carried out to investigate how the crystal response varies as a function of crystal cut as well as shear and longitudinal acoustic wave propagation. Within this comparison, an uncertainty budget of the measurement system was carried out and compared. Furthermore, the piezoelectric and anisotropic nature of $LiNbO_3$ led to measurements of the sensor when under constant pressure and temperature variation. Finally, a systematic study of material constants and velocities of several crystals under the influence of a DC electric field were studied to assess the feasibility of predicting the HV sensor response using material constants as input parameters. Below is a summary of observations and remarks on improvements for future work.

Applying such high voltages to bulk $LiNbO_3$ has never been reported in the literature using the configuration described in this dissertation. To demonstrate the feasibility of this sensor, a Y+36° cut crystal response was found to behave linearly DC field conditions when a DC voltage was applied transversely to the interrogating acoustic wave. This work showed that both single pass and multipass sensing of the acoustic wave is possible using $LiNbO_3$ in such a configuration.

Successful demonstration led to determining the sensor response when voltage was applied in-line with the interrogating acoustic wave. To perform these

measurements an X°-cut crystal and a Y+36° cut crystal were compared. The comparison also provided an understanding of the influence of crystal cut on the sensor response. Results showed that the voltage-induced shift in the acoustic wave propagation time scaled quadratically with voltage for DC and AC voltages applied to X-cut crystals. For the Y+36° crystal, the voltage-induced shift scales linearly with DC voltages and quadratically with AC voltages. For the Y+36° cut, the voltage-induced shift from applying DC voltages ranged from 10–54 ps and 35–778 ps for AC voltages at 640 V over the frequency range of 100 Hz–100 kHz. For 5 μs voltage pulses, the 0° X-cut crystal sensed a voltage induced shift of 0.250–2 ns and the Y+36°-cut crystal sensed a time shift of 0.115–1.6 ns. Thus, to within experimental error, the responses were equivalent. When applying 5 μs voltage pulses to both crystals, the voltage-induced shift scaled linearly with voltage. Using the same conditions as the Y+36° cut, the 0° X-cut crystal sensed a shift of 10–273 ps for DC voltages and 189–813 ps for AC voltage application. For 5 μs voltage pulses, the 0° X-cut crystal sensed a voltage induced shift of 0.250–2 ns and the Y+36°-cut crystal sensed a time shift of 0.115–1.6 ns. This suggests a frequency sensitive response to voltage where the influence of the crystal cut was not a significant contributor under DC, AC, or pulsed voltage conditions. The data presented may help in aiding future modelling efforts in this area. The measured DC data was compared to a 1-D impedance matrix model where the predicted incremental length changed as a function of voltage. This model provided qualitative insight on the complexity of electromechanical coupling between different material systems but simplified the

anisotropic nature of $LiNbO_3$. The best-case uncertainty budget of the sensor (within a 95% confidence interval) was calculated 0.0033% using an Y+36°-cut crystal and 0.0032% using an X-cut crystal for all the voltage conditions used in this experiment.

However, the previously measured piezoelectric stress-charge constants, d_{ij}, that were used to estimate the measured response was found to be inadequate, providing errors of 32% and 60% errors to the response of the X-cut and Y+36°-cut crystal sensor, respectively under DC electric field conditions. Because of this large error in d_{ij}, a systematic study of measuring the material constants as a function of voltage was explored that was not previous performed in the literature. As expected, it was found that the elastic constants C_{11}, C_{44}, and C_{66} had ppm level variation under the influence of an electric field, which is to be expected since pure elastic waves are mechanical in nature. It was found that piezeoelectricity active longitudinal wave velocities, in particular V_{22}, had smaller errors versus measurements performed on piezeoelectricity active shear wave velocities, such as V_{13}. Using these velocities and material constants, a Kline-McClintock uncertainty analysis was performed on e_{15} and e_{22} which were used to help determine d_{ij} values. Simulations performed discovered that d_{11} was underestimated by using Kovac's material constants and d_{61} (used in X-cut crystal sensor response) and d_{43} (used in Y+36°-cut crystal sensor response) were underestimated by a factor of three [92]. Using measured values (not under an electric field bias) of e_{31} and C_{14}, yielded no improvements in estimating d_{61}

and d_{43}. With these conclusions in mind, the following recommendations for improvements can be made:

1. One method of improving the sensitivity of the voltage sensor is to use $LiNbO_3$ as a resonator. In this configuration, the resonator would have a higher quality factor, which will increase the measurement sensitivity. As a result of this increased sensitivity, it may be possible to measure lower voltages using a resonator configuration.
2. Although only pulses of 5 μs were measured and the crystal was able to respond, the original NIST-N1 resistive divider was designed to measure 1 μs pulses with ns rise times. With this in mind, resorting back to optical techniques using the Pockels effect or Kerr effect, with additional signal processing of the output, and a low noise laser source might potentially improve the measurement uncertainty of the system [118].
3. An additional study of how the material constants change both as a function of temperature and voltage might further elucidate any errors that were observed in this dissertation. Furthermore, determining the amount of stress applied by the transducers in both the longitudinal wave and shear wave setups would also help in understanding how much stress is actually applied to the crystal. Knowing this information can help better predict the sensor response. Furthermore, a computational model with linear and nonlinear material constants with their associated temperature coefficients may provide deeper insight into the physics occurring under AC and pulsed voltage application.

A. APPENDIX

A.1 CHRISTOFFEL EQUATION SOLUTIONS

X-Cut

Christoffel's Equation is:

$$k^2\left(l_{iK}\left\{C_{KL}^{E}+\frac{[e_{Kj}l_j][l_ie_{il}]}{l_i\varepsilon_{ij}^{S}l_j}\right\}l_{Lj}\right)v_j=\rho\omega^2v_i$$

First, we will solve the denominator in the inner bracket:

$$(1\quad 0\quad 0)\begin{pmatrix}\epsilon_x & 0 & 0\\ 0 & \epsilon_y & 0\\ 0 & 0 & \epsilon_z\end{pmatrix}\begin{pmatrix}1\\0\\0\end{pmatrix}$$

$$l_i\varepsilon_{ij}^{S}l_j=\epsilon_x$$

The numerator in the inner bracket is:

$$e_{Kj}l_j=\begin{pmatrix}0 & 0 & 0 & 0 & e_{15} & e_{22}\\ e_{22} & -e_{22} & 0 & e_{15} & 0 & 0\\ e_{31} & e_{31} & e_{33} & 0 & 0 & 0\end{pmatrix}\begin{pmatrix}1\\0\\0\end{pmatrix}$$

$$l_ie_{il}=(1\quad 0\quad 0)\begin{pmatrix}0 & 0 & 0 & 0 & e_{15} & e_{22}\\ e_{22} & -e_{22} & 0 & e_{15} & 0 & 0\\ e_{31} & e_{31} & e_{33} & 0 & 0 & 0\end{pmatrix}$$

Multiplication of these two portions becomes:

$$[e_{Kj}l_j][l_ie_{il}]=\begin{pmatrix}0 & 0 & 0 & 0 & 0 & 0\\ 0 & 0 & 0 & 0 & 0 & 0\\ 0 & 0 & 0 & 0 & 0 & 0\\ 0 & 0 & 0 & 0 & 0 & 0\\ 0 & 0 & 0 & 0 & e_{15}^2 & e_{15}e_{22}\\ 0 & 0 & 0 & 0 & 2e_{15}e_{22} & e_{22}^2\end{pmatrix}$$

Completion of the inner bracket sum and dividing by ϵ_x becomes:

$$\left\{C_{KL}^{E}+\frac{\left[e_{Kj}l_j\right]\left[l_i e_{il}\right]}{l_i \varepsilon_{ij}^{S} l_j}\right\}=\begin{pmatrix} c_{11} & c_{12} & c_{13} & c_{14} & 0 & 0 \\ c_{12} & c_{11} & c_{13} & -c_{14} & 0 & 0 \\ c_{13} & c_{13} & c_{33} & 0 & 0 & 0 \\ c_{14} & -c_{14} & 0 & c_{44} & 0 & 0 \\ 0 & 0 & 0 & 0 & c_{44}+\frac{e_{15}^2}{\epsilon_x} & c_{14}+\frac{e_{15}e_{22}}{\epsilon_x} \\ 0 & 0 & 0 & 0 & c_{14}+\frac{e_{15}e_{22}}{\epsilon_x} & c_{66}+\frac{e_{22}^2}{\epsilon_x} \end{pmatrix}$$

Multiply bracket by l_{iK} and l_{Lj}

$$=\begin{pmatrix} 1 & 0 & 0 & 0 & 0 & 0 \\ 0 & 0 & 0 & 0 & 0 & 1 \\ 0 & 0 & 0 & 0 & 1 & 0 \end{pmatrix}\begin{pmatrix} c_{11} & c_{12} & c_{13} & c_{14} & 0 & 0 \\ c_{12} & c_{11} & c_{13} & -c_{14} & 0 & 0 \\ c_{13} & c_{13} & c_{33} & 0 & 0 & 0 \\ c_{14} & -c_{14} & 0 & c_{44} & 0 & 0 \\ 0 & 0 & 0 & 0 & c_{44}+\frac{e_{15}^2}{\epsilon_x} & c_{14}+\frac{e_{15}e_{22}}{\epsilon_x} \\ 0 & 0 & 0 & 0 & c_{14}+\frac{e_{15}e_{22}}{\epsilon_x} & c_{66}+\frac{e_{22}^2}{\epsilon_x} \end{pmatrix}\begin{pmatrix} 1 & 0 & 0 \\ 0 & 0 & 0 \\ 0 & 0 & 0 \\ 0 & 0 & 0 \\ 0 & 0 & 1 \\ 0 & 1 & 0 \end{pmatrix}$$

Christoffel's equation with 3 x 3 solution

$$k^2\begin{pmatrix} c_{11} & 0 & 0 \\ 0 & c_{66}+\frac{e_{22}^2}{\epsilon_x} & c_{14}+\frac{e_{15}e_{22}}{\epsilon_x} \\ 0 & c_{14}+\frac{e_{15}e_{22}}{\epsilon_x} & c_{44}+\frac{e_{15}^2}{\epsilon_x} \end{pmatrix}v_j=\rho\omega^2 v_i$$

Solving for eigenvalues yields:

X-propagation, X-polarization

$$\rho V_{x,x}^2=c_{11}$$

X-propagation, Y-polarization

$$\rho V_{x,y}^2$$

$$= \frac{e_{15}^2 + e_{22}^2 + c_{44}\epsilon_x + c_{66}\epsilon_x - \sqrt{(-e_{15}^2 - e_{22}^2 - c_{44}\epsilon_x - c_{66}\epsilon_x)^2 - 4(c_{66}e_{15}^2\epsilon_x - 2c_{14}e_{15}e_{22}\epsilon_x + c_{44}e_{22}^2\epsilon_x - c_{14}^2\epsilon_x^2 + c_{44}c_{66}\epsilon_x^2)}}{2\epsilon_x}$$

X–propagation, Z-polarization

$$\rho V_{x,z}^2$$

$$= \frac{e_{15}^2 + e_{22}^2 + c_{44}\epsilon_x + c_{66}\epsilon_x + \sqrt{(-e_{15}^2 - e_{22}^2 - c_{44}\epsilon_x - c_{66}\epsilon_x)^2 - 4(c_{66}e_{15}^2\epsilon_x - 2c_{14}e_{15}e_{22}\epsilon_x + c_{44}e_{22}^2\epsilon_x - c_{14}^2\epsilon_x^2 + c_{44}c_{66}\epsilon_x^2)}}{2\epsilon_x}$$

Y-Cut

First, we will solve the denominator in the inner bracket:

$$(0 \quad 1 \quad 0)\begin{pmatrix}\epsilon_x & 0 & 0\\ 0 & \epsilon_y & 0\\ 0 & 0 & \epsilon_z\end{pmatrix}\begin{pmatrix}0\\1\\0\end{pmatrix}$$

$$l_i \varepsilon_{ij}^S l_j = \epsilon_y$$

The numerator in the inner bracket is:

$$e_{Kj}l_j = \begin{pmatrix}0 & 0 & 0 & 0 & e_{15} & e_{22}\\ e_{22} & -e_{22} & 0 & e_{15} & 0 & 0\\ e_{31} & e_{31} & e_{33} & 0 & 0 & 0\end{pmatrix}\begin{pmatrix}0\\1\\0\end{pmatrix}$$

$$l_i e_{il} = (0 \quad 1 \quad 0)\begin{pmatrix}0 & 0 & 0 & 0 & e_{15} & e_{22}\\ e_{22} & -e_{22} & 0 & e_{15} & 0 & 0\\ e_{31} & e_{31} & e_{33} & 0 & 0 & 0\end{pmatrix}$$

Multiplication of these two portions becomes:

$$\left[e_{Kj}l_j\right]\left[l_i e_{il}\right] = \begin{pmatrix}e_{22}^2 & -e_{22}^2 & 0 & e_{15}e_{22} & 0 & 0\\ -e_{22}^2 & e_{22}^2 & 0 & -e_{15}e_{22} & 0 & 0\\ 0 & 0 & 0 & 0 & 0 & 0\\ e_{15}e_{22} & -e_{15}e_{22} & 0 & e_{15}^2 & 0 & 0\\ 0 & 0 & 0 & 0 & 0 & 0\\ 0 & 0 & 0 & 0 & 0 & 0\end{pmatrix}$$

Completion of the inner bracket sum and dividing by ϵ_y becomes:

$$C_{KL}^{E}+\frac{\left[e_{Kj}l_j\right]\left[l_ie_{il}\right]}{l_i\varepsilon_{ij}^{S}l_j}=\begin{pmatrix} c_{11}+\frac{e_{22}^2}{\epsilon_y} & c_{12}-\frac{e_{22}^2}{\epsilon_y} & c_{13} & c_{14}+\frac{e_{15}e_{22}}{\epsilon_y} & 0 & 0 \\ c_{12}-\frac{e_{22}^2}{\epsilon_y} & c_{11}+\frac{e_{22}^2}{\epsilon_y} & c_{13} & -c_{14}-\frac{e_{15}e_{22}}{\epsilon_y} & 0 & 0 \\ c_{13} & c_{13} & c_{33} & 0 & 0 & 0 \\ c_{14}+\frac{e_{15}e_{22}}{\epsilon_y} & -c_{14}-\frac{e_{15}e_{22}}{\epsilon_y} & 0 & c_{44}+\frac{e_{15}^2}{\epsilon_y} & 0 & 0 \\ 0 & 0 & 0 & 0 & c_{44} & c_{14} \\ 0 & 0 & 0 & 0 & c_{14} & c_{66} \end{pmatrix}$$

Multiply bracket by l_{iK} and l_{Lj}

$$\begin{pmatrix} 0 & 0 & 0 & 0 & 0 & 1 \\ 0 & 1 & 0 & 0 & 0 & 0 \\ 0 & 0 & 0 & 1 & 0 & 0 \end{pmatrix}\begin{pmatrix} c_{11}+\frac{e_{22}^2}{\epsilon_y} & c_{12}-\frac{e_{22}^2}{\epsilon_y} & c_{13} & c_{14}+\frac{e_{15}e_{22}}{\epsilon_y} & 0 & 0 \\ c_{12}-\frac{e_{22}^2}{\epsilon_y} & c_{11}+\frac{e_{22}^2}{\epsilon_y} & c_{13} & -c_{14}-\frac{e_{15}e_{22}}{\epsilon_y} & 0 & 0 \\ c_{13} & c_{13} & c_{33} & 0 & 0 & 0 \\ c_{14}+\frac{e_{15}e_{22}}{\epsilon_y} & -c_{14}-\frac{e_{15}e_{22}}{\epsilon_y} & 0 & c_{44}+\frac{e_{15}^2}{\epsilon_y} & 0 & 0 \\ 0 & 0 & 0 & 0 & c_{44} & c_{14} \\ 0 & 0 & 0 & 0 & c_{14} & c_{66} \end{pmatrix}\begin{pmatrix} 0 & 0 & 0 \\ 0 & 1 & 0 \\ 0 & 0 & 0 \\ 0 & 0 & 1 \\ 0 & 0 & 0 \\ 1 & 0 & 0 \end{pmatrix}$$

Christoffel's equation with 3 x 3 solution

$$k^2\begin{pmatrix} c_{66} & 0 & 0 \\ 0 & c_{11}+\frac{e_{22}^2}{\epsilon_y} & -c_{14}-\frac{e_{15}e_{22}}{\epsilon_y} \\ 0 & -c_{14}-\frac{e_{15}e_{22}}{\epsilon_y} & c_{44}+\frac{e_{15}^2}{\epsilon_y} \end{pmatrix}v_j=\rho\omega^2v_i$$

Y-propagation, X-polarization

$$\rho V_{y,x}^2=C_{66}$$

Y-propagation, Y-polarization

$$\rho V_{y,y}^2$$

$$= \frac{e_{15}^2 + e_{22}^2 + c_{11}\epsilon_y + c_{44}\epsilon_y - \sqrt{\left(e_{15}^2 + e_{22}^2 + (c_{11} + c_{44})\epsilon_y\right)^2 - 4\epsilon_y\left(-2c_{14}e_{15}e_{22} + c_{44}e_{22}^2 - c_{14}^2\epsilon_y + c_{11}\left(e_{15}^2 + c_{44}\epsilon_y\right)\right)}}{2\rho\epsilon_y}$$

Y-propagation, Z-polarization

$$\rho V_{y,z}^2$$

$$= \frac{e_{15}^2 + e_{22}^2 + c_{11}\epsilon_y + c_{44}\epsilon_y + \sqrt{\left(e_{15}^2 + e_{22}^2 + (c_{11} + c_{44})\epsilon_y\right)^2 - 4\epsilon_y\left(-2c_{14}e_{15}e_{22} + c_{44}e_{22}^2 - c_{14}^2\epsilon_y + c_{11}\left(e_{15}^2 + c_{44}\epsilon_y\right)\right)}}{2\rho\epsilon_y}$$

Z-Cut

First, we will solve the denominator in the inner bracket :

$$(0 \quad 0 \quad 1).\begin{pmatrix} \epsilon_x & 0 & 0 \\ 0 & \epsilon_y & 0 \\ 0 & 0 & \epsilon_z \end{pmatrix}.\begin{pmatrix} 0 \\ 0 \\ 1 \end{pmatrix}$$

$$l_i \varepsilon_{ij}^S l_j = \epsilon_z$$

The numerator in the inner bracket is:

$$e_{Kj}l_j = \begin{pmatrix} 0 & 0 & 0 & 0 & e_{15} & e_{22} \\ e_{22} & -e_{22} & 0 & e_{15} & 0 & 0 \\ e_{31} & e_{31} & e_{33} & 0 & 0 & 0 \end{pmatrix}\begin{pmatrix} 0 \\ 0 \\ 1 \end{pmatrix}$$

$$l_i e_{il} = (0 \quad 0 \quad 1)\begin{pmatrix} 0 & 0 & 0 & 0 & e_{15} & e_{22} \\ e_{22} & -e_{22} & 0 & e_{15} & 0 & 0 \\ e_{31} & e_{31} & e_{33} & 0 & 0 & 0 \end{pmatrix}$$

Multiplication of these two portions becomes:

$$[e_{Kj}l_j][l_ie_{il}] = \begin{pmatrix} e_{31}^2 & e_{31}^2 & e_{31}e_{33} & 0 & 0 & 0 \\ e_{31}^2 & e_{31}^2 & e_{31}e_{33} & 0 & 0 & 0 \\ e_{31}e_{33} & e_{31}e_{33} & e_{33}^2 & 0 & 0 & 0 \\ 0 & 0 & 0 & 0 & 0 & 0 \\ 0 & 0 & 0 & 0 & 0 & 0 \\ 0 & 0 & 0 & 0 & 0 & 0 \end{pmatrix}$$

Z-propagation, X-polarization and Y-Polarization

$$\rho V_{z,x(y)}^2 = C_{44}$$

Z-propagation, Z-polarization

$$\rho V_{z,z}^2 = c_{33} + \frac{e_{33}^2}{\epsilon_z}$$

Completion of the inner bracket sum and dividing by ϵ_z becomes:

$$\begin{pmatrix} c_{11} + \frac{e_{31}^2}{\epsilon_z} & c_{12} + \frac{e_{31}^2}{\epsilon_z} & c_{13} + \frac{e_{31}e_{33}}{\epsilon_z} & c_{14} & 0 & 0 \\ c_{12} + \frac{e_{31}^2}{\epsilon_z} & c_{11} + \frac{e_{31}^2}{\epsilon_z} & c_{13} + \frac{e_{31}e_{33}}{\epsilon_z} & -c_{14} & 0 & 0 \\ c_{13} + \frac{e_{31}e_{33}}{\epsilon_z} & c_{13} + \frac{e_{31}e_{33}}{\epsilon_z} & c_{33} + \frac{e_{33}^2}{\epsilon_z} & 0 & 0 & 0 \\ c_{14} & -c_{14} & 0 & c_{44} & 0 & 0 \\ 0 & 0 & 0 & 0 & c_{44} & c_{14} \\ 0 & 0 & 0 & 0 & c_{14} & c_{66} \end{pmatrix}$$

Multiply bracket by l_{iK} and l_{Lj}

$$\begin{pmatrix} 0 & 0 & 0 & 0 & 1 & 0 \\ 0 & 0 & 0 & 1 & 0 & 0 \\ 0 & 0 & 1 & 0 & 0 & 0 \end{pmatrix} \begin{pmatrix} c_{11} + \frac{e_{31}^2}{\epsilon_z} & c_{12} + \frac{e_{31}^2}{\epsilon_z} & c_{13} + \frac{e_{31}e_{33}}{\epsilon_z} & c_{14} & 0 & 0 \\ c_{12} + \frac{e_{31}^2}{\epsilon_z} & c_{11} + \frac{e_{31}^2}{\epsilon_z} & c_{13} + \frac{e_{31}e_{33}}{\epsilon_z} & -c_{14} & 0 & 0 \\ c_{13} + \frac{e_{31}e_{33}}{\epsilon_z} & c_{13} + \frac{e_{31}e_{33}}{\epsilon_z} & c_{33} + \frac{e_{33}^2}{\epsilon_z} & 0 & 0 & 0 \\ c_{14} & -c_{14} & 0 & c_{44} & 0 & 0 \\ 0 & 0 & 0 & 0 & c_{44} & c_{14} \\ 0 & 0 & 0 & 0 & c_{14} & c_{66} \end{pmatrix} \begin{pmatrix} 0 & 0 & 0 \\ 0 & 0 & 0 \\ 0 & 0 & 1 \\ 0 & 1 & 0 \\ 1 & 0 & 0 \\ 0 & 0 & 0 \end{pmatrix}$$

Christoffel's equation with 3 x 3 solution:

$$k^2\begin{pmatrix} c_{44} & 0 & 0 \\ 0 & c_{44} & 0 \\ 0 & 0 & c_{33}+\dfrac{e_{33}^2}{\epsilon_z} \end{pmatrix} v_j = \rho\omega^2 v_i$$

A.2 KLINE-MCCLINTOCK UNCERTAINTY CALCULATIONS FOR E_{15} AND E_{22}

e_{15}

$$e_{15} = \sqrt{(-C_{44}+\frac{-\rho^2V_{12}^2V_{13}^2+\rho^2V_{22}^2V_{23}^2}{C_{11}-C_{66}})\epsilon_o\epsilon_{\mathrm{xx}}}$$

$$\pm e_{15} = \sqrt{\begin{matrix}\left(\frac{\partial e_{15}}{\partial C_{11}}\sigma_{C_{11}}\right)^2+\left(\frac{\partial e_{15}}{\partial C_{44}}\sigma_{C_{44}}\right)^2+\left(\frac{\partial e_{15}}{\partial C_{66}}\sigma_{C_{66}}\right)^2+\left(\frac{\partial e_{15}}{\partial \varepsilon_{xx}}\sigma_{\varepsilon_{xx}}\right)^2+ \\ \left(\frac{\partial e_{15}}{\partial V_{X,Y}}\sigma_{V_{X,Y}}\right)^2+\left(\frac{\partial e_{15}}{\partial V_{Y,Y}}\sigma_{V_{Y,Y}}\right)+\left(\frac{\partial e_{15}}{\partial V_{Y,Z}}\sigma_{V_{Y,Z}}\right)^2+\left(\frac{\partial e_{15}}{\partial V_{X,Z}}\sigma_{V_{X,Z}}\right)^2\end{matrix}}$$

$$\frac{de_{15}}{dc_{44}} = -\frac{\epsilon_o\epsilon_{\mathrm{xx}}}{2\sqrt{(-C_{44}+\frac{-\rho^2V_{12}^2V_{13}^2+\rho^2V_{22}^2V_{23}^2}{C_{11}-C_{66}})\epsilon_o\epsilon_{\mathrm{xx}}}}$$

$$\frac{de_{15}}{dc_{66}} = \frac{(-\rho^2V_{12}^2V_{13}^2+\rho^2V_{22}^2V_{23}^2)\epsilon_o\epsilon_{\mathrm{xx}}}{2(C_{11}-C_{66})^2\sqrt{(-C_{44}+\frac{-\rho^2V_{12}^2V_{13}^2+\rho^2V_{22}^2V_{23}^2}{C_{11}-C_{66}})\epsilon_o\epsilon_{\mathrm{xx}}}}$$

$$\frac{de_{15}}{dc_{11}} = -\frac{(-\rho^2 V_{12}^2 V_{13}^2 + \rho^2 V_{22}^2 V_{23}^2)\epsilon_o \epsilon_{xx}}{2(C_{11}-C_{66})^2 \sqrt{(-C_{44} + \frac{-\rho^2 V_{12}^2 V_{13}^2 + \rho^2 V_{22}^2 V_{23}^2}{C_{11}-C_{66}})\epsilon_o \epsilon_{xx}}}$$

$$\frac{de_{15}}{dV_{12}} = -\frac{\rho^2 V_{12} V_{13}^2 \epsilon_o \epsilon_{xx}}{(C_{11}-C_{66}) \sqrt{(-C_{44} + \frac{-\rho^2 V_{12}^2 V_{13}^2 + \rho^2 V_{22}^2 V_{23}^2}{C_{11}-C_{66}})\epsilon_o \epsilon_{xx}}}$$

$$\frac{de_{15}}{dV_{13}} = -\frac{\rho^2 V_{12}^2 V_{13} \epsilon_o \epsilon_{xx}}{(C_{11}-C_{66}) \sqrt{(-C_{44} + \frac{-\rho^2 V_{12}^2 V_{13}^2 + \rho^2 V_{22}^2 V_{23}^2}{C_{11}-C_{66}})\epsilon_o \epsilon_{xx}}}$$

$$\frac{de_{15}}{dV_{22}} = \frac{\rho^2 V_{22} V_{23}^2 \epsilon_o \epsilon_{xx}}{(C_{11}-C_{66}) \sqrt{(-C_{44} + \frac{-\rho^2 V_{12}^2 V_{13}^2 + \rho^2 V_{22}^2 V_{23}^2}{C_{11}-C_{66}})\epsilon_o \epsilon_{xx}}}$$

$$\frac{de_{15}}{dV_{23}} = \frac{\rho^2 V_{22}^2 V_{23} \epsilon_o \epsilon_{xx}}{(C_{11}-C_{66}) \sqrt{(-C_{44} + \frac{-\rho^2 V_{12}^2 V_{13}^2 + \rho^2 V_{22}^2 V_{23}^2}{C_{11}-C_{66}})\epsilon_o \epsilon_{xx}}}$$

$$\frac{de_{15}}{d\varepsilon_{xx}} = \frac{(-C_{44} + \frac{-\rho^2 V_{12}^2 V_{13}^2 + \rho^2 V_{22}^2 V_{23}^2}{C_{11}-C_{66}})\epsilon_o}{2\sqrt{(-C_{44} + \frac{-\rho^2 V_{12}^2 V_{13}^2 + \rho^2 V_{22}^2 V_{23}^2}{C_{11}-C_{66}})\epsilon_o \epsilon_{xx}}}$$

e_{22}

$$\mathrm{e22} = \sqrt{\epsilon_o(-C_{11} - C_{44} + \rho(V_{22}^2 + V_{23}^2) - \frac{e_{15}^2}{\epsilon_o \epsilon_{xx}})\epsilon_{xx}}$$

$$\pm e_{22} = \sqrt{\left(\frac{\partial e_{15}}{\partial C_{11}}\sigma_{C_{11}}\right)^2 + \left(\frac{\partial e_{15}}{\partial C_{44}}\sigma_{C_{44}}\right)^2 + \left(\frac{\partial e_{15}}{\partial C_{66}}\sigma_{C_{66}}\right)^2 + \left(\frac{\partial e_{15}}{\partial \varepsilon_{xx}}\sigma_{\varepsilon_{xx}}\right)^2 + \left(\frac{\partial e_{15}}{\partial V_{X,Y}}\sigma_{V_{X,Y}}\right)^2 + \left(\frac{\partial e_{15}}{\partial V_{Y,Y}}\sigma_{V_{Y,Y}}\right)^2 + \left(\frac{\partial e_{15}}{\partial V_{Y,Z}}\sigma_{V_{Y,Z}}\right)^2 + \left(\frac{\partial e_{15}}{\partial V_{X,Z}}\sigma_{V_{X,Z}}\right)^2}$$

$$\frac{de_{22}}{dc_{44}} = -\frac{\epsilon_o \epsilon_{xx}}{2\sqrt{\epsilon_o(-C_{11} - C_{44} + \rho(V_{22}^2 + V_{23}^2) - \frac{e_{15}^2}{\epsilon_o \epsilon_{xx}})\epsilon_{xx}}}$$

$$\frac{de_{22}}{dc_{11}} = -\frac{\epsilon_o \epsilon_{xx}}{2\sqrt{\epsilon_o(-C_{11} - C_{44} + \rho(V_{22}^2 + V_{23}^2) - \frac{e_{15}^2}{\epsilon_o \epsilon_{xx}})\epsilon_{xx}}}$$

$$\frac{de_{22}}{dV_{23}} = \frac{\rho V_{23} \epsilon_o \epsilon_{xx}}{\sqrt{\epsilon_o(-C_{11} - C_{44} + \rho(V_{22}^2 + V_{23}^2) - \frac{e_{15}^2}{\epsilon_o \epsilon_{xx}})\epsilon_{xx}}}$$

$$\frac{de_{22}}{dV_{22}} = \frac{\rho V_{22} \epsilon_o \epsilon_{xx}}{\sqrt{\epsilon_o(-C_{11} - C_{44} + \rho(V_{22}^2 + V_{23}^2) - \frac{e_{15}^2}{\epsilon_o \epsilon_{xx}})\epsilon_{xx}}}$$

$$\frac{de_{22}}{de_{15}} = -\frac{e_{15}}{\sqrt{\epsilon_o(-C_{11} - C_{44} + \rho(V_{22}^2 + V_{23}^2) - \frac{e_{15}^2}{\epsilon_o \epsilon_{xx}})\epsilon_{xx}}}$$

A.3 UNCERTAINTY BUDGETS FOR DC, AC, AND PULSED VOLTAGES

Estimated uncertainty for voltage measurements based on 0° X-cut crystal for DC and AC measurements.

Description	Magnitude	Distribution	Degree of Freedom	Divisor	Standard Uncertainty	Uncertainty Type	Contribution
Crystal Response From DC/AC Voltage	1.73E-06	Normal	4	1	1.73E-06	A	0.01%
10 MHz External Timebase	3.33E-13	Expanded (k=3)	30	3	1.11E-13	B	0.00%
Temperature of Crystal	1.57E-04	Normal	30	1	1.57E-04	B	97.99%
Crystal Dimensions	3.80E-05	Rectangular	30	1.732	2.19E-05	B	1.91%
Time Interval Counter	8.02E-06	Rectangular	30	1.732	4.63E-06	B	0.09%
		Notes:					
Combined A & B Standard Uncertainty	1.59E-04	**DC and AC Voltage Uncertainty Measurements**					
Effective Degrees of Freedom	31	**The time interval counter used was a Stanford Research Systems SRS 620**					
Coverage Factor (k)	2.04	**The multicalibrator used was a Fluke 5700**					
Expanded Combined Uncertainty	**3.24E-04**						

Estimated uncertainty for voltage measurements based on Y+36° cut crystal for DC and AC measurements.

Description	Magnitude	Distribution	Degree of Freedom	Divisor	Standard Uncertainty		Uncertainty Type	Contribution
Crystal Response From DC/AC Voltage	1.73E-06	Normal	4	1	1.73E-06	2.99E-12	A	0.00%
10 MHz External Timebase	3.33E-13	Expanded (k=3)	30	3	1.11E-13	1.23E-26	B	0.00%
Temperature of Crystal	1.50E-04	Normal	30	1	1.50E-04	2.24E-08	B	99.95%
								0.00%
Crystal Dimensions	3.80E-05	Rectangular	30	1.732	2.19E-05	4.81E-10	B	0.05%
Time Interval Counter	8.02E-06	Rectangular	30	1.732	4.63E-06	2.14E-11	B	0.00%
		Notes:						
Combined A & B Standard Uncertainty	1.51E-04	**DC and AC Voltage Uncertainty Measurements**						
Effective Degrees of Freedom	32	**The time interval counter used was a Stanford Research Systems SRS 620**						
Coverage Factor (k)	2.04	**The multicalibrator used was a Fluke 5700**						
Expanded Combined Uncertainty	**3.083E-04**							

Estimated uncertainty for voltage measurements based on 0° X-cut crystal for pulsed voltage measurements.

Description	Magnitude	Distribution	Degree of Freedom	Divisor	Standard Uncertainty		Uncertainty Type	Contribution
Crystal Response From DC/AC Voltage	1.88E-05	Normal	4	1	1.88E-05	3.53E-10	A	0.02%
10 MHz External Timebase	3.33E-13	Expanded (k=3)	30	3	1.11E-13	1.23E-26	B	0.00%
Temperature of Crystal	1.50E-04	Normal	30	1	1.50E-04	2.24E-08	B	99.93%
								0.00%
Crystal Dimensions	3.80E-05	Rectangular	30	1.732	2.19E-05	4.81E-10	B	0.05%
Time Interval Counter	8.02E-06	Rectangular	30	1.732	4.63E-06	2.14E-11	B	0.00%
		Notes:						
Combined A & B Standard Uncertainty	1.53E-04	DC and AC Voltage Uncertainty Measurements						
Effective Degrees of Freedom	32	The time interval counter used was a Stanford Research Systems SRS 620						
Coverage Factor (k)	2.04	The multicalibrator used was a Fluke 5700						
Expanded Combined Uncertainty	3.112E-04							

Estimated uncertainty for voltage measurements based on Y+36° cut crystal for Pulsed measurements.

Description	Magnitude	Distribution	Degree of Freedom	Divisor	Standard Uncertainty		Uncertainty Type	Contribution
Crystal Response From DC/AC Voltage	3.70E-05	Normal	4	1	3.70E-05	1.37E-09	A	0.31%
10 MHz External Timebase	3.33E-13	Expanded (k=3)	30	3	1.11E-13	1.23E-26	B	0.00%
Temperature of Crystal	1.57E-04	Normal	30	1	1.57E-04	2.47E-08	B	99.66%
								0.00%
Crystal Dimensions	3.80E-05	Rectangular	30	1.732	2.19E-05	4.81E-10	B	0.04%
Time Interval Counter	8.02E-06	Rectangular	30	1.732	4.63E-06	2.14E-11	B	0.00%
		Notes:						
Combined A & B Standard Uncertainty	1.63E-04	DC and AC Voltage Uncertainty Measurements						
Effective Degrees of Freedom	32	The time interval counter used was a Stanford Research Systems SRS 620						
Coverage Factor (k)	2.04	The multicalibrator used was a Fluke 5700						
Expanded Combined Uncertainty	3.323E-04							

A.4 $LiNbO_3$ CONSTANTS [WARNER *ET AL.*, REF. 113]

Elasticity matrix, *C* [Pa]

$$\begin{bmatrix} 2.03x10^{11} & 0.53x10^{11} & 0.75x10^{11} & 0.9x10^{10} & 0 & 0 \\ 0.53x10^{11} & 2.03x10^{11} & 0.75x10^{11} & -0.9x10^{10} & 0 & 0 \\ 0.75x10^{11} & 0.75x10^{11} & 2.45x10^{11} & 0 & 0 & 0 \\ 0.9x10^{10} & -0.9x10^{10} & 0 & 6.0.x10^{10} & 0 & 0 \\ 0 & 0 & 0 & 0 & 6.0.x10^{10} & 0.9x10^{10} \\ 0 & 0 & 0 & 0 & 0.9x10^{10} & 0.75x10^{11} \end{bmatrix}$$

Piezoelectric matrix, *e* [C/m^2]

$$\begin{bmatrix} 0 & 0 & 0 & 0 & 3.7 & -2.5 \\ -2.5 & 2.5 & 0 & 3.7 & 0 & 0 \\ 0.2 & 0.2 & 1.3 & 0 & 0 & 0 \end{bmatrix}$$

Relative permittivity matrix, ε_r

$$\begin{bmatrix} 38.958 & 0 & 0 \\ 0 & 38.958 & 0 \\ 0 & 0 & 25.677 \end{bmatrix}$$

REFERENCES

[1] D.F. Binns and T.J. Randall, "Improved spark-gap voltmeter," *Proceedings IEEE,* vol. 113, pp. 1557-1561, 1966.

[2] E. Kuffel, W.S. Zaengl, and J. Kuffel, *High Voltage Engineering : Fundamentals*, 2nd ed. Oxford; Boston: Butterworth-Heinemann, 2000.

[3] I. GUM, "Guide to the Expression of Uncertainty in Measurement, (1995), with Supplement 1, Evaluation of measurement data, JCGM 101: 2008," in *Organization for Standardization, Geneva, Switzerland*, ed., 2008.

[4] Ross Engineering Corporation. (2015, September 3, 2015). *HV Voltage Dividers*.Available:http://www.rossengineeringcorp.com/products/measurement/hv-voltage-dividers/hv-voltage-dividers-detailed-info.html

[5] E. Mallett and A.D. Blumlein, "A New ethod of high-frequency resistance measurement," *Journal of the IEE,* vol. 63, pp. 397-412, 1925.

[6] D.L.H. Gibbings, "An alternating-current analogue of the Kelvin double bridge," *Journal of IEE (London),* vol. 109, pp. 307-316, 1962.

[7] J.J. Hill, "Calibration of DC resistance standards and voltage-ratio boxes by an AC method," *Journal of the IEE,* vol. 112, pp. 211-217, 1965.

[8] H.B. Brooks and F.C. Holtz, "The Two-Stage Current Transformer," *Transactions of the American Institute of Electrical Engineers,* vol. XLI, pp. 382-393, 1922.

[9] T.A. Deacon and J.J. Hill, "Two-stage inductive voltage dividers," *Proceedings of the Institution of Electrical Engineers,* vol. 115, pp. 888-892, 1968.

[10] J.J. Hill and T.A. Deacon, "Theory, design and measurement of inductive voltage dividers," *Proceedings of the Institution of Electrical Engineers,* vol. 115, pp. 727-735, 1968.

[11] D.N. Homan and T.L. Zapf, "Two Stage, Guarded Inductive Voltage Divider for Use at 100 kHz," *ISA Transactions,* vol. 9, pp. 201-209, 1970.

[12] K. Grohmann, "A step-up method for calibrating inductive voltage dividers up to 1 MHz," *IEEE Transactions on Instrumentation and Measurements,* vol. IM-25, pp. 516-518, 1976.

[13] National Fire Protection Association, "Standard for Electrical Safety in the Workplace"," in *NFPA 70E-2004* ed. Quincy, MA.

[14] I.F. Budovsky, G.W. Small, A.M. Gibbes, and J.R. Fiander, "Calibration of 1000 V/50 Hz Inductive Voltage Dividers and Ratio Transformers," in *2004 Conference on Precision Electromagnetic Measurements* 2004, pp. 322-323.

[15] V.G. Likhachev, V.M. Baikov, and O.I. Bul'ennaya, "Modular transformer voltage dividers in measuring equipment," *Measurement Techniques,* vol. 32, pp. 92-95, 1989/01/01 1989.

[16] J.H. Park, "Special shielded Resistor for high voltage dc measurements," *Journal of Research of the National Bureau of Standards, Section C: Engineering and Instrumentation,* vol. 66C, pp. 19-24, 1962.

[17] M. Misakian, "High-Voltage Divider and Resistor Calibrations," *National Bureau of Standards (U.S.) Technical Note,* July 1985.

[18] J.H. Park, "Special shielded resistor for high voltage dc measurements," *Journal of Research of the National Bureau of Standards Section C: Engineering and Instrumentation,* vol. 66C, pp. 19-24, January-March 1962.
[19] Y. Li, "Development of precision DC high voltage dividers," in *2010 Conference on Precision Electromagnetic Measurements,* 2010, pp. 569-570.
[20] Y. Li, M.K. Ediriweera, F.S. Emms, and A. Lohrasby, "Development of Precision DC High-Voltage Dividers," *IEEE Transactions on Instrumentation and Measurement* vol. 60, pp. 2211-2216, 2011.
[21] Z.Y. Lee, "Subnanosecond high-voltage two-stage resistive divider," *Review of Scientific Instruments,* vol. 54, pp. 1060-1062, 08/00/ 1983.
[22] A.J. Schwab and J.H.W. Pagel, "Precision Capacitive Voltage Divider for Impulse Voltage Measurements," *IEEE Transactions on Power Apparatus and Systems,* vol. PAS-91, pp. 2376-2382, 1972.
[23] A.I. Gerasimov, A.S. Fedotkin, and V.V. Kulgavchuk, "Small High-Voltage Liquid Resistors," *Instruments and Experimental Techniques,* vol. 37, pp. 176-179, Mar-Apr 1994.
[24] Y. Liu, F. Lin, G. Hu, and M. Zhang, "Design and Performance of a Resistive-Divider System for Measuring Fast HV Impulse," *IEEE Transactions on Instrumentation and Measurement* vol. 60, pp. 996-1002, 2011.
[25] A.I. Gerasimov, "Aqueous-solution high-voltage resistors: Development, study, and application (Review)," *Instruments and Experimental Techniques,* vol. 49, pp. 1-26, Jan-Feb 2006.
[26] T. Hagen and I. Budovsky, "Development of a precision resistive voltage divider for frequencies up to 100 kHz," in *2010 Conference on Precision Electromagnetic Measurements (CPEM)*, 2010, pp. 195-196.
[27] P. Horowitz and W. Hill, *The Art of Electronics*, 2nd ed. Cambridge England ; New York: Cambridge University Press, 1989.
[28] J. Haibin, H. Tingting, H. Zhiyuan, and Y. Li, "Research of a wideband frequency ac resistive divider," in *2011 10th International Conference on Electronic Measurement & Instruments* 2011, pp. 114-116.
[29] R. Prochazka, J. Hlavacek, K. Draxler, and R. Styblikova, "Precise 10 and 20 kV DC/AC resistive divider," in *2013 IEEE International Instrumentation and Measurement Technology Conference*, pp. 774-777.
[30] S.I. Shkuratov, M. Kristiansen, J.C. Dickens, L.L. Hatfield, and E. Horrocks, "High-current and high-voltage pulsed testing of resistors," *IEEE Transactions on Plasma Science* vol. 28, pp. 1607-1614, 2000.
[31] C.S. Wong, "Effect of stray inductance on capacitive-voltage divider," *Journal of Applied Physics,* vol. 59, pp. 673-675, 01/15/ 1986.
[32] D. Lampard, "A new theorem in electrostatics with applications to calculable standards of capacitance," *Proceedings of the IEE-Part C: Monographs,* vol. 104, pp. 271-280, 1957.
[33] P.R. Howard, "Errors in Recording Surge Voltages," *Proceedings of the IEE-London,* vol. 99, pp. 371-383, 1952.

[34] M.M. Brady and K.G. Dedrick, "High-Voltage Pulse Measurement with a Precision Capacitive Voltage Divider," *Review of Scientific Instruments,* vol. 33, pp. 1421-1428, 12/00/ 1962.
[35] L. Jin-Liang, Y. Bing, Z. Tian-Wen, F. Jia-Huai, Z. Jian-de, and W. Xin-Xin, "Coaxial Capacitive Dividers for High-Voltage Pulse Measurements in Intense Electron Beam Accelerator With Water Pulse-Forming Line," *IEEE Transactions on Instrumentation and Measurement,* vol. 58, pp. 161-166, 2009.
[36] N. Benjamin, "High-impedance capacitive divider probe for potential measurements in plasmas," *Review of Scientific Instruments,* vol. 53, pp. 1541-1543, 1982.
[37] J. Mankowski, J. Dickens, and M. Kristiansen, "High voltage subnanosecond breakdown," *IEEE Transactions on Plasma Science,* vol. 26, pp. 874-881, 1998.
[38] S. Jayaram, X.Y. Xu, and J.D. Cross, "High-divider-ratio fast-response capacitive dividers for high-voltage pulse measurements," *IEEE Transactions on Industry Applications* vol. 36, pp. 920-922, 2000.
[39] R. Malewski and N. Hylten-Cavallius, "A Low Voltage Arm for EHV Impulse Dividers," *IEEE Transactions on Power Apparatus and Systems,,* vol. PAS-93, pp. 1797-1804, 1974.
[40] S.I. Shkuratov, E.F. Talantsev, L.L. Hatfield, J.C. Dickens, and M. Kristiansen, "Single-shot, repetitive, and lifetime high-voltage testing of capacitors," *IEEE Transactions on Plasma Science,* vol. 30, pp. 1943-1949, 2002.
[41] E. Hecht, *Optics*, 3rd ed. Reading, Mass.: Addison-Wesley, 1998.
[42] R.E. Hebner, R.A. Malewski, and E.C. Cassidy, "Optical methods of electrical measurement at high voltage levels," *Proceedings IEEE,* vol. 65, pp. 1524-1548, 1977.
[43] L. Bi and H. Li, "An overview of optical voltage sensor," in *Computer Science and Electronics Engineering (ICCSEE), 2012 International Conference on*, 2012, pp. 197-201.
[44] B.H. Billings, S. Sage, and W. Draisin, "A Narrow Passband Polarization Interference Filter for Hydrogen Alpha," *Review of Scientific Instruments,* vol. 22, pp. 1009-1017, 1951.
[45] A.M. Zarem, F.R. Marshall, and F.R. Poole, "An electro-optical shutter for photography," *Electrical Engineering,* vol. 68, pp. 282-288, 1949.
[46] S. Namba, "High Voltage Measurement by ADP Crystal Plate," *Review of Scientific Instruments,* vol. 27, pp. 336-336, 1956.
[47] S.Y. Ettinger and A.C. Venezia, "High Voltage Pulse Measuring System Based on Kerr Effect," *Review of Scientific Instruments,* vol. 34, pp. 221-224, 1963.
[48] D.C. Wunsch and A. Erteza, "Kerr Cell Measuring System for High Voltage Pulses," *Review of Scientific Instruments,* vol. 35, pp. 816-820, 1964.

[49] J.J. Hill and A.P. Miller, "A seven-decade adjustable-ratio inductively-coupled voltage divider with 0.1 part per million accuracy," *Proceedings of the IEE -Part B: Electronic and Communication Engineering,* vol. 109, pp. 157-162, 1962.
[50] K.S. Lee, "Electrooptic voltage sensor: birefringence effects and compensation methods," *Applied Optics,* vol. 29, pp. 4453-4461, 1990/10/20 1990.
[51] J.C. Santos, M.C. Taplamacioglu, and K. Hidaka, "Pockels high-voltage measurement system," *IEEE Transactions on Power Delivery, ,* vol. 15, pp. 8-13, 2000.
[52] P. Bauerschmidt and R. Lerch, "Optical voltage sensor based on a quartz resonator," in *Ultrasonics Symposium, 1996. Proceedings., 1996 IEEE*, 1996, pp. 383-387 vol.1.
[53] A. Kumada and K. Hidaka, "Directly High-Voltage Measuring System Based on Pockels Effect," *IEEE Transactions on Power Delivery, ,* vol. 28, pp. 1306-1313, 2013.
[54] K. Bohnert, P. Gabus, J. Kostovic, and H. Brändle, "Optical Fiber Sensors for the Electric Power Industry," *Optics and Lasers in Engineering,* vol. 43, pp. 511-526, 3// 2005.
[55] B.A. Auld, *Acoustic fields and waves in solids*. New York,: Wiley, 1973.
[56] K. Bohnert, M. Ingold, and J. Kostovic, "Fiber-Optic Voltage Sensor for SF6 Gas-Insulated High-Voltage Switchgear," *Applied Optics,* vol. 38, pp. 1926-1933, 1999/04/01 1999.
[57] K. Bohnert, J. Kostovic, and P. Pequignot, "Fiber optic voltage sensor for 420 kV electric power systems," *Optical Engineering,* vol. 39, pp. 3060-3067, 2000.
[58] L. Bi and H. Li, "An overview of optical voltage sensor," in *International Conference on Computer Science and Electronics Engineering* 2012, pp. 197-201.
[59] National Voluntary. Laboratory Accreditation Program. *Scope of Accreditation to ISO/IEC 17025:2005,Sandia National Laboratory, Primary Standards Laboratory*.
[60] G.J. FitzPatrick and E.F. Kelley, "Comparative high voltage impulse measurement," *Journal of Research of the National Institute of Standards and Technology,* vol. 101, pp. 639-658, Sep-Oct 1996.
[61] T.J. Quinn, "Primary methods of measurement and primary standards," *Metrologia,* vol. 34, p. 61, 1997.
[62] A. Hati, C.W. Nelson, and D.A. Howe, "Vibration sensitivity of optical components: A survey," in *2011 Joint Conference of the IEEE International Frequency Control and the European Frequency and Time Forum* 2011, pp. 1-4.
[63] B. Drafts, "Acoustic wave technology sensors," *IEEE Transactions on Microwave Theory and Techniques,* vol. 49, pp. 795-802, 2001.
[64] J. Curie and P. Curie, "Développement, par pression, de l'électricité polaire dans les cristaux hémièdres à faces inclinées," *Comptes Rendus,* vol. 91, pp. 294-295, 1880.

[65] D.S. Ballantine Jr., R.M. White, S.J. Martin, A.J. Ricco, E.T. Zellers, G.C. Frye, and H. Wohltjen, *Acoustic Wave Sensors: Theory, Design and Physico-Chemical Applications*. New York: Academic Press, 1997.
[66] "IEEE Standard on Piezoelectricity," *ANSI/IEEE Std 176-1987,* 1988.
[67] J.F. Rosenbaum, *Bulk Acoustic Wave Theory and Devices.* vol. 147: Artech House Boston, 1988.
[68] R.S. Weis and T.K. Gaylord, "Lithium niobate: Summary of physical properties and crystal structure," *Applied Physics A,* vol. 37, pp. 191-203, 1985/08/01 1985.
[69] "Standards on Piezoelectric Crystals, 1949," *Proceedings IRE,* vol. 37, pp. 1378-1395, 1949.
[70] A. Fischerauer and G. Fischerauer, "A novel highly sensitive SAW strain sensor with in-built temperature measurement," in *2012 IEEE International Ultrasonics Symposium (IUS)*, 2012, pp. 2094-2097.
[71] Z. Xiangwen, W. Fei-Yue, and L. Li, "Optimal selection of piezoelectric substrates and crystal cuts for SAW-based pressure and temperature sensors," *IEEE Transactions on Ultrasonics, Ferroelectrics and Frequency Control,,* vol. 54, pp. 1207-1216, 2007.
[72] B.H. Fisher and D.C. Malocha, "A study on the aging of ultra-thin Palladium films on SAW hydrogen gas sensors," in *2010 IEEE International Frequency Control Symposium,*, 2010, pp. 242-247.
[73] Z. Xiangwen, W. Fei-Yue, and L. Li, "Optimal selection of piezoelectric substrates and crystal cuts for SAW-based pressure and temperature sensors," *IEEE Transactions on Ultrasonics, Ferroelectrics and Frequency Control,* vol. 54, pp. 1207-1216, 2007.
[74] S.G. Joshi, "Surface acoustic-wave device for measuring high voltages," *Review of Scientific Instruments,* vol. 54, pp. 1012-1016, 08/00/ 1983.
[75] M. Ishido, "Acoustic-wave-based voltage sensors," *Sensors and Actuators A: Physical,* vol. 44, pp. 183-189, 9// 1994.
[76] E. Gatti, A. Palma, and E. Verona, "A surface acoustic wave voltage sensor," *Sensors and Actuators,* vol. 4, pp. 45-54, 1983.
[77] A.V. Medved, R.A. Mishkinis, and P.F. Rutkovsky, "Highly sensitive electrostatic voltage sensor on SAW double-waveguides," *Electronics Letters,* vol. 26, pp. 973-975, 1990.
[78] S. Joshi, "Surface acoustic wave propagation in a biasing electric field," *The Journal of the Acoustical Society of America,* vol. 72, pp. 1872-1878, 1982.
[79] S.G. Joshi, "Voltage-controlled SAW oscillator on temperature-stable quartz substrate," *Proceedings of the IEEE,* vol. 73, pp. 1240-1241, 1985.
[80] J.R. Vig, "Dual-mode oscillators for clocks and sensors," in *Ultrasonics Symposium, 1999. Proceedings. 1999 IEEE*, 1999, pp. 859-868, vol.2.
[81] S.G. Joshi, "A Temperature Compensated High Voltage Probe Using Surface Acoustic Waves," in *1982 Ultrasonics Symposium*, 1982, pp. 317-320.

[82] E. Benes, M. Groschl, F. Seifert, and A. Pohl, "Comparison between BAW and SAW sensor principles," *IEEE Transactions on Ultrasonics, Ferroelectrics, and Frequency Control, ,* vol. 45, pp. 1314-1330, 1998.

[83] J. Werner and A. Dyer, "The Relationship Between Plateback, Mass Loading and Electrode Dimensions for AT-Cut Quartz Crystals Having Rectangular Resonators Operating at Fundamental and Overtone Modes," in *1976 IEEE Symposium on Frequency Control.* , 1976, pp. 40-53.

[84] S.J. Martin, G.C. Frye, and K.O. Wessendorf, "Sensing liquid properties with thickness-shear mode resonators," *Sensors and Actuators A: Physical,* vol. 44, pp. 209-218, 1994.

[85] H.P. Lobl, M. Klee, C. Metzmacher, W. Brand, R. Milsom, P. Lok *et al.*, "Piezoelectric materials for BAW resonators and filters," in *2001 IEEE Ultrasonics Symposium,* , 2001, pp. 807-811, vol.1.

[86] R.C. Ruby, P. Bradley, Y. Oshmyansky, A. Chien, and J.D. Larson, III, "Thin film bulk wave acoustic resonators (FBAR) for wireless applications," in *2001 IEEE Ultrasonics Symposium,*, 2001, pp. 813-821, vol.1.

[87] E.L. Wooten, K.M. Kissa, A. Yi-Yan, E.J. Murphy, D.A. Lafaw, P.F. Hallemeier *et al.*, "A review of lithium niobate modulators for fiber-optic communications systems," *IEEE Journal of Selected Topics in Quantum Electronics,* vol. 6, pp. 69-82, 2000.

[88] A. Kawamata, H. Hosaka, and T. Morita, "Non-hysteresis and perfect linear piezoelectric performance of a multilayered lithium niobate actuator," *Sensors and Actuators A: Physical,* vol. 135, pp. 782-786, 4/15/ 2007.

[89] L. Arizmendi, "Photonic applications of lithium niobate crystals," *Physica Status Solidi (a),* vol. 201, pp. 253-283, 2004.

[90] N. Patel, D.W. Branch, E. Schamiloglu, and S. Cular, "Acoustically determined linear piezoelectric response of lithium niobate up to 1100 V," *Applied Physics Letters,* vol. 104, 2014.

[91] N. Patel, D.W. Branch, E. Schamiloglu, and S. Cular, "Comparative study of 0° X-cut and Y + 36°-cut lithium niobate high-voltage sensing," *Review of Scientific Instruments,* vol. 86, p. 085001, 2015.

[92] G. Kovacs, M. Anhorn, H.E. Engan, G. Visintini, and C.C. W. Ruppel, "Improved material constants for $LiNbO_3$ and $LiTaO_3$," in *Proceedings IEEE*, 1990, pp. 435-438 vol.1.

[93] B.A. Auld, *Acoustic fields and waves in solids*, 2nd ed. Malabar, Fla.: R.E. Krieger, 1990.

[94] H.F. Tiersten, "Electroelastic equations for electroded thin plates subject to large driving voltages," *Journal of Applied Physics,* vol. 74, pp. 3389-3393, 1993.

[95] D. Royer and E. Dieulesaint, *Elastic Waves in Solids II: Generation, Acousto-Optic Interaction, Applications,* vol. 2: Springer, 2000.

[96] Y. Cho and K. Yamanouchi, "Nonlinear, elastic, piezoelectric, electrostrictive, and dielectric constants of lithium niobate," *Journal of Applied Physics,* vol. 61, pp. 875-887, 1987.

[97] K.J. Singh, O. Elmazria, F. Sarry, P. Nicolay, K. Ghoumid, B. Belgacem *et al.*, "Enhanced Sensitivity of SAW-Based Pirani Vacuum Pressure Sensor," *Sensors Journal, IEEE,* vol. 11, pp. 1458-1464, 2011.
[98] X.Q. Bao, W. Burkhard, V. Varadan, and V. Varadan, "SAW temperature sensor and remote reading system," in *1987 IEEE Ultrasonics Symposium,*, 1987, pp. 583-586.
[99] F. Pignatiello, M. De Rosa, P. Ferraro, S. Grilli, P. De Natale, A. Arie *et al.*, "Measurement of the thermal expansion coefficients of ferroelectric crystals by a moiré interferometer," *Optics Communications,* vol. 277, pp. 14-18, 9/1/ 2007.
[100] T.L. Bergman, F.P. Incropera, and A.S. Lavine, *Fundamentals of Heat and Mass Transfer*: John Wiley & Sons, 2011.
[101] M.A. Breazeale, I.V. Ostrovskii, and M.S. McPherson, "Thermal hysteresis of nonlinear ultrasonic attenuation in lithium niobate," *Journal of Applied Physics,* vol. 96, pp. 2990-2994, 2004.
[102] B.D. Zaitsev, I.E. Kuznetsova, S.G. Joshi, and A.S. Kuznetsova, "New method of change in temperature coefficient delay of acoustic waves in thin piezoelectric plates," *Ultrasonics, Ferroelectrics, and Frequency Control, IEEE Transactions on,* vol. 53, pp. 2113-2120, 2006.
[103] R.T. Smith and F.S. Welsh, "Temperature Dependence of the Elastic, Piezoelectric, and Dielectric Constants of Lithium Tantalate and Lithium Niobate," *Journal of Applied Physics,* vol. 42, pp. 2219-2230, 1971.
[104] C.S. Kim, K. Yamanouchi, S. Karasawa, and K. Shibayama, "Temperature dependence of the elastic surface wave velocity on LiNbO3 and LiTaO3," *Japanese Journal of Applied Physics,* vol. 13, p. 24, 1974.
[105] M. Viens and J.D.N. Cheeke, "Highly sensitive temperature sensor using SAW resonator oscillator," *Sensors and Actuators A: Physical,* vol. 24, pp. 209-211, 9// 1990.
[106] H. Oh, W. Wang, K. Lee, I. Park, and S. S. Yang, "Sensitivity improvement of wireless pressure sensor by incorporating a SAW reflective delay line," *Int. J. on Smart Sensing & Intelligent Syst,* vol. 1, pp. 940-954, 2008.
[107] R.A. Graham, "Pressure Depedance of the Piezoelectric Polarization of $LiNbO_3$ and $LiTaO_3$," *Ferroelectrics,* vol. 10, pp. 65-69, 1976.
[108] *AH 2500A 1 kHz Ultra-Precision Capacitance Bridge Operation and Instruction Manual*, Andeen-Hagerling, Cleveland, OH, 1994.
[109] J. Fialka and P. Benes, "Comparison of Methods for the Measurement of Piezoelectric Coefficients," *Instrumentation and Measurement, IEEE Transactions on,* vol. 62, pp. 1047-1057, 2013.
[110] Y. Nakagawa, K. Yamanouchi, and K. Shibayama, "Third-order elastic constants of lithium niobate," *Journal of Applied Physics,* vol. 44, pp. 3969-3974, 1973.
[111] R.N. Thurston, H.J. McSkimin, and P. Andreatch, "Third-Order Elastic Coefficients of Quartz," *Journal of Applied Physics,* vol. 37, pp. 267-275, 1966.

[112] H.J. McSkimin, P. Andreatch, and R.N. Thurston, "Elastic Moduli of Quartz versus Hydrostatic Pressure at 25° and − 195.8°C," *Journal of Applied Physics,* vol. 36, pp. 1624-1632, 1965.
[113] A.W. Warner, M. Onoe, and G.A. Coquin, "Determination of Elastic and Piezoelectric Constants for Crystals in Class (3m)," *Journal of the Acoustical Society of America,* vol. 42, pp. 1223-&, 1967.
[114] I.E. Kuznetsova, B.D. Zaitsev, S.G. Joshi, and I.A. Borodina, "Investigation of acoustic waves in thin plates of lithium niobate and lithium tantalate," *Ultrasonics, Ferroelectrics, and Frequency Control, IEEE Transactions on,* vol. 48, pp. 322-328, 2001.
[115] Q.-M. Wang, T. Zhang, Q. Chen, and X.-H. Du, "Effect of DC bias field on the complex materials coefficients of piezoelectric resonators," *Sensors and Actuators A: Physical,* vol. 109, pp. 149-155, 2003.
[116] A.S. Andrushchak, B.G. Mytsyk, H.P. Laba, O.V. Yurkevych, I.M. Solskii, A.V. Kityk *et al.*, "Complete sets of elastic constants and photoelastic coefficients of pure and MgO-doped lithium niobate crystals at room temperature," *Journal of Applied Physics,* vol. 106, p. 073510, 2009.
[117] S.J. Kline and F. McClintock, "Describing uncertainties in single-sample experiments," *Mechanical Engineering,* vol. 75, pp. 3-8, 1953.
[118] B.J. Klemme and A.R. Mahoney, "Design of an Electro-Optic Device for In-situ Measurement of High Voltage Pulses," *NCSL International Measure,* vol. 3, pp. 48-52, 2008.